



National Library
of Canada

Bibliothèque nationale
du Canada

Acquisitions and
Bibliographic Services Branch

Direction des acquisitions et
des services bibliographiques

395 Wellington Street
Ottawa, Ontario
K1A 0N4

395, rue Wellington
Ottawa (Ontario)
K1A 0N4

Your file *Voire référence*

Our file *Notre référence*

NOTICE

The quality of this microform is heavily dependent upon the quality of the original thesis submitted for microfilming. Every effort has been made to ensure the highest quality of reproduction possible.

If pages are missing, contact the university which granted the degree.

Some pages may have indistinct print especially if the original pages were typed with a poor typewriter ribbon or if the university sent us an inferior photocopy.

Reproduction in full or in part of this microform is governed by the Canadian Copyright Act, R.S.C. 1970, c. C-30, and subsequent amendments.

AVIS

La qualité de cette microforme dépend grandement de la qualité de la thèse soumise au microfilmage. Nous avons tout fait pour assurer une qualité supérieure de reproduction.

S'il manque des pages, veuillez communiquer avec l'université qui a conféré le grade.

La qualité d'impression de certaines pages peut laisser à désirer, surtout si les pages originales ont été dactylographiées à l'aide d'un ruban usé ou si l'université nous a fait parvenir une photocopie de qualité inférieure.

La reproduction, même partielle, de cette microforme est soumise à la Loi canadienne sur le droit d'auteur, SRC 1970, c. C-30, et ses amendements subséquents.

Canada

A GAS TENSION METHOD
FOR AIR-WATER GAS EXCHANGE STUDIES

By
Meredith Anderson

SUBMITTED IN PARTIAL FULFILLMENT OF THE
REQUIREMENTS FOR THE DEGREE OF
DOCTOR OF PHILOSOPHY
AT
DALHOUSIE UNIVERSITY
HALIFAX, NOVA SCOTIA
13 JULY 1993

© Copyright by Meredith Anderson, 1993



National Library
of Canada

Bibliothèque nationale
du Canada

Acquisitions and
Bibliographic Services Branch

Direction des acquisitions et
des services bibliographiques

395 Wellington Street
Ottawa, Ontario
K1A 0N4

395, rue Wellington
Ottawa (Ontario)
K1A 0N4

Your file *Votre référence*

Our file *Notre référence*

The author has granted an irrevocable non-exclusive licence allowing the National Library of Canada to reproduce, loan, distribute or sell copies of his/her thesis by any means and in any form or format, making this thesis available to interested persons.

L'auteur a accordé une licence irrévocable et non exclusive permettant à la Bibliothèque nationale du Canada de reproduire, prêter, distribuer ou vendre des copies de sa thèse de quelque manière et sous quelque forme que ce soit pour mettre des exemplaires de cette thèse à la disposition des personnes intéressées.

The author retains ownership of the copyright in his/her thesis. Neither the thesis nor substantial extracts from it may be printed or otherwise reproduced without his/her permission.

L'auteur conserve la propriété du droit d'auteur qui protège sa thèse. Ni la thèse ni des extraits substantiels de celle-ci ne doivent être imprimés ou autrement reproduits sans son autorisation.

ISBN 0-315-93624-X

Canada

Name MEREDITH ANDERSON

Dissertation Abstracts International is arranged by broad, general subject categories. Please select the one subject which most nearly describes the content of your dissertation. Enter the corresponding four-digit code in the spaces provided.

CHEMICAL OCEANOGRAPHY

0547

U·M·I

SUBJECT TERM

SUBJECT CODE

closest (

Subject Categories

THE HUMANITIES AND SOCIAL SCIENCES

COMMUNICATIONS AND THE ARTS

Architecture 0729
Art History 0377
Cinema 0900
Dance 0378
Fine Arts 0357
Information Science 0723
Journalism 0391
Library Science 0399
Mass Communications 0708
Music 0413
Speech Communication 0459
Theater 0465

EDUCATION

General 0515
Administration 0514
Adult and Continuing 0516
Agricultural 0517
Art 0273
Bilingual and Multicultural 0282
Business 0688
Community College 0275
Curriculum and Instruction 0727
Early Childhood 0518
Elementary 0524
Finance 0277
Guidance and Counseling 0519
Health 0680
Higher 0745
History of 0520
Home Economics 0278
Industrial 0521
Language and Literature 0279
Mathematics 0280
Music 0522
Philosophy of 0998
Physical 0523

Psychology 0525
Reading 0535
Religious 0527
Sciences 0714
Secondary 0533
Social Sciences 0534
Sociology of 0340
Special 0529
Teacher Training 0530
Technology 0710
Tests and Measurements 0288
Vocational 0747

LANGUAGE, LITERATURE AND LINGUISTICS

Language
General 0679
Ancient 0289
Linguistics 0290
Modern 0291
Literature
General 0401
Classical 0294
Comparative 0295
Medieval 0297
Modern 0298
African 0316
American 0591
Asian 0305
Canadian (English) 0352
Canadian (French) 0355
English 0293
Germanic 0311
Latin American 0312
Middle Eastern 0315
Romance 0313
Slavic and East European 0314

PHILOSOPHY, RELIGION AND THEOLOGY

Philosophy 0422
Religion
General 0318
Biblical Studies 0321
Clergy 0319
History of 0320
Philosophy of 0322
Theology 0469

SOCIAL SCIENCES

American Studies 0323
Anthropology
Archaeology 0324
Cultural 0326
Physical 0327
Business Administration
General 0310
Accounting 0272
Banking 0770
Management 0454
Marketing 0338
Canadian Studies 0385
Economics
General 0501
Agricultural 0503
Commerce-Business 0505
Finance 0508
History 0509
Labor 0510
Theory 0511
Folklore 0358
Geography 0366
Gerontology 0351
History
General 0578

Ancient 0579
Medieval 0581
Modern 0582
Black 0328
African 0331
Asia, Australia and Oceania 0332
Canadian 0334
European 0335
Latin American 0336
Middle Eastern 0333
United States 0337
History of Science 0585
Law 0398
Political Science
General 0615
International Law and Relations 0616
Public Administration 0617
Recreation 0814
Social Work 0452
Sociology
General 0626
Criminology and Penology 0627
Demography 0938
Ethnic and Racial Studies 0631
Individual and Family Studies 0628
Industrial and Labor Relations 0629
Public and Social Welfare 0630
Social Structure and Development 0700
Theory and Methods 0344
Transportation 0709
Urban and Regional Planning 0999
Women's Studies 0453

THE SCIENCES AND ENGINEERING

BIOLOGICAL SCIENCES

Agriculture
General 0473
Agronomy 0285
Animal Culture and Nutrition 0475
Animal Pathology 0476
Food Science and Technology 0359
Forestry and Wildlife 0478
Plant Culture 0479
Plant Pathology 0480
Plant Physiology 0817
Range Management 0777
Wood Technology 0746
Biology
General 0306
Anatomy 0287
Biostatistics 0308
Botany 0309
Cell 0379
Ecology 0329
Entomology 0353
Genetics 0369
Limnology 0793
Microbiology 0410
Molecular 0307
Neuroscience 0317
Oceanography 0416
Physiology 0433
Radiation 0821
Veterinary Science 0778
Zoology 0472
Biophysics
General 0786
Medical 0760
EARTH SCIENCES
Biogeochemistry 0425
Geochemistry 0996

Geodesy 0370
Geology 0372
Geophysics 0373
Hydrology 0388
Mineralogy 0411
Paleobotany 0345
Paleoecology 0426
Paleontology 0418
Paleozoology 0985
Palynology 0427
Physical Geography 0368
Physical Oceanography 0415

HEALTH AND ENVIRONMENTAL SCIENCES

Environmental Sciences 0768
Health Sciences
General 0566
Audiology 0300
Chemotherapy 0992
Dentistry 0567
Education 0350
Hospital Management 0769
Human Development 0758
Immunology 0982
Medicine and Surgery 0564
Mental Health 0347
Nursing 0569
Nutrition 0570
Obstetrics and Gynecology 0380
Occupational Health and Therapy 0354
Ophthalmology 0381
Pathology 0571
Pharmacology 0419
Pharmacy 0572
Physical Therapy 0382
Public Health 0573
Radiology 0574
Recreation 0575

Speech Pathology 0460
Toxicology 0383
Home Economics 0386

PHYSICAL SCIENCES

Pure Sciences
Chemistry
General 0485
Agricultural 0749
Analytical 0486
Biochemistry 0487
Inorganic 0488
Nuclear 0738
Organic 0490
Pharmaceutical 0491
Physical 0494
Polymer 0495
Radiation 0754
Mathematics 0405
Physics
General 0605
Acoustics 0986
Astronomy and Astrophysics 0606
Atmospheric Science 0608
Atomic 0748
Electronics and Electricity 0607
Elementary Particles and High Energy 0798
Fluid and Plasma 0759
Molecular 0609
Nuclear 0610
Optics 0752
Radiation 0756
Solid State 0611
Statistics 0463
Applied Sciences
Applied Mechanics 0346
Computer Science 0984

Engineering
General 0537
Aerospace 0538
Agricultural 0539
Automotive 0540
Biomedical 0541
Chemical 0542
Civil 0543
Electronics and Electrical 0544
Heat and Thermodynamics 0348
Hydraulic 0545
Industrial 0546
Marine 0547
Materials Science 0794
Mechanical 0548
Metallurgy 0743
Mining 0551
Nuclear 0552
Packaging 0549
Petroleum 0755
Sanitary and Municipal 0554
System Science 0790
Geotechnology 0408
Operations Research 0796
Plastics Technology 0795
Textile Technology 0994

PSYCHOLOGY

General 0621
Behavioral 0384
Clinical 0622
Developmental 0620
Experimental 0623
Industrial 0624
Personality 0625
Physiological 0982
Psychobiology 0349
Psychometrics 0632
Social 0451



For John

'Love one another, but make not a bond of love:

Let it rather be a moving sea between the shores of your souls.'

KAHILIL GIBRAN

Contents

List of Tables	ix
List of Figures	x
Abstract	xii
Symbols	xiii
Acknowledgements	xv
1 Introduction	1
1.1 General Introduction	1
1.2 Gas Flux Models	2
1.2.1 Gas Flux via Bubbles	3
1.3 Gas-Exchange Measurements	7
1.3.1 Review of Laboratory Studies	7
1.3.2 Field Studies	10
1.4 Parametrization of Gas Exchange	12
1.5 Summary	13
2 Experimental Plan	16
2.1 Introduction	16
2.2 Bubble Generation and Measurement	16
2.3 A New Measurement	17
2.4 Gas-exchange Experiments	17

2.5	Model and Analysis	19
3	Bubble Populations	21
3.1	Bubble Generation	21
3.2	Photographic/Illuminated-slab Technique	22
3.2.1	Side-view photographs	23
3.2.2	Overhead photographs	27
3.2.3	Data accumulation	27
3.3	Bubble Concentration Results	28
3.3.1	Freshwater plume	28
3.3.2	Seawater plume	35
3.3.3	Bubble concentration calculations	35
3.4	Discussion	36
3.4.1	Rise time	36
3.4.2	Depth of focus measurements	39
3.4.3	$C_b(d)$: bubble concentrations as a function of diameter	41
3.4.4	$C_b(z)$: bubble concentrations as a function of depth	44
3.5	Summary	46
4	A Gas Tension Method for Studying Flux Across a Gas-Water Interface	49
4.1	Introduction	49
4.2	The Gas Tension Device	50
4.2.1	Physical description	50
4.2.2	Calibration	52
4.2.3	Theoretical response	52
4.2.4	Response time	54
4.3	Experimental Program	58
4.3.1	Apparatus	58
4.3.2	Variables	61
4.4	Gas-Exchange Results	64
4.4.1	Example: CO ₂ invasion into sea water with bubble injection.	64
4.4.2	Further results	65

4.5	V_0 Measurement	76
4.6	The Hydrostatic Effect	79
4.7	Summary	82
5	Depth-dependent Gas Flux Model	83
5.1	Introduction	83
5.2	Model Development	85
5.2.1	Equilibrium flux	85
5.2.2	Individual bubble flux	85
5.2.3	Depth-dependent bubble (DDB) flux	87
5.2.4	Total bubble flux	89
5.2.5	Total gas flux	90
5.3	Discussion	90
5.3.1	Analysis of the total gas flux equation	90
5.3.2	Bubble population effects	91
5.3.3	Bubble size and dynamics	93
5.3.4	Anti-bubble Bias	94
5.4	A Tool for Gas-Exchange Analysis	95
5.5	Steady-state Supersaturations	96
5.6	Predictions from the DDB Flux Model	98
5.6.1	Predictions relevant to the bubble-injection experiments	98
5.6.2	Gas tension profiles	100
5.7	Summary	101
6	Invasion Experiments with Bubble Injection	103
6.1	Introduction	103
6.2	Experiments	104
6.2.1	Purging	104
6.2.2	Gas-Exchange Experiment Details	104
6.3	Review of Analysis Technique	108
6.4	Results Example	111
6.5	Results	114

6.5.1	Combined gas-exchange velocity, k'	122
6.5.2	Surface gas-exchange velocity, k	122
6.5.3	Bubble exchange velocity, $\langle k_b \rangle$	125
6.5.4	Steady-state saturation anomaly, s^0 and Δ^0	125
6.6	Discussion	125
6.6.1	Gross features: k' , Δ^0	125
6.6.2	k and $\langle k_b \rangle$	129
6.7	Summary	130
7	Discussion and Conclusions	133
7.1	Introduction	133
7.2	Temperature and Related Effects	133
7.2.1	Solubility	133
7.2.2	Diffusivity	134
7.2.3	Pressure	135
7.2.4	Humidity	135
7.3	Suggestions for Further Work	135
7.3.1	Hardware improvements	136
7.3.2	Field instrument	137
7.4	Conclusions	139
	Appendix A Pressure Sensor Calibration	142
	Appendix B Calculations	146
	Appendix C Data Analysis Routines	151
	Bibliography	161

List of Tables

3.1	Measured bubble population characteristics	35
3.2	Small bubble sampling	40
3.3	Bubble concentrations as a function of diameter — literature values	42
3.4	Measured values of the exponent n in the seawater plume	43
4.1	Freshwater experiments record	62
4.2	Seawater experiments record	63
4.3	V_0 measurements	78
4.4	Recovery time constants	78
5.1	Bubble population features — qualitative effect on gas transfer.	91
6.1	Invasion experiments with bubble injection—experimental conditions.	106
6.2	Temperature range between experiments	107
6.3	Duplicate experiment model analysis	114
6.4	Gas-exchange velocities — summary of experimental results.	124

List of Figures

1.1	Gas flux model schematics	9
2.1	Gas properties	18
3.1	Photographic sampling scheme	24
3.2	Sample photograph	26
3.3	Freshwater plume at 1 s	29
3.4	Freshwater plume at 2 s	30
3.5	Seawater plume at 1 s	31
3.6	Seawater plume at 2 s	32
3.7	Bubble concentrations versus diameter	33
3.8	Bubble concentrations versus diameter (cont.)	34
3.9	Bubble rise times	38
3.10	Measured bubble concentrations versus diameter	45
3.11	Measured bubble concentrations versus depth	47
4.1	Exploded view of the gas tension device (GTD)	51
4.2	Schematic of the GTD pressure-sensing mechanism.	53
4.3	GTD theoretical response	55
4.4	Apparatus	59
4.5	CO ₂ invasion experiment: raw data	66
4.6	CO ₂ invasion into sea water with bubble injection	69
4.7	CO ₂ evasion from sea water with bubble injection	70
4.8	He invasion into sea water with bubble injection	71
4.9	He invasion into fresh water with bubble injection	72

4.10	N ₂ Invasion into fresh water with bubble injection	73
4.11	N ₂ Invasion into fresh water, 'null' mixing conditions	74
4.12	N ₂ Invasion into sea water under 'circulation' mixing conditions	75
4.13	Voltage response after a V_0 measurement	77
4.14	Draining exercise	81
5.1	Gas flux model notation	86
5.2	Normalized supersaturation as a function of the ratios z_b/d_m and $\langle k_b \rangle/k'$	99
6.1	Oxygen displacement	105
6.2	Example of start time selection	110
6.3	CO ₂ invasion into sea water with bubble injection — analysis	112
6.4	CO ₂ invasion into sea water with bubble injection — duplicate analysis	113
6.5	N ₂ invasion into fresh water with bubble injection	115
6.6	He invasion into fresh water with bubble injection	116
6.7	Ar invasion into fresh water with bubble injection	117
6.8	CO ₂ invasion into fresh water with bubble injection	118
6.9	Ar invasion into sea water with bubble injection	119
6.10	N ₂ invasion into sea water with bubble injection	120
6.11	He invasion into sea water with bubble injection	121
6.12	Gas-exchange velocities — summary of experimental results	123
7.1	Driving forces for invasion and evasion	138
A.1	Calibration apparatus	144
A.2	Calibration curve	145

Abstract

The most interesting scientific problems tend to occur at interfaces, both physical and disciplinary. Study of gas exchange processes across the air-sea interface requires the tools of atmospheric scientists, chemical engineers, and chemical and physical oceanographers. Gas exchange is least well understood under the dynamic conditions of wave breaking and bubble injection, when fluxes are expected to be large. Results from studies under such conditions have led to controversial results, e.g. high local fluxes that are difficult to reconcile with global budgets. The largely unresolved differences await improved instrumentation, new approaches, and more data. A new method based on measurement of total dissolved gas pressure ('gas tension' for succinctness) is described. In experiments the state of gaseous equilibrium of a water parcel in a closed tank is continuously monitored using a simple 'gas tension device' (GTD) developed for this purpose. Measurement of the dissolved gas content of the water, and response to changes in applied gas-phase pressure, allows calculation of gas exchange velocities and steady-state supersaturations. Exchange rates of argon, nitrogen, helium and carbon dioxide are determined in this work in single-gas experiments. Effort is concentrated on the generally neglected experimental configuration of gas invasion with bubble injection. An intermittent waterfall provides bubble injection in a type of simulated breaking-wave. Photographic examination of the bubble populations shows many small bubbles in sea water compared with fewer and larger bubbles in fresh water. The results show that the bubble population in sea water contributes to higher gas exchange velocities than the bubble population generated by the same mechanism in fresh water. A model developed as a tool for interpreting the new gas tension measurements incorporates a simple depth-dependent bubble gas flux model and allows a total gas exchange velocity to be further separated into components for the free-surface exchange velocity and the bubble exchange velocity. The gas tension method provides a sensitive, robust, and versatile technique for gas-exchange studies. With simple modifications the GTD will be a useful field instrument.

Symbols

- β Bunsen coefficient of solubility: volume of gas (STP) absorbed per unit volume of liquid when the partial pressure of the gas is one atmosphere.
- δ Hydrodynamic boundary layer thickness
- δ_0 Diffusive boundary layer thickness
- Δ Saturation anomaly as a percentage, $\Delta = s/\bar{p} \times 100\%$
- σ Surface tension of water, 0.07 Pa m^{-1}
- μ Dynamic viscosity, ($1.13 \times 10^{-3} \text{ kg m}^{-1} \text{ s}^{-1}$ for sea water (S=34psu) and $1.00 \times 10^{-3} \text{ kg m}^{-1} \text{ s}^{-1}$ for fresh water, at 20°C)
- ν Kinematic viscosity, ($1.100 \times 10^{-6} \text{ m}^2\text{s}^{-1}$ for sea water (S=34 psu) and $1.004 \times 10^{-6} \text{ m}^2\text{s}^{-1}$ for fresh water, at 20°C) $\mu = \nu/\rho$
- ρ Density
- τ Time constant
- a Abbreviation for k'/d_m in P_{calc}
- b Abbreviation for $\rho g \langle k_b \rangle c_2/c_1$ in P_{calc}
- c Concentration of dissolved gas
- c^* Air solubility: amount of gas absorbed from moist (water-vapour saturated) air at a total pressure of one atmosphere

d_m Depth of mixing layer. 'Mixing' layer to signify an actively mixing body of water and to avoid any preconceptions associated with 'mixed' layer. Calculated as water volume to depth ratio.

D Molecular diffusivity of dissolved gas in water

g Acceleration due to gravity

H Henry's Law constant, $H = p/c^*$

k Exchange velocity (piston/transfer coefficient)

p Gas-phase gas pressure

P Gas tension (pressure of dissolved gas)

P^* Equilibrium gas tension, ($P^* = p$)

r Calibration ratio for GTD in $V \text{ mbar}^{-1}$

s Saturation anomaly, $s = P - P^*$, also $s = P - p$. Usual reference is to steady-state saturation anomaly, s^0 .

Sc Schmidt number, $Sc = \nu/D$

V Voltage

u_{10} Wind speed at ten metres elevation

w' Variation in vertical velocity about a mean value (at a fixed height above the sea surface).

z Depth below the mean free water surface.

z_b e -folding depth of bubble exchange velocity, assumed to be equal to the e -folding depth of the bubble distribution

Superscripts and subscripts

* Equilibrium

⁰ Steady-state

_b Of or relating to bubbles

Acknowledgements

I am grateful for the Dalhousie Graduate Fellowship and Killam Memorial Scholarship that supported me financially during my time at Dalhousie. For additional support, both financial and emotional, I am deeply grateful to John Haines, my husband and hero.

I am grateful to my supervisor, Bruce Johnson, and members of my supervisory committee, Dan Kelley, Bob Moore and Stu Smith for the assistance they offered. I thank my supervisor and committee for their encouragement, enthusiasm and cooperation. For the concept of the gas tension device, which became the focus of the thesis work, I applaud Bruce's ingenuity. For my computer literacy and access I am grateful to friends and faculty in physical oceanography at Dalhousie and also at the U.S. Geological Survey Coastal Center. I also thank the Aquatron crew, especially Tinker, for helping out on many projects in the workshops.

Life at Dal was made incredibly pleasant by wonderful friends and flatmates, especially Dan and Janet. Thanks also to Janet's mom for those Sunday family dinners and other kindnesses. For energizing squash games I thank all my mates, including Val and John, and earlier Jean, Myriam and Julie. For sympathetic understanding I am also grateful for the friendships of Kumiko, Sherry, and Val.

To John, who suffered for so long all the disadvantages of married life without the advantages, thanks for making it work.

Chapter 1

Introduction

1.1 General Introduction

The incentive for studying the gas transfer process in the ocean is to understand and quantify the ocean's role as a source or sink for many important gases. Of particular current interest, because of their possible role in climate change, are the trace gases: carbon dioxide, methane, chlorofluorocarbons, sulfur dioxide, and oxides of nitrogen (*Wang et al.*, 1986). Understanding the behaviour of inert gases, whose behaviour is influenced solely by physical processes, is the first goal. Measurement and modelling of the effect of physical processes on gas concentrations will aid in the separation of those effects from the contributions of biological and chemical processes. The ability to model the physical contributions to oxygen supersaturations, for example, should help to resolve a controversy amongst biological oceanographers over estimates of productivity in the ocean (*Platt*, 1984; *Platt and Harrison*, 1985; *Platt and Harrison*, 1986; *Emerson et al.*, 1991).

The ability to model the air-sea exchange process for CO₂ is the ultimate goal of many researchers involved in gas-exchange studies (e.g., Joint Global Ocean Flux Study). The exchange of CO₂ across air-water boundaries is a crucial link in models of the global carbon cycle. Currently geochemists trying to solve global carbon budgets use air-sea gas-exchange rates that are twice as large (*Tans et al.*, 1990) as those in general use in the gas-exchange community (*Liss and Merlivat*, 1986), yet they are still perhaps underestimating the uptake of carbon by the ocean. Undersampling of extreme conditions is certainly a problem but also temperature effects on gas transfer rates may have not been fully appreciated (*Watson*,

1992; Phillips, 1991; Robertson and Watson, 1992).

1.2 Gas Flux Models

A useful starting point in consideration of gas exchange across the air-water interface has been a concept taken from the chemical engineering literature (*Whitman, 1923*), summarized by Danckwerts (1970). Bubbles are ignored. Thin boundary layers are assumed to exist on each side of the interface between a region of vertically well-mixed water and its overlying atmosphere (Figure 1.1). The statistical mean thickness of the boundary layer is set by a balance between thickening by molecular diffusion and erosional thinning by mixing in the interior. Transfer across the layers occurs by molecular diffusion. For slightly soluble gases, CO₂ included, diffusion across the water-side boundary layer is the rate-determining step in the gas transfer. Solving the partial differential equations describing steady-state diffusion across a boundary layer of thickness δ , for the case where no chemical reaction is occurring, leads to a formulation for the gas flux, F_e , in terms of the concentration step, Δc , across the water-side boundary layer, and a mass transfer coefficient, k ,

$$F_e = -k\Delta c. \quad (1.1)$$

The rate of transfer per unit area per unit driving force, k , has units of velocity and is referred to in the literature as a ‘transfer’, ‘exchange’, or ‘piston’ velocity, with an even wider range of symbols being used. Here k (with relevant subscripts) will be adopted. The concentration difference may also be converted to a partial pressure difference by dividing by Henry’s law constant. The Henry’s law constant describes the gas-phase pressure that would be in gaseous equilibrium with the gas concentration in water and has units of pressure per unit concentration. In the simplest interpretation, k is evaluated as the diffusivity of the gas in water divided by the thickness of the boundary layer (*Higbie, 1935; Liss, 1973*). A laminar film, free from movements which would redistribute the gas, is an unrealistic model under most oceanic conditions and, not surprisingly, its thickness is not easily determined. However, the concept of a thin boundary layer whose thickness is controlled by wind-induced turbulence has spawned a multitude of similar models. For example, in surface renewal models the film is periodically refreshed (*Danckwerts, 1951*) and there are models based on analogy to turbulent boundary-layer theory (*Deacon, 1977; Kerman, 1984*). Refinements of

the simplest model include expressing k as a function of diffusivity (D) and the kinematic viscosity (ν) via the Schmidt number, $Sc = \nu/D$. Considering their simplicity, these models have met a reasonable amount of success in explaining observations under a limited range of conditions. There is general agreement that $k \propto Sc^{-\frac{2}{3}}$ under ‘smooth interface’ conditions (in agreement with boundary-layer theory) and that $k \propto Sc^{-\frac{1}{2}}$ under ‘rough interface’ conditions (in agreement with surface-renewal theory) (Ledwell, 1984; Holmén and Liss, 1984; Coantic, 1986; Jähne *et al.*, 1987b). The ‘smooth’ to ‘rough’ transition occurs when wavelets appear, at a wind speed of about 5 m s^{-1} , depending on the geometry of the experimental tank and on the extent of contamination of the water with surface-active materials. The thin film model and those similar to it shall be included under the umbrella name of equilibrium flux models, because their driving force term always drives the system towards an equilibrium condition where gas pressures are equal in each phase.

1.2.1 Gas Flux via Bubbles

At wind speeds above about 13 m s^{-1} in wind-wave tanks (perhaps lower in the ocean) wave breaking becomes significant. Kanwisher (1963) was the first to recognize that breaking waves can inject bubbles to depths where hydrostatic pressures may force them to dissolve, even in water already saturated with gas. Bubbles injected by breaking waves therefore provide an additional mechanism for gas transfer. Bubbles are used as mediators of gas transfer in so many chemical engineering processes that they have even been described as one of the chemical engineer’s ‘elementary particles’ (Clift *et al.*, 1978). Bubble dynamics and mass transfer properties have been reasonably well-studied in this context, although with emphasis on single gas systems. Studies of mass transfer from bubbles relevant to ocean conditions, including consideration of the effect of waves on bubble dynamics, was introduced to the oceanographic literature by Thorpe (1982) and Merlivat and Méneray (1983).

There are two fundamental differences between the gas transfer mechanism via bubbles and that at the sea surface. First there are additional terms in the driving force for gas transfer via bubbles, over and above the difference between the dissolved gas pressure and gas pressure in the atmosphere. The hydrostatic pressure of the overlying water increases

the internal pressure of bubbles and this increases the driving force for gas transfer. Bubbles injected to 10 m, for example, are pressurized an additional one atmosphere due to hydrostatic pressure. Surface tension force increases as bubble size decreases and provides another term, the Laplace pressure ($2\sigma/r$), in the driving force for gas transfer. Bubbles with a diameter smaller than 100 μm experience Laplace pressures larger than 0.01 atm; a 10 μm bubble experiences a Laplace pressure of order 0.15 atm. The internal pressure is alleviated both as the buoyant bubble rises (and thus expands), and as the component gases equilibrate with the surrounding water. The exchange of gas may be into, or out of, the bubble, depending on the concentration of gases in the surrounding water. A standard technique in gas analysis, for example, is to strip the gas from a water sample by bubbling an inert 'carrier' gas through the solution.

Hydrostatic and Laplace pressures are always positive terms and consequently bubble dissolution is favoured over bubble growth. This asymmetry means that gas supersaturation is supported by bubble injection processes. Gas supersaturations are a common condition in the ocean and there is general agreement that they are at least partially supported by bubble injection processes (*Craig and Weiss, 1971; Atkinson, 1973; Broecker and Peng, 1982; Craig and Hayward, 1987*). Possible causes of supersaturation besides bubble injection include temperature increase or atmospheric pressure decrease since equilibration, and biological activity.

The second fundamental difference between the mechanisms of gas transfer via bubbles and via the sea surface is that the gas phase has additional constraints on it in the case of bubbles. Bubble growth or shrinkage causes internal pressure and composition changes that affect further gas transfer. The compositional changes arise because of solubility effects. At equilibrium the mole fractions of dissolved gases are different from their mole fractions in air, because of the widely differing solubilities of the component gases. A bubble initially has the same composition as the atmosphere and will become enriched in the less soluble gas as gas exchange reflects the preferred partitioning between phases of each gas. These composition changes have been verified by experiments, e.g. (*Wyman et al., 1952*), and are observable because the volume of a bubble, being much smaller than the atmosphere, is strongly influenced by gas exchange with the surrounding water. The atmosphere contains 95% of the inventory of all gases on earth (*Broecker and Peng, 1982*) and has a largely

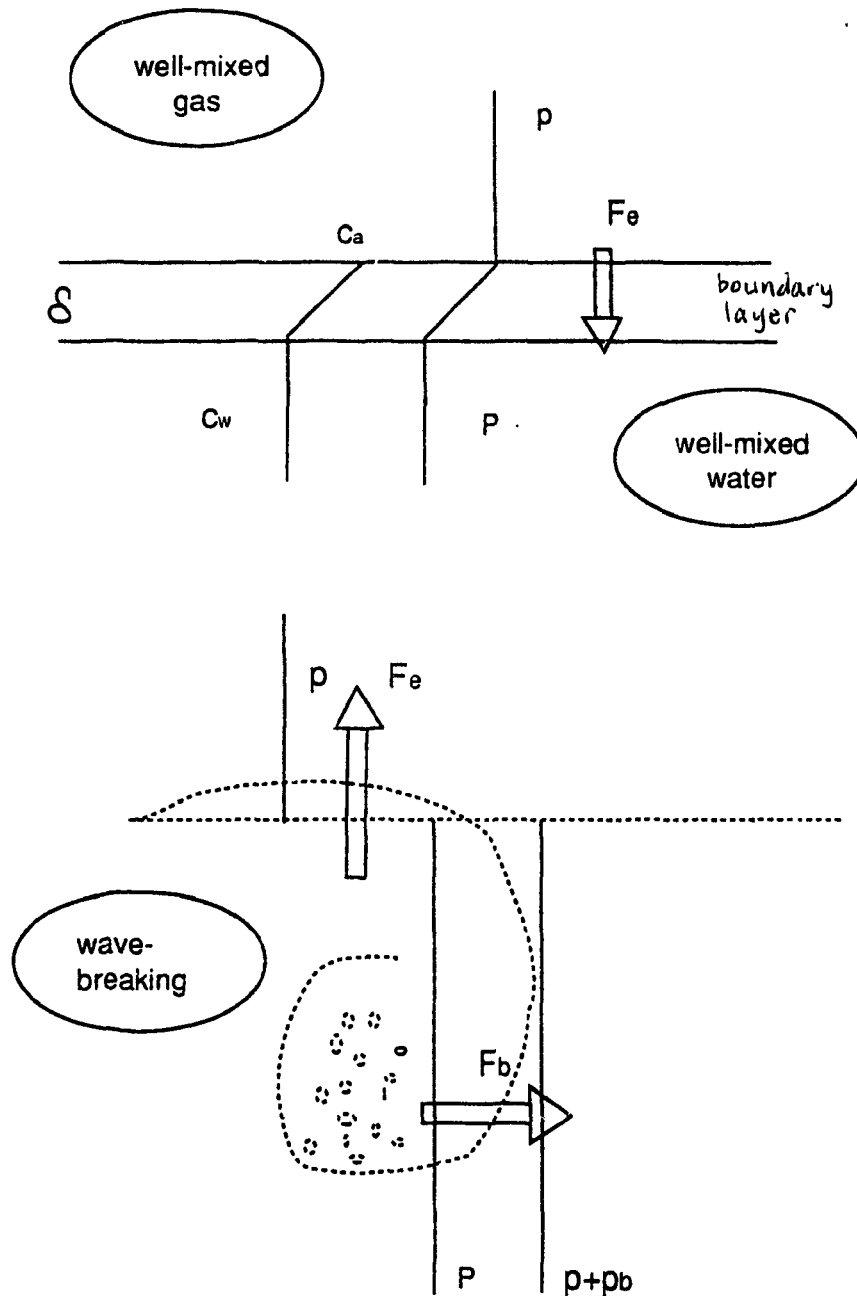


Figure 1.1: The equilibrium flux, F_e , across a water boundary layer (thickness δ) between well-mixed gas and water phases (upper figure) is proportional to $P - p$, or alternatively to $c_w - c_a$. Henry's law constant allows the concentration c_a in equilibrium with p to be calculated. Equilibrium is when $p = P$. A bubble flux, F_b , is proportional to $P - p_b$, where p_b is p plus hydrostatic and Laplace pressures (lower figure). Steady state is when $F_e + F_b = 0$, i.e. $k(P - p) = k_b(P - p_b)$.

invariant composition, except for water vapour and annual hemispheric cycles in CO₂. When the total internal pressure of a bubble is sufficiently high, some of the 'excess' of the less soluble gas that would otherwise have risen out is forced to dissolve, thus effecting a relative supersaturation of the less soluble gas. Slowly dissolving gases are compressed by a shrinking volume caused by the relatively more rapid dissolution of other gaseous components. The magnitude of the internal pressure changes arising from gas exchange and hydrostatic and Laplace pressure contributions will be relatively less significant for large bubbles and become relatively more significant for small bubbles. The rise time of a bubble puts a limit on the degree to which its contents equilibrate. The size of a bubble plays a role in determining the degree of equilibration, by affecting the rise time through buoyancy and surface effects. The interplay between a bubble's dynamics and its mass transfer properties is complex in even the most basic of scenarios. Modelling the total bubble gas flux dauntingly requires an accounting of the contributions of all the bubbles in a population. The task is complicated because bubble populations change in both space and time, making them difficult to measure. The simplifications chosen to make the bubble flux a tractable modelling problem are likely to critically affect model predictions. Supporting experimental bubble flux data under a variety of well-defined conditions are necessary and, as yet, rare.

Merlivat and Mémery's model for gas flux including the role of bubbles (*Merlivat and Mémery*, 1983; *Mémery and Merlivat*, 1984) is unrealistically formulated in such a way that the exchange velocity tends to infinity as a gas concentration in equilibrium with the atmosphere is approached. This situation arises because, although an additional exchange velocity for bubbles is included, additional driving force terms are not. Thorpe (1982; 1984) developed his bubble flux model by combining his own acoustic field observations of bubble distributions as a function of wind speed with empirical mass flux formulae. Wallace and Wirick (1992) found that Thorpe's model for bubble gas flux, when used in combination with a standard model for sea-surface gas exchange, successfully reproduced their field observations of O₂ concentration changes under storm conditions. The bubble flux model of Spitzer and Jenkins (1989) includes a factor for the fractional degree of bubble dissolution estimated to be occurring, but was found by Wallace and Wirick (1992) to be less satisfactory in reproducing the storm-driven O₂ observations than the model of Thorpe. Further theories

on bubble-mediated gas exchange (*Woolf and Thorpe, 1991; Thorpe et al., 1992*), largely reflecting the results of laboratory studies (discussed in the next section), continue to refine the models. However, the relative importance of the different contributing factors, under the range of conditions that present themselves in the ocean, is still poorly understood.

1.3 Gas-Exchange Measurements

Studies under storm conditions are difficult to conduct. Consequently investigation of the gas transfer process has largely been carried out under relatively calm conditions at sea and in wind-wave tanks in the laboratory, where the physical parameters may be controlled or easily monitored.

1.3.1 Review of Laboratory Studies

With the assumption that wind stress at the sea surface is responsible for the turbulence that enhances gas-exchange rates, wind-wave tank experiments have been carried out to determine an empirical relationship between gas-exchange coefficients and wind speed.

In typical tank experiments the water in the wind-wave tank is injected with a tracer gas and the subsequent decrease in the concentration of the tracer in the water, or increase of tracer in the gas phase, is monitored periodically through chemical analyses. Frequently the effects of surface films, fetch, wave height, and bubbles have also been of interest and measured in some way (*Broecker et al., 1978; Merlivat and Mémery, 1983; Broecker and Siems, 1984; Jähne et al., 1985; Jähne et al., 1987b; Goldman et al., 1988*).

Most wind-wave tank studies show a small gradual increase in k with wind speed at moderate wind speeds, followed by a rapid increase in k concomitant with the appearance of waves and a further dramatic increase in k at the onset of wave breaking. Useful summaries are given by Liss and Merlivat (1986) and Wanninkhof (1992). Surprisingly, no consistent enhancement of gas transfer rate has been observed in experiments with mechanically-produced waves instead of wind-induced waves. It is often suggested that increased gas-exchange rates are largely due to increases in surface area available for gas exchange, both when waves are present and when bubbles are injected (*Downing and Truesdale, 1955; Merlivat and Mémery, 1983*). However, Csanady (1990) offers a mathematical

solution with respect to small wavelets in which he suggests that the free surface area is not the relevant parameter, but rather it is flow divergences in the surface layer. Surface divergences, with vertical motions distinct from orbital wave motions, are suggested to be responsible for 'handing-over' the gas-exchange process from the diffusive scale to the eddy scale. The density of divergences should increase with wind speed up to the point at which other processes become important – processes that include large wave breaking, whitecapping and bubble production. Csanady suggests that the many discrepancies between field and laboratory data (discussed in section 1.3.2), as well as the large amount of scatter in field data, arise due to saturation of wave fields in the laboratory on the one hand and the diverse wave 'climate' in the ocean on the other. An important consequence of Csanady's work is confirmation of the theoretical gas-exchange rate dependence on Schmidt number under moderate mixing conditions.

Also, it is not clear to what degree surface-active contaminants are responsible for discrepancies between data sets. Engineering studies, as reviewed by Clift et al. (1978), have shown that the reduction in mass transfer caused by surfactants can be 'striking', and depend critically on the particular combination of liquid and surfactant.

Wave breaking in the laboratory occurs at wind speeds around 13 m s^{-1} , depending on the particular geometry of the tank, and is at the upper operating limit of most wind-wave tanks. Consequently few laboratory studies have been carried out at high wind speeds. The dramatic increase in k at about this point has been universally attributed to wave breaking and bubble injection. Recently the existence of an additional mechanism has been suggested by Khoo and Sonin (1992) who intriguingly found a similar transition to a higher mass transfer mode for surfaces not subject to mean shear, with no wave breaking or bubble injection. In their experiments agitation was applied from below the water surface in a manner that generated no waves at the surface. Khoo and Sonin (1992) suggest that the observed augmentation of gas transfer is related to changes in the turbulent transport mechanism in the near-surface water.

There have been very few studies in which both gas-exchange rates and bubble populations have been measured. The thesis work of Siems (1980) is the earliest and his results are summarized in Broecker and Siems (1984), where it is shown that the break point to higher exchange velocities occurs at lower wind speed for O_2 than for CO_2 . Merlivat and

Mémery (1983) similarly suggested that the break point occurred at lower wind speed for the less soluble Ar, than for the more soluble N₂O in their experiments. Jähne et al. (1984b, 1985) used a laser light scattering bubble detecting system in concert with Rn evasion and He invasion and evasion rate measurements, but were forced to conclude that their bubble populations were insufficient to give a bubble flux signal. Broecker and Siems (1984) and Jähne et al. (1985) concluded that the gas-exchange rate for the less soluble gas was sensitive to the size distribution of the bubbles, in particular the number of small bubbles present. The additional surface area that bubbles provide is not a satisfactory basis for estimating their contribution to gas exchange, because the efficiency of the surface varies with the size of the bubble. Also, when the fact that bubble populations are known to be distinctly different in sea water compared with fresh water (*Monahan and Ziellow, 1969; Zieminski and Whittemore, 1971; Scott, 1975; Thorpe, 1982; Thorpe et al., 1992*) is considered in light of recent evidence of the sensitivity of bubble gas transfer to bubble size, a caution is apparent. That caution is flux measurements should not be indiscriminately compared between fresh water, e.g., (*Wanninkhof et al., 1985*), and sea water when bubble injection is occurring.

Gas-exchange experiments have been conducted in whitecap simulation tanks with the objective of developing a remotely observable indicator of gas exchange under wave breaking conditions in the ocean (*Torgersen et al., 1989; Monahan and Torgersen, 1991; Asher et al., 1991*). A whitecap, generated by periodically tipping a volume of water into a 1.2 m deep tank of water, is characterized by the degree of foam coverage as interpreted by computer-aided video analysis. Experiments comparing He, O₂, SF₆, and DMS (*Asher et al., 1991*) evasion suggest that the exchange velocity dependence on the Schmidt number has an exponent of -0.3 during bubble injection, i.e. the magnitude of the exponent is reduced from the -0.5 established by theory and experiment for high wind conditions before wave breaking. Evasion experiments comparing the rate of Rn loss from sea water and fresh water (*Torgersen et al., 1989*) found the rate to be faster from sea water, both when the whitecap simulation was active and when the water in the tank was simply stirred.

Surfactants have been investigated in several studies relevant to air-sea gas exchange (*Jähne et al., 1984a; Broecker et al., 1978; Goldman et al., 1988*); earlier studies are reviewed by Liss (1983). The effect of surfactants is to create a barrier to mass transfer, directly and

through inhibition of surface turbulence (e.g. wave damping). Bubbles injected in natural waters rapidly accumulate surface-active contaminants. Surfactants affect a bubble's stability with respect to dissolution (*Johnson and Cooke, 1981*) and slow its terminal rise velocity through increased surface drag. Further surfactant studies relevant to gas exchange in natural systems are needed.

1.3.2 Field Studies

Different time and space scales are inherent in each of the approaches to gas-exchange study that have been used in the field. The techniques range from ^{14}C budgets that are averaged globally over years to localized micrometeorological measurements that are on minute time scales. A few of the techniques are summarized here, and Liss (1983) provides a comprehensive background.

The radon deficiency method (*Broecker, 1965; Broecker and Peng, 1971*) for estimating gas-exchange rates has been most widely used (Geosecs cruises in both the Atlantic and Pacific oceans - (*Peng et al., 1979*); TTO - (*Smethie et al., 1985*); JASIN, FGGE - (*Kromer and Roether, 1983*)). The radon deficit is calculated as the amount of ^{222}Rn required to balance the radio-isotopic equilibrium concentration with its naturally present parent, ^{226}Ra . The gas in deficit has been lost to the atmosphere and so the evasion rate, as a moving average on the time scale of the half-life of ^{226}Ra (3.8 days), can be calculated. Roether and Kromer (1984) discuss the method, suggesting that the method underestimates fluxes for changeable conditions and high wind speeds. Deacon (1981) screened the offending conditions out of Geosecs data and found the slope of the remaining k_{Rn} versus wind speed data to be an order of magnitude smaller than that found in wind-wave tank studies.

Gas-exchange rates for ^{222}Rn are used to estimate k_{CO_2} and transfer velocities for other gases by application of relative diffusivity relationships via the Schmidt number. However, even finding consistent data sets of gas diffusivities is difficult (*Holmén and Liss, 1984; Wanninkhof, 1992*). The resulting CO_2 fluxes (using CO_2 concentration estimates) are supported (arguably) by being within the bounds of the globally averaged fluxes derived from ^{14}C budgets of naturally occurring and bomb-produced ^{14}C (*Broecker et al., 1985*). These results have then been used by Broecker et al. (1986) to question reports of higher fluxes obtained by the eddy-flux method of Smith and Jones (1985) and Wesley et al. (1982).

However, just as wind speeds may episodically be very high and average to lower values, it follows that eddy-fluxes may episodically and locally be high, and average to lower values on the longer time and larger space scales inherent in some other method (*Smith and Jones, 1986; Smith et al., 1991*).

The eddy-correlation flux method requires measurement of microscale variability in both vertical wind velocity and air mass properties. The method has been applied particularly successfully by agricultural meteorologists to determine heat, water vapour and CO₂ fluxes above crops (*Desjardins et al., 1989*). The CO₂ fluxes above crops are an order of magnitude larger than those expected in the marine environment. The sensitivity of the instrumentation has recently been improved by an order of magnitude and earlier nearshore oceanic CO₂ fluxes (*Smith and Jones, 1985*) made with the unimproved sensor are supported by recent eddy-flux measurements (*Smith et al., 1991*). Fluxes are shown to respond to changes in the CO₂ concentration difference between the air and the water. Both downward and upward fluxes are measured. Controversially, the eddy-flux measurements do not show a close correlation with wind speed. However, the wave climate in the ocean often does not show a close correlation with wind speed, and some of the scatter in field results is undoubtedly due to this fact.

Episodic high flux events associated with breaking waves have recently been observed in open coastal waters by Wallace and Wirick (1992) who moored polarographic O₂ probes over winter in the Mid Atlantic Bight. Just as storm events are important contributors to seasonal mixed-layer deepening and sea-surface temperature cooling (*Large et al., 1986*), such events are thought to provide a significant contribution to annual gas budgets for O₂ and CO₂ (*Thomas et al., 1990*). The data of Wallace and Wirick also demonstrate the asymmetry in gas exchange that bubble-mediated processes introduce, asymmetry that manifests itself both as a tendency towards water supersaturation and also as higher rates of ingassing of the water column relative to degassing. These effects were first suggested by Atkinson (1973). My own interpretation is that the effect of falling atmospheric pressure on gas concentrations as a storm builds is more than offset by the effects of increasing bubble dissolution and falling temperatures. The result is a relatively rapid increase in gas concentrations to supersaturated levels while the bubble ingassing flux dominates any surface degassing flux. Surface degassing erodes the supersaturation at the surface and this

process comes to dominate over bubble injection fluxes as the storm subsides, even as the driving force for degassing is diminished by rising atmospheric pressure. The net effect is an overall slower degassing of the water column than ingassing, because bubble fluxes pump up gas concentrations during a storm event and recovery is largely via slower equilibrium fluxes. To summarize, an asymmetry exists in the bubble flux between the *driving force* for invasion and the *driving force* for evasion, thus supporting supersaturation. The degree of supersaturation reached is moderated by surface fluxes. An asymmetry between *exchange velocities* for invasion and evasion is not necessary to explain net ingassing enhancement of the water column over degassing during storm events.

1.4 Parametrization of Gas Exchange

Gas-exchange rate to wind speed relationships have been the subject of most efforts, both in the laboratory and in the field. The increase in k with wind speed has been interpreted to be linear within restricted wind-speed ranges by some workers (*Broecker et al.*, 1978; *Broecker and Siems*, 1984; *Smethie et al.*, 1985; *Liss and Merlivat*, 1986). Others interpret k to be proportional to some power of wind speed near 2 (*Kanwisher*, 1963; *Deacon*, 1981; *Hartman and Hammond*, 1985; *Smith*, 1985; *Broecker et al.*, 1985; *Wanninkhof*, 1992). Currently favoured is a piece-wise linear relation where k increases with increasing wind speed (*Liss and Merlivat*, 1986) over three different regimes. The reference conditions are at a Schmidt number appropriate for CO_2 at 20°C . This linearization allows the application of mean wind-speed data to estimate gas fluxes whereas any higher power relationship to wind speed inconveniently requires a knowledge of the variability of wind speed. *Wanninkhof et al.* (1985) point out that even using mean wind speed and the linear relations may give different gas-exchange rate results depending on whether the wind is steady or varies over the range where one linear relation ends and the next begins.

In an effort to more closely describe the near surface turbulence that is considered to control gas transfer, other parameters have also been investigated and these include friction velocity in the water (*Deacon*, 1977), sea-surface backscatter (*Etcheto and Merlivat*, 1988; *Wanninkhof and Bliven*, 1991), and sea-surface foam (*Monahan and Spillane*, 1984; *Asher et al.*, 1991). Hopefully, satellite-based observations of radar backscatter will eventually aid estimates of global gas fluxes.

Parametrization of the gas-exchange process under the most dynamic conditions, with large breaking waves and bubble injection, is least well defined, being least well understood. Although the duration of dynamic conditions in the ocean may be relatively brief, the gas fluxes are potentially large and their location may be critical. For example, gas exchange in areas of deep water formation deserves further study. Calculations of global gas fluxes for any gas based on measurements of another gas by simple application of a Schmidt number relationship (*Liss and Slater, 1974; Thomas et al., 1988; Murphy et al., 1991; Erickson III, 1993*) must be met with criticism beyond any disagreement with the selection and application of a particular wind-speed relationship. The main objection is that gas fluxes under dynamic conditions, being undersampled, large, and with poorly defined parameter sensitivities, are underrepresented.

Robertson and Watson (1992) suggest that the topmost 1 mm ‘skin’ of the ocean, having a lower temperature than the water beneath over much of the world’s ocean, has a capacity for absorbing gas that is greater than has previously been considered. The thermodynamic arguments of Phillips (1991) also suggest that air-water temperature differences are more important than has previously been considered. Phillips points out that the usual formulation of the driving force for gas transfer in terms of a partial pressure difference is a limiting case for small pressure differences. More generally it is the chemical potential difference between the phases that should be considered. The chemical potential incorporates a term for the heat of solution of the particular gas and so couples the gas transfer to heat transfer. Phillips suggests that the driving force for CO₂ gas flux may be significantly underestimated by ignoring the temperature gradient across the air-water interface.

1.5 Summary

The general applicability of wind-wave tunnel results to the open ocean is arguable: even the largest tanks with the most sophisticated configurations (e.g. Institut de la Mécanique Statistique de la Turbulence has a gas tight, recirculating, 40-metre-long wind-wave tank and 100 cm water depth) cannot reproduce high sea-state conditions and also may suffer wall and surface contamination effects (*Liss, 1983; Jähne et al., 1987b*) and other limitations. However many interesting effects, especially regarding the role of bubbles, require further

investigation and may best be examined in controlled laboratory experiments. For example, bubbles have an asymmetric effect on invasion and evasion processes (*Atkinson, 1973; Woolf and Thorpe, 1991; Wallace and Wirick, 1992*) and may introduce a net exchange rate dependence on solubility (*Merlivat and Mémerly, 1983; Broecker and Siems, 1984; Jähne et al., 1985*). Consequently it is necessary to further examine factors which affect bubble populations, e.g. salinity and wave breaking (*Monahan and Zietlow, 1969; Zieminski and Whittemore, 1971; Scott, 1975; Shatka and Ronen, 1992; Baldy, 1988; Thorpe, 1982*), and those factors which affect the behaviour of gases in bubbles, e.g. solubility, diffusivity, and saturation levels (*Broecker and Siems, 1984; Woolf and Thorpe, 1991; Thorpe et al., 1992*). The recent demonstrations of the sensitivity of bubble-mediated gas transfer to different parameters should raise the concern that evasion-only experiment configurations and indiscriminate comparisons of freshwater results to seawater results may not have accurately represented the role of bubbles in the past. It is well documented that bubble populations produced by breaking waves have distinctly different signatures in seawater compared with freshwater (*Monahan and Zietlow, 1969; Thorpe, 1982*). The results of further laboratory studies will help direct future oceanic flux studies, especially those so urgently required under storm conditions.

A closer look at a recent field study conducted under near storm conditions shows some of the difficulties and limitations in current methods for estimating gas-exchange rates in the field. Watson and coworkers (1991) injected two inert tracer gases at a depth of 10 m and mapped their subsequent dispersal over 10 days. This was the first artificial tracer injection experiment to measure water to air gas transfer in the ocean, following the earlier lake experiments of Torgersen et al. (1982), Wanninkhof et al. (1985) and Upstill-Goddard et al. (1990). There were operational difficulties and the complexity of sampling and on-board chemical analyses of dissolved gases suggests that there will always be difficulties under storm conditions. Injecting and mapping dispersal of gas tracers is not trivial and was simplified by delivering two tracers into the water. The changing relative concentrations of the two tracers is interpreted by assuming a particular dependence of gas-exchange velocity on Schmidt number — an assumption that has been validated by theory and experiment only under moderate wind-wave conditions. Field studies have not yet incorporated the laboratory finding that exchange velocity appears to be a function of solubility when bubble

transport becomes significant. The exchange rates determined by Watson et al. (1991) are reported as probably being underestimates, but will not be improved until better accounting of the role of bubbles is included. The authors point out that scenarios of increased frequency of storms as a consequence of climate change further emphasise the need for more data under storm conditions.

It is apparent from the literature that important questions remain about the gas-exchange process in natural systems. Direct in situ measurements of the time-varying concentration of naturally present gases are needed to properly describe the process. Interpretation of such measurements and modelling advances for dynamic conditions require further understanding of the role of bubbles in the gas-exchange process. Such understanding will be facilitated by laboratory studies.

Chapter 2

Experimental Plan

2.1 Introduction

Chapter 1 described the difficulties and pitfalls that have been prevalent in gas-exchange studies under the dynamic conditions of wave breaking and bubble injection. In this chapter I present the experimental plan chosen to overcome or avoid these difficulties. Most notably, a new measurement technique, and its use in gas-exchange experiments with an alternative means of bubble generation is pursued.

2.2 Bubble Generation and Measurement

Recognizing the difficulties with working at the upper operating limit of wind-wave tanks, an alternative bubble injection system was desirable. To make a significant contribution to the total gas flux, many bubbles have to be injected, and be injected deeply. A closed-tank system, in which water recirculates via a peristaltic pump to a bucket that periodically tips out the accumulated water in a waterfall, was chosen. Cipriano and Blanchard (1981) argue that the breakup of air entrained by falling water produces a spectrum of bubble sizes that is common to all entrainment mechanisms. They support this argument, both by making the analogy to the breakup of water into an invariant raindrop spectrum, and by comparing their own waterfall-generated bubble populations to field observations. The main disadvantage of this arrangement is that there is no measure of mixing comparable to wind speed. However, since bubble injection is the process of major concern, measurements of the

bubble population provide the most relevant information. The system and the photographic technique for measuring the generated bubbles used in this work are described in Chapter 3. Bubble populations generated by the intermittent waterfall under the same conditions, in both sea water and fresh water, were measured and are compared in Chapter 3.

2.3 A New Measurement

A decision was made to pursue a new measurement of total dissolved gas pressure, the water-phase analog of barometric pressure. In principle, measurement of the difference between total dissolved gas pressure (gas tension) and gas-phase pressure provides a direct measure of the degree of supersaturation of a solution. Such a measurement would be ideally suited to following gas-exchange studies where injected bubbles drive a system to supersaturation.

A gas tension device (GTD) was developed to make continuous in situ measurements. Gas tension, being a physical, rather than a chemical measurement of gas content, has both advantages and limitations: pressure measurement sensitivity is high, but in a mixture of gases only the total pressure is measured; there is no gas specificity. The GTD and its response in single-gas exchange experiments are described in Chapter 4.

2.4 Gas-exchange Experiments

A range of gas-exchange experiments was selected to demonstrate the gas tension method and to explore the sensitivity of bubble-mediated gas exchange to the conditions of particular interest. Based on their ready availability and the wide range of chemical properties they represent, the gases He, N₂, Ar, and CO₂ were selected for use in single-gas experiments. The range of solubilities and diffusivities of these gases in both sea water and fresh water is illustrated in Figure 2.1.

In recognition of the possible role of temperature effects, the temperature of the system was carefully kept at room temperature and measured.

Gas fluxes were initiated by applying step changes to the gas-phase pressure. The high sensitivity meant that only small perturbations were necessary to initiate a measurable flux. This was both desirable and risky. The advantage was that the tank did not have to structurally withstand large over-pressures, since perturbations on the scale of normal

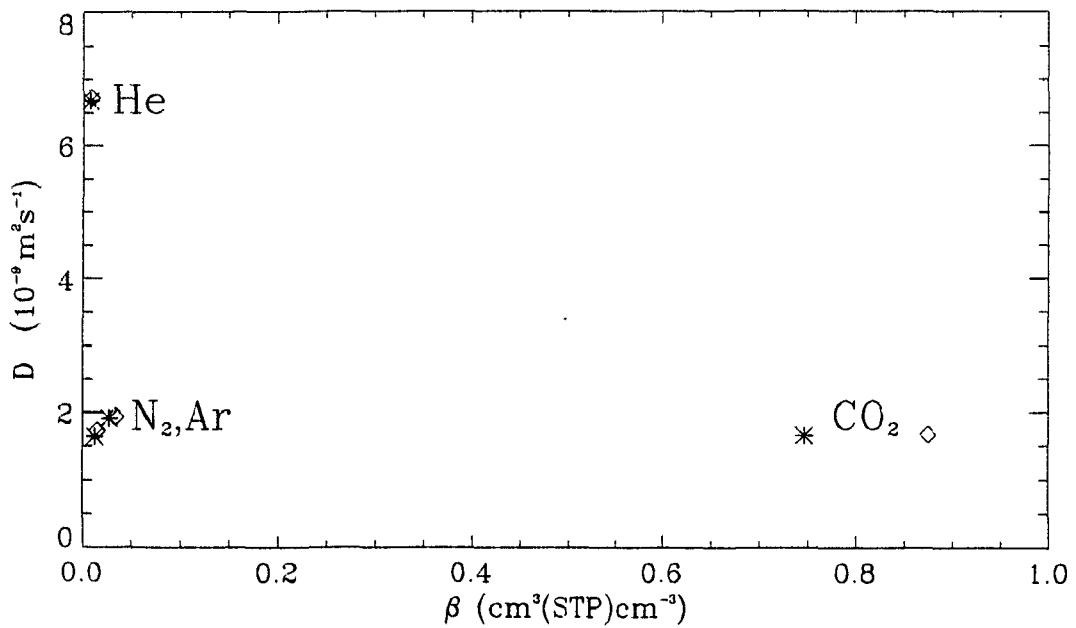
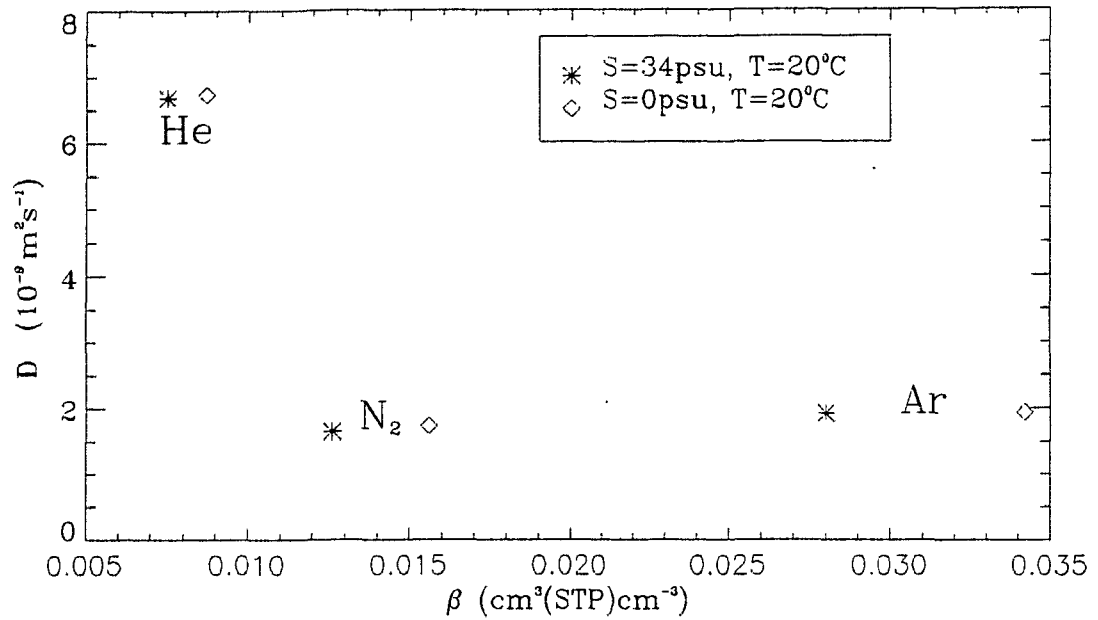


Figure 2.1: Gas properties. Gas diffusivity, D in $\text{m}^2 \text{ s}^{-1}$, versus gas solubility in terms of the bunsen coefficient, β in $\text{cm}^3(\text{STP})\text{cm}^{-3}$. The data are for fresh water at 20°C and sea water at 20°C and 34 psu. The values were determined from empirical formulae using the coefficients tabulated by Wanninkhof (1992) which derive largely from the experimental solubility data of Weiss (1970; 1971; 1974) and from the experimental diffusivity data of Jähne et al. (1987a).

atmospheric variations were sufficient to initiate a measurable flux. The risk was that perturbations other than the one of interest might influence the gas flux.

With the gas tension method, both invasion and evasion experiments were possible, in sea water and fresh water, with and without bubble injection. Questions of primary interest were chosen to direct the course of the gas exchange experimentation:

1. Does the gas tension device provide a useful measurement in gas exchange studies?
2. Are gas-exchange rates different in sea water and fresh water?
 - (a) Are any of the differences in gas-exchange rates between sea water and fresh water due to different bubble populations in the two media?
 - (b) What are the relative importance of gas properties and bubble populations in determining gas-exchange rates?
3. Are gas invasion rates equal to gas evasion rates when bubble injection is occurring? Since bubbles are known to be effective at stripping gas out of a volume of water, the question of whether their effectiveness is equal in both a stripping case and an injecting case arises.

2.5 Model and Analysis

A model was needed as a tool for interpreting the gas-exchange data. The basic concept is followed that supersaturations principally arise because of the hydrostatic pressures that bubbles experience at depth. The model is therefore strongly depth-dependent and used the measured degree of supersaturation to separate the total gas flux into contributions from the bubble flux and the surface equilibrium flux. The model thus allowed calculation of the components of the combined gas-exchange velocity, that is, the equilibrium exchange velocity, k , and the bubble exchange velocity, k_b . The model is developed in Chapter 5.

In Chapter 6 the results of the gas-exchange experiments are interpreted using the model. The trends in k between different gases as a function of Sc are examined. The trends in k_b are investigated to see if they give any insight into the mechanism of gas exchange via bubbles.

Errors for the gas tension method that have not been covered in earlier chapters, and effects that require further consideration, are discussed in Chapter 7. Suggestions for improvements, more experiments, and development of a field instrument are made. The answers to the questions posed in Section 2.4 provide the substance of the brief conclusion.

Chapter 3

Bubble Populations

“When a wave breaks, the largest bubbles surface first, and thus the bubble spectrum is a function of time as well as position in the whitecap. To obtain the total number of bubbles produced, a sequence of spectra in both space and time must be secured, an extremely difficult if not impossible task.”

(*Cipriano and Blanchard, 1981*)

3.1 Bubble Generation

The bubbles in these experiments were injected in a breaking-wave simulation, like Torgersen *et al.*'s (*Torgersen et al., 1989*), after the design of Cipriano and Blanchard (1981) who argue that the breakup of a volume of air entrained in falling water should produce bubble spectra that approach a characteristic shape, a shape produced by common plunging and spilling waves (*Cokelet, 1977*) in the sea (*Cipriano and Blanchard, 1982*). Cipriano and Blanchard (1981) avoided some of the sampling difficulty they describe above by operating their weir in a continuously overflowing mode in order to produce a steady-state bubble population. However, for the present experiments the waterfall is operated intermittently, so as not to bias the population in favour of large fast-rising bubbles. Water is pumped from the bottom of the tank to a bucket balanced above the water surface. As it fills, the bucket's center of gravity moves until the bucket becomes unstable and pivots, dumping its accumulated load in a bubbly plume. The bucket then pivots back to its resting position. In order to maximize the potential contribution of bubbles to gas transfer, a tall narrow geometry was

adopted. Bubbles were injected deep into a volume of water that had a low free surface area. A water volume of approximately 0.8 l was dumped from a height of 0.7 m once every 90 s or so, the result of recycling the tank water through a peristaltic pump at a rate of 0.55 l min^{-1} . Calculation and observation suggest this flow rate does not produce cavitation in the pumping line. The weir volume is the upper limit able to manoeuvre within the geometry of the tank and still produce a relatively unconstrained plume — a plume in which the bubbles are not broken up by interaction with the walls of the tank. Torgersen, Monahan and colleagues (*Torgersen et al.*, 1989; *Monahan and Torgersen*, 1991; *Asher et al.*, 1991) have used a similar arrangement as a whitecap simulation for gas-exchange studies, however they have not reported the bubble populations generated.

The bubble population in the intermittent plume was intended to closely approach the source bubble population under a breaking wave. Most often, observed bubble populations represent the background populations that persist after bubble dissolution, dilution and rise-out. Source population measurements are essential for evaluating the potential of the bubbles to effect gas transfer. The objective of this exercise was to quantify the bubble populations provided by the intermittent waterfall. In particular, differences between the population generated in sea water and that generated in fresh water were of primary interest.

The water in each case was at room temperature, about 22°C .

3.2 Photographic/Illuminated-slab Technique

A problem that arises in photographic measurements of bubble concentration is how to determine or define the sample volume and then measure just those bubbles that occur within the specified volume. In these experiments a vertical slab of water was illuminated from either side by focussed flash strobes. The two side strobes, when triggered synchronously with a third strobe providing diffuse background illumination, very clearly stopped bubble motion and defined those bubbles which were within the illuminated slab.

Each side strobe was focussed through a razor blade slit and a convex perspex lens and then directed through a translucent strip of coloured film attached to the outside of the tank. Because the walls of the tank were round, and the light had to pass through the acrylic walls into the water, it took careful alignment of the angle of incidence of the side strobes on the outer walls to illuminate a slab of water through the desired section

of the plume. A different colour strip was used on each side and served to not only help with alignment and width definition of the strobe beams, but also to subsequently provide orientation when looking at the photographs. The illuminated slab was satisfactorily narrow when there were no bubbles present, of order a couple of centimetres. When bubbles were present they scattered the light and increased the thickness of the slab. The thickness of the slab was therefore determined in each instance by analysis of overhead photographs.

The camera was focussed on a wire suspended through the middle of the illuminated section. The wire had knots at calibrated distances along its length and was photographed at the start of each time series of photographs. The camera used was a 35-mm Pentax ME Super camera with a 50-mm macro lens and f-stop setting at 16. The flash speed was approximately 1×10^{-4} s. The film used was Kodak Ektachrome-100 colour slide film and development was done by a commercial laboratory.

3.2.1 Side-view photographs

Photographs of bubbles were taken through the side of the tank at three depths, two and sometimes three vertical sections, and usually 8 times over the plume's duration. Figure 3.1 shows the positions and labelling of the sections and layers. Tripping of the camera shutter was done manually. Elapsed times, measured by stopwatch, start at the moment the weir started tipping water and stop at the time the shutter was pressed. Duplicate photographs were taken starting when the plume was sufficiently dispersed to make distinct bubble measurements, around 0.9 s, and at approximately 0.3 s intervals thereafter. After 2.5 s photographs were taken less frequently.

The camera was positioned in front of the tank, about 0.5 m from the section of interest. This arrangement allowed relatively large areas of the plume to be sampled in each photograph. However, it limited the size of the smallest bubbles that were measurable to $100 \mu\text{m}$. This resolution is not ideal considering that the concentration of bubbles is known to increase with decreasing radius down to some cut-off radius of about $40 \mu\text{m}$ to $20 \mu\text{m}$ (*Medwin and Breitz, 1989*). However, the primary goal was to quantify some general differences between the bubble populations in sea water compared with fresh water, using the same production and analysis techniques in each medium. This has been reported only in general terms previously (*Monahan and Zietlow, 1969*). Detailed statistically reliable bubble

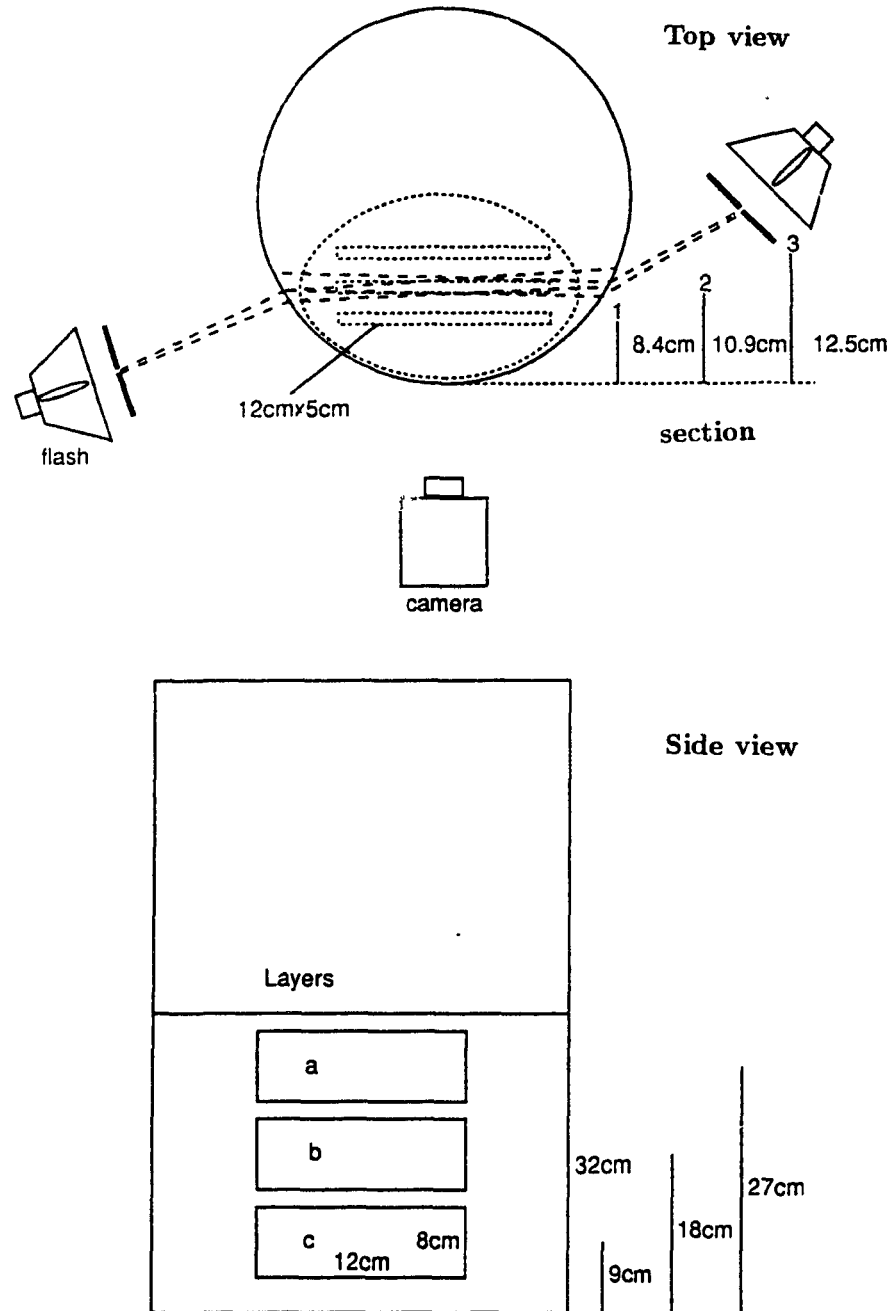


Figure 3.1: Sampling scheme for photographic/illuminated-slab method: top view and side view.

spectra require more complicated and intensive measurement techniques than that available for this investigation. However, even state-of-the-art laser techniques (*Baldy, 1988*) have sample size and time resolution constraints. Ideally, differences in the bubble populations would be investigated over the size range considered to be most important in gas transfer, i.e. those smaller than about $200\ \mu\text{m}$ (*Woolf and Thorpe, 1991*), however adequate sampling of the small bubbles and definition of their sampling volume are not satisfied by this labour intensive photographic method.

Figures 3.2, 3.3, 3.4, 3.5, and 3.6 are examples of photographic samples. The slides were interpreted in the following way.

1. Slides were projected onto paper with an image approximately $80\ \text{cm} \times 50\ \text{cm}$.
2. Slides of the calibrated wire were taken in each section before turning on the intermittent waterfall and used for size calibration. Typical magnifications were 6.6.
3. Bubbles which were in some sense distinct were outlined in pencil for later measurement. 'Distinct' implies a 'satisfactory level' of focus of the bubble and the bright coloured spots produced by the side strobes. A second person made an independent selection of bubbles on several slides for comparison.
4. Bubbles with just one bright spot, but otherwise clearly in focus, were included in the count to allow for side-shading by other bubbles.
5. Areas of high density of illuminated bubbles, in which individual bubbles were not distinct, were outlined and the measured area/volume not included as sample volume. In these cases the bubble density will be underestimated.
6. Where high numbers of bubbles in the foreground obscured the illuminated section, a correspondingly reduced sample volume was calculated.

Many of the first slides in a time series, taken around 0.9 s, had bubble densities that were too dense to calculate. Also, the bubble density is probably underestimated in those slides where there are areas of illuminated-but-indistinct bubbles.

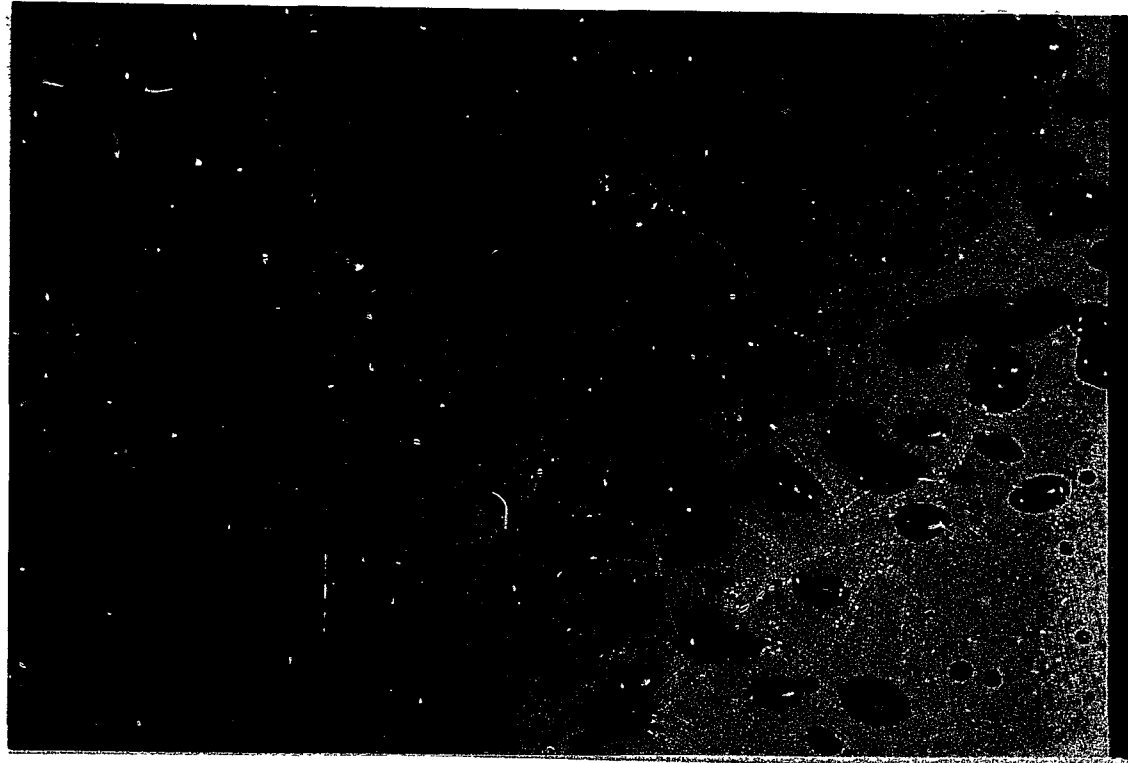


Figure 3.2: A typical photographic sample of the bubbles injected by the intermittent waterfall. The distance between the top knot and the middle knot of the wire (dia. 0.020 inches) is 2.954 ± 0.020 cm, and between the middle and bottom knot is 2.951 ± 0.020 cm. This example is middepth in a freshwater plume 2 seconds after the bucket pivot (i.d:10.23, s3, lb, t2.2 — refer to Figure 3.1 for explanation).

3.2.2 Overhead photographs

Overhead photographs of the evolution of the bubble plume were made corresponding to positions and times sampled in the side-view photographs. The slides were interpreted in the following way.

1. Overhead slides of the illuminated water slab were projected onto paper in the same manner as for the previous slides. A disk on the bottom of the tank was used for size calibration.
2. The outline of the illuminated section was sketched.
3. An average width of the slab at the midsection was obtained from 5 evenly-spaced measurements taken across the area sampled by the side-view photos. The uncertainty in this measurement ranges from 30% to 100% or more due to the irregular thickness and somewhat subjectively defined boundaries of the illuminated volume.

3.2.3 Data accumulation

The data accumulation and reduction steps are outlined below. Few bubbles are spherical; most are oblate spheroids with their long (equatorial) axis oriented perpendicular to the direction of travel.

1. The equatorial diameters, d_e , of the outlined bubbles were measured to the nearest 0.5 mm on the image (corresponding to about $100\mu\text{m}$ in the bubble). The aspect ratio of the bubbles was determined from the ratio of the axial diameter, d_a to the equatorial diameter.
2. A volume-equivalent diameter, d_{ve} , was calculated for those bubbles with an aspect ratio of less than 0.6 from

$$d_{ve} = \left(\frac{3}{2}d_e^2d_a\right)^{\frac{1}{3}}.$$

This volume-equivalent diameter is estimated from the volume of a disk with a surface area $\pi d_e^2/4$ and thickness equal to d_a .

3. Tally sheets of the number of bubbles in each 0.5 mm size range on the image were totalled for each slide.

4. Computations applied the scaling factor and rebinned the tallies based on bin increments of 0.01 cm diameter. The number of bubbles was divided by the calculated sample volume to give results in terms of bubble concentrations versus bubble diameter.

Each photograph samples a volume of 0.48 l on average, with dimensions 12 cm × 8 cm × 5 cm (width × depth × thickness) compared with a total water volume of about 48 l.

3.3 Bubble Concentration Results

A subset of the bubble measurements, those at a vertical cross-section through the middle of the plume, are described in fresh water (section 3.3.1) and sea water (section 3.3.2) over time series at 3 depths. The *shallow* sample is over the depth range 1 cm to 9 cm, the *mid-depth* sample is over the range 10 cm to 18 cm and the *deep* sample is over the range 19 cm to 27 cm. Photographs (Figures 3.3–3.6) and graphs (Figures 3.7 and 3.8) illustrate the differences between the time-series of the mid-depth fresh water results and those in sea water.

3.3.1 Freshwater plume

Most bubbles in the freshwater plume have diameters smaller than 0.8 cm with typical concentrations in the most populated size bins of about 10 bubbles per litre. Details of results at the three depths are as follows.

Shallow No measurements were possible during the initial period of very high bubble densities. There was a second peak in bubble numbers at about 2.2 s as the injected bubbles returned from their brief excursion to depth. Most bubbles were gone after 3 s. The peak in bubble numbers versus diameter is in the diameter range 0.25 cm to 0.35 cm.

Mid The concentrations peaked at 1.1 s and again at approximately 1.9 s and at diameters of order 0.30 cm. Most of the bubbles were gone after 2.5 s.

Deep Peak concentrations were from approximately 1.0 s to 1.7 s and at a diameter broadly centred on 0.25 cm. Most bubbles were gone after 2.5 s.



Figure 3.3: Freshwater plume at 1 s. (i.d 10:16, s3, lb, t1.1). Scale is the same as previous photos.



Figure 3.4: Freshwater plume at 2 s. (i.d 10:23, s3, lb, t2.2). Scale is the same as previous photos. This photo is a duplicate of the sample in Figure 3.2.



Figure 3.5: Seawater plume at 1 s. (i.d 16:18, s3, lb, t1.2). Scale is the same as previous photos.



Figure 3.6: Seawater plume at 2 s. (i.d 16:21, s3, lb, t2.3). Scale is the same as previous photos. Large numbers of small bubbles persist compared with Figure 3.4 in fresh water after the same amount of time.

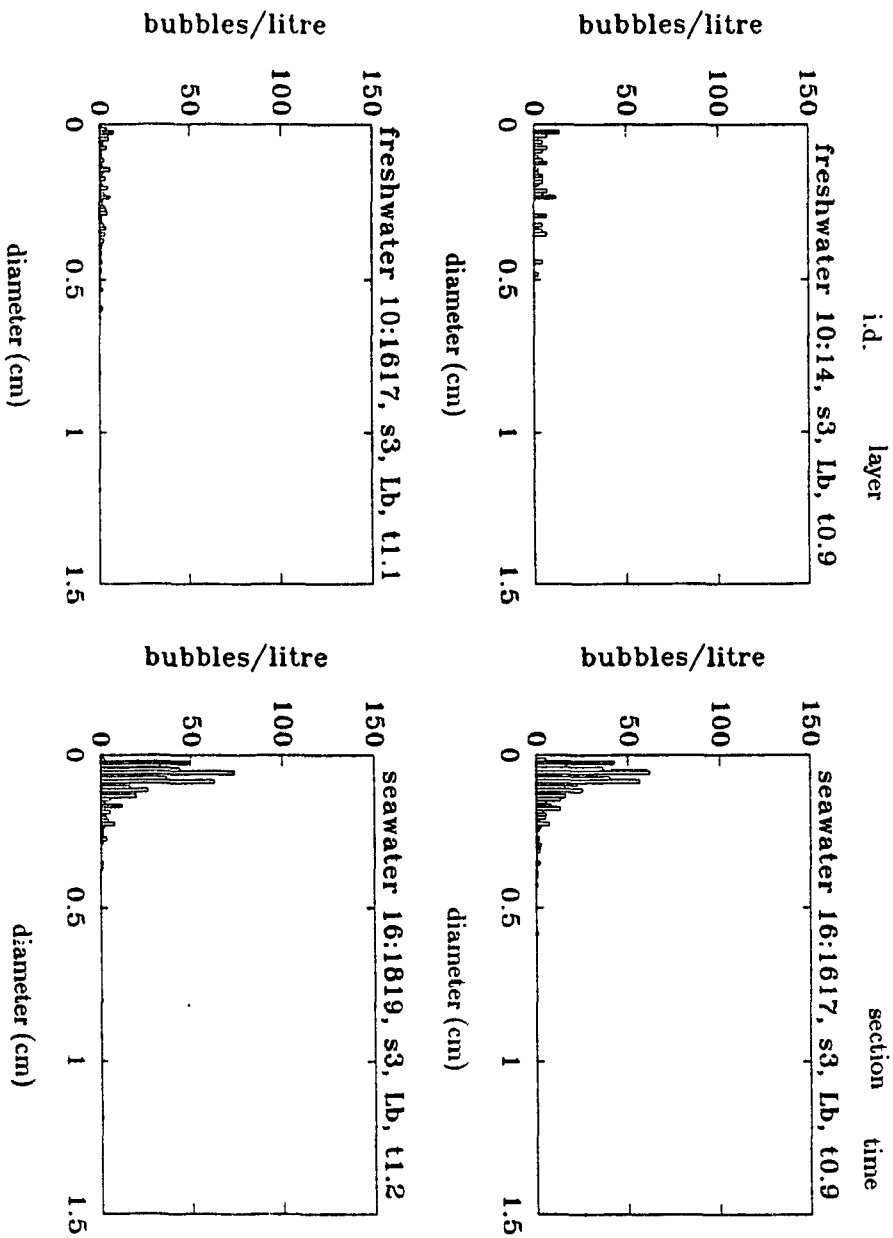


Figure 3.7: Bubble concentrations versus diameter in the centre of freshwater and seawater plumes at middepth (14cm) at corresponding and sequential times. The figure heading gives the medium (fresh water or sea water), the sample i.d., the section (s3), the layer (lb), and the time (t—variable).

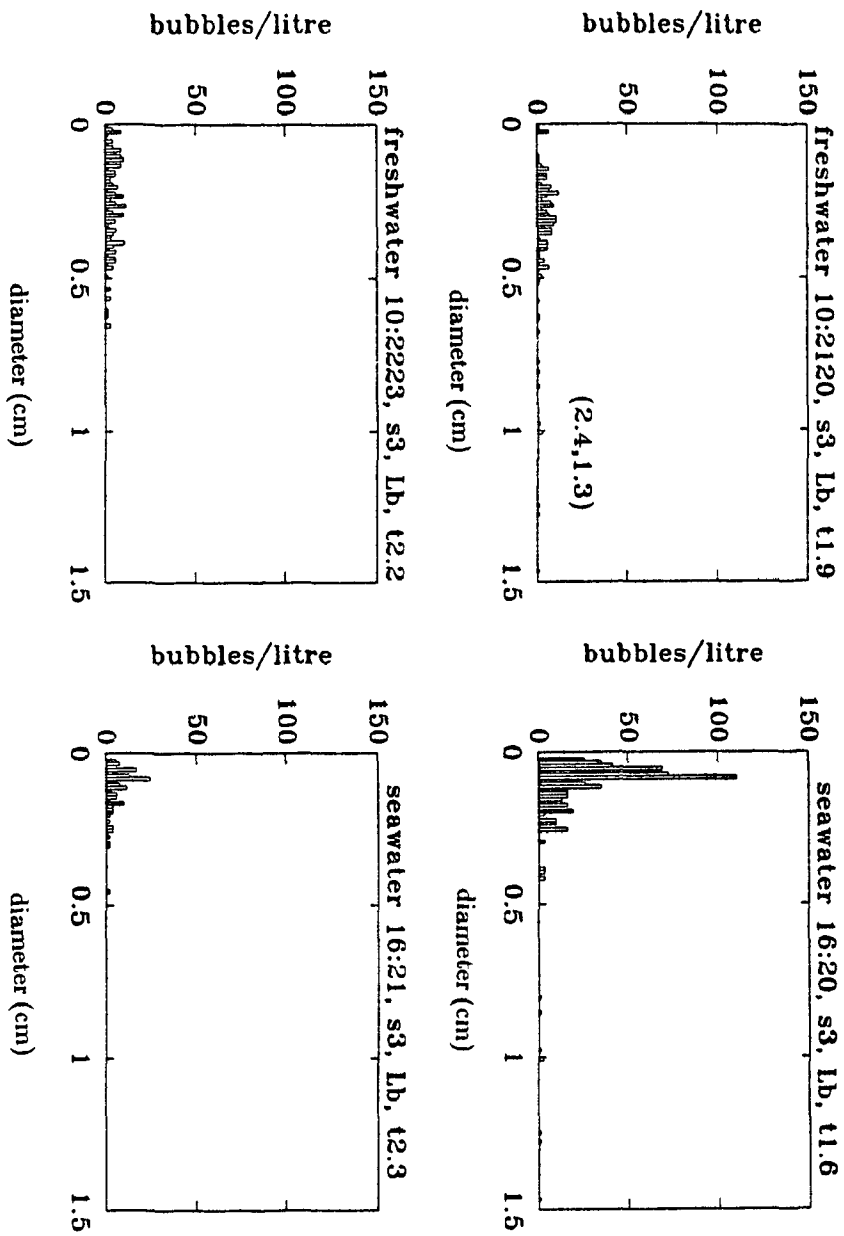


Figure 3.8: Bubble concentrations versus diameter in the centre of freshwater and seawater plumes at middepth (14cm) at corresponding and sequential times. The figure heading gives the medium (fresh water or sea water), the sample i.d., the section (s3), the layer (lb), and the time (t—variable).

Sample I.D.	t (s)	V_p (cm^3)	C_b ($N_b \text{ l}^{-1}$)	V_b ($\text{cm}^3 \text{ l}^{-1}$)	A_b ($\text{cm}^2 \text{ l}^{-1}$)	A_b/V_b (cm^{-1})
Fresh10:14	0.9	425	132	1.07	20	19
Fresh10:16,17	1.1	743	115	2.26	28	12
Fresh10:21,20	1.8	383	208	21.06	126	6
Fresh10:22,23	2.2	347	232	4.27	63	15
Sea16:16,17	0.9	563	439	0.68	19	28
Sea16:18,19	1.2	453	462	0.42	15	36
Sea16:20	1.6	317	596	0.95	28	29
Sea16:21	2.3	535	155	0.36	10	27

Table 3.1: Net bubble population properties at middepth (14cm) in the section through the middle of the plumes at time, t , after the initiation of the plume. Abbreviations: V_p , the sample volume of the photograph; C_b , concentration of bubbles, i.e. number of bubbles, N_b , per litre; V_b , A_b , sum of all bubble volumes and surface areas per litre respectively.

3.3.2 Seawater plume

Most bubbles have diameters smaller than 0.4 cm (half that of fresh water) with typical concentrations in the most populated size bins of about 100 bubbles per litre (a factor of 10 times that in fresh water). Bubbles visible to the eye persisted longer in sea water than they did in fresh water. Details of the results at the three depths are as follows.

Shallow No measurements were possible initially, but later there was a peak in concentration at about 2.7 s. Some bubbles persisted even after 5 s. The peak in bubble numbers versus diameter is in the diameter range 0.03 cm to 0.05 cm, about a tenth the corresponding fresh water value.

Mid Bubble concentrations were high from 0.9 s to 1.6 s with a significant decrease after about 2 s. The concentrations were at a maximum for bubble diameters in the range 0.06 cm to 0.09 cm.

Deep Bubbles reached this depth at about 2 s. The concentrations peaked from 2.1 s to 3.1 s and at diameters of order 0.05 cm.

3.3.3 Bubble concentration calculations

Table 3.1 summarizes some of the measured bubble population characteristics: C_b is

the total number of bubbles (N_b) per litre in the sample, V_b is the total volume per litre of all the bubbles in the sample volume, A_b is the sum of the surface areas of all the bubbles per litre and the final column is the ratio of the last two, the surface area to volume ratio. Sample volumes vary due to the time-varying thicknesses of the sample volumes that arise as described previously. The differences between the sample volumes account for at most 10–40% of the differences between any of the calculated parameter concentrations. There are typically 2.5 times as many bubbles in the sea water samples as in the corresponding fresh water samples. There are also many more small bubbles in sea water compared with fresh water by about a factor of 5 (Figure 3.7). Consequently, the bubble surface area to volume ratio in sea water is typically double that in fresh water, even though in fresh water the total volume of bubbles is an order of magnitude higher, and the total surface area of bubbles is larger.

3.4 Discussion

The comparisons in the previous sections are based on snapshots in time of bubble populations at one location in a plume that varies both spatially and temporally. While the results are hopefully representative of the general differences between the freshwater and seawater bubble populations, the following discussion shows that caution must be applied in trying to generalise the results to the whole plume over its lifetime.

3.4.1 Rise time

The entrained air entered the water as a jet and subsequently broke up into bubbles that appeared to travel together in a front. A layer of high bubble concentration was seen to first travel downwards and then reverse and rise out, becoming increasingly more dispersed over time. The nature of the development of the plume means that the early photographs primarily show descending bubbles while the later photographs primarily show bubbles that are rising out. A consideration of terminal bubble rise velocities also leads to the conclusion that many bubbles are likely to have been photographed more than once. The sampling method applies a residence-time weighting to the total numbers of bubbles observed in a population.

Rise-times of bubbles can be estimated from calculations of terminal rise velocities using the theoretical equations of Levich (1962) and Thorpe (1982) as summarized by Woolf and Thorpe (1991). Terminal rise velocities and rise times as a function of bubble diameter are illustrated in Figure 3.9. For bubbles of diameter 400 μm to 1000 μm the time to rise 10 cm in a quiescent fluid is from 1 s to 3 s, depending on the size of the bubble and the nature of its surface. Obviously fluid motions play a large role in determining the net motion of the bubbles and a usual simplification for estimating the lifetimes of bubbles is to consider them to be instantaneously injected to a certain depth from which they rise out at their terminal velocity. This approach then leads to an estimate of the plume's lifetime, based on 1000 μm diameter bubbles rising a distance of 30 cm, of 3 s to 4.5 s (Figure 3.9). The calculated residence time agrees with the observation by eye that most bubbles were gone from the shallow layer after 3 s in fresh water and about 5 s in sea water. The time for a 400 μm bubble to rise at terminal velocity a distance of 8 cm, the vertical dimension of the photographed sample volume, is from 1.8 s to 2.4 s. Consequently, as an extreme case, a 400 μm bubble might be photographed in the same layer in each of the 4 time frames over the period up to 2.4 s. In comparison, a bubble of diameter 1000 μm has a maximum calculated rise time for a distance of 8 cm of 1.2 s. Thus a 1000 μm bubble might appear, at most, in just 2 of the 4 photographs taken of the layer of interest.

The measured concentrations of bubbles in the diameter range 400 μm to 1000 μm in the simulated breaking-wave (Table 3.1) may be compared with some values from the literature. The sum of the concentrations of bubbles in the diameter range of interest averages 15 bubbles per litre in fresh water and 220 bubbles per litre in sea water. In Cipriano and Blanchard's continuous seawater waterfall the total concentration of bubbles between 400 μm and 1000 μm was about 1200 per litre at a radial distance of 12 cm from the centre of their plume (Cipriano and Blanchard, 1981). Blanchard and Woodcock (1957) captured typically 27 bubbles per litre in this size range in their bubble trap under a natural breaking sea water wave (estimated from their Figure 4 in (Cipriano and Blanchard, 1981)). The bubble concentrations at a section in the current breaking-wave simulation are somewhat higher than those observed under the natural breaking wave conditions observed by Blanchard and Woodcock, but are an order of magnitude lower than those found in the continuous waterfall simulation. A volume flow rate 1/40th of Cipriano and Blanchard's

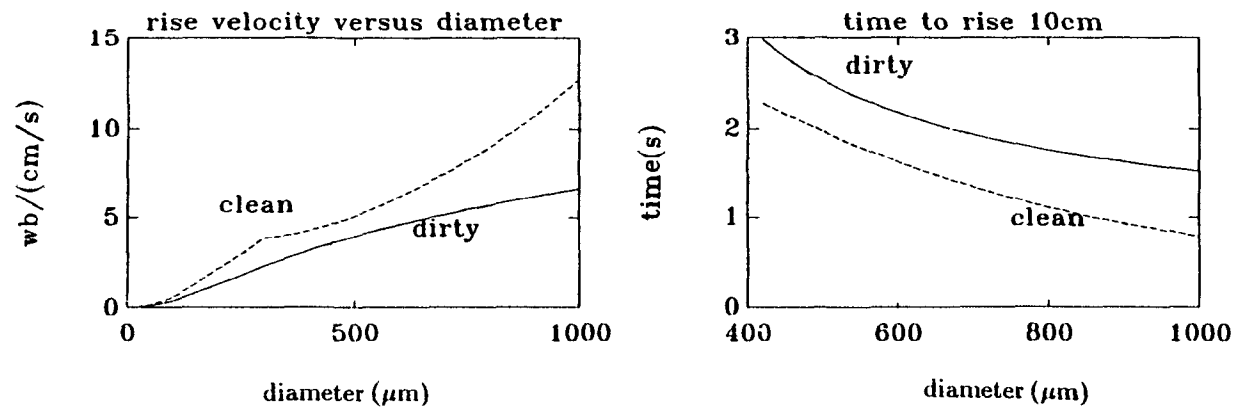


Figure 3.9: Terminal rise velocities (w_b), and rise times, as a function of bubble diameter for clean and dirty bubbles in sea water (35 psu at 10°C).

was used in these experiments.

3.4.2 Depth of focus measurements

The depth of focus is a function of bubble size. Johnson and Cooke (1979) determined a linear relationship with a depth of focus of approximately 26 mm for bubbles of diameter 200 μm increasing to approximately 51 mm for bubbles of diameter 400 μm . Johnson and Cooke used this relationship to determine their sample volumes as a function of bubble size. In the illuminated slab method the thickness of the sample volume is defined by the width of the strobe beams as they intersect and are scattered by the bubbles and is typically 5 cm. However, the smaller bubbles may be in focus, or even visible, over only a fraction of the thickness of the sample volume and, as a consequence, their concentrations may be underestimated.

A limited test of the depth of focus in my set-up was made using a similar arrangement to Johnson and Cooke as follows. A 0.010-inch diameter wire, coated with silicone grease to render it hydrophobic, was strung across a frame and suspended in a tank of water. The camera was set-up in the same way as in the plume measurements, i.e. at a distance of about 0.5 m (44 cm through air, 0.6 cm through acrylic, 8 cm through water) and a camera f-stop setting of 16. Bubbles of a range of sizes were injected into the water with a syringe. Some of these bubbles attached to the wire. Photographs were taken as the frame holding the wire and bubbles was moved 5.2 cm towards the camera in 2 mm increments. The diameter of a small bubble was determined relative to the diameter of the suspended wire in the photograph in which the images were sharpest. The bubble images in the photographs at various distances were then compared and the range of distances from camera to object for which a sufficiently distinct image was apparent was determined. A 400 μm diameter bubble had a depth of focus of 34 ± 4 mm and a 500 μm diameter bubble had a depth of focus of 46 ± 4 mm. These depth of focus values are slightly higher than those determined by Johnson and Cooke (1979).

The theoretical depth of focus, d_f , can be calculated based on optical considerations (Focal, 1969),

$$d_f = 2 \frac{cvf}{F}$$

in which c is the size of the circle of confusion, v is the distance between the lens and image,

sample I.D.	time (s)	thickness (cm)	C_b (N_b/l) $d \leq 400\mu\text{m}$	% $d \leq 400\mu\text{m}$	underestimation factor
Sea 16:16,17	0.9	6.9	36.5	11	2.0
Sea 16:18,19	1.2	5.0	39	9	1.5
Sea 16:20	1.6	3.5	19	3	1.0
Sea 16:21	2.3	5.9	7	1	1.7

Table 3.2: Examples of small bubble sampling in the seawater plume at middepth (10–18 cm). The sample volume thickness (column 3) is larger than the depth of focus for small bubbles (≈ 3.4 cm for $d = 400\mu\text{m}$) and results in underestimates of C_b , the number of bubbles per litre. The measured concentrations of bubbles with diameters less than or equal to $400\mu\text{m}$ is given in column 4. The proportion of small bubbles, as a percentage of the concentration of all measured bubbles, is given in column 5. The last column gives, as an example, a factor by which the concentration of $400\mu\text{m}$ bubbles is underestimated due to the limited depth of focus.

f is the f-number of the lens aperture and F is the focal length of the lens. The circle of confusion is related to the degree of blur that is acceptable, which is related to the size of the object because a small amount of blur may render the smallest objects practically invisible. As an example, for a circle of confusion of $100\mu\text{m}$ and the appropriate values of the other parameters, i.e. $v \approx 5000$ mm, $f=16$ and $F=50$ mm, the value of the depth of focus is 32 mm, comparable to the measured depth of focus of a $400\mu\text{m}$ diameter bubble.

Underestimates that can arise in calculations of the concentrations of the smallest bubbles, for which the depth of focus is a fraction of the slab thickness, are calculated in Table 3.2. Underestimation factors are calculated for $400\mu\text{m}$ bubbles and are proportionately larger for smaller bubbles. The problem appears to become less significant with time as the fraction of bubbles smaller than or equal to $400\mu\text{m}$ apparently decreases with time in these experiments. In general the relative proportion of small bubbles is expected to increase over time, not decrease, both because small bubbles have longer risetimes than fast-rising large bubbles and because the bubbles are presumably dissolving, although the degree of saturation of the water is unknown. The estimate of the degree to which the concentration of the smallest bubbles is underestimated is only sufficient to partially mitigate their apparent decrease over time. A likely explanation is that small bubbles become more widely dispersed than larger bubbles. Cipriano and Blanchard (1981) found this to be the

case in a similarly produced plume and also found the population of larger bubbles to be increasingly depleted with depth.

3.4.3 $C_b(d)$: bubble concentrations as a function of diameter

Review

In designing a simple laboratory model of a breaking wave, Cipriano and Blanchard (1981) reasoned that the breakup of falling water tends to produce a constant raindrop spectrum above a threshold rain intensity then, by analogy, the bubble spectrum produced by breakup of entrained air might also approach a characteristic shape. In summarizing existing field data, Wu (1981; 1988) concluded that there was indeed a universal power law (exponent -4) relating the concentration of bubbles to their size (down to some cut-off radius).

Table 3.3 summarizes additional literature findings on the relationship between the concentration of bubbles and their diameter. The tabulated value of the exponent, n , in many cases is as calculated at a later date by someone other than the original author. The more detailed recent investigations (*Baldy and Bourguel*, 1987; *Baldy*, 1988; *Hwang et al.*, 1990) suggest that the previously accepted invariant power law relationship does in fact have some variability. The value of n tends toward -2 in 'bubble generation zones' and toward an invariant -4 in deeper 'bubble dispersion zones'. The differences are considered to be largely due to the depletion of larger bubbles with depth since their buoyancy-driven rise velocities are large enough to overcome the momentum of the entraining fluid (*Baldy*, 1988). However, Medwin and Breitz's similar range of exponents did not arise from analysing bubble spectra from different zones, but by evaluating n over different diameter ranges in a single spectrum. This result suggests that other reported differences may be due to different sampling methods. However it is also true that some measurements were made under breaking waves while other spectra are acknowledged to be representative of background bubble populations. The range of n values in Cipriano and Blanchard's data depend on the radial distance from the centre of the plume, as calculated by Hsu et al. (1984). Cipriano and Blanchard (1981) themselves had noticed in a comparison of the data of Blanchard and Woodcock, Johnson and Cooke, and Kolovayev that the number of large bubbles became increasingly depleted with depth. Kolovayev (1976) noted a narrowing of the observed bubble size spectrum with depth and attributed the result to a combination of compression

Ref.	Measurement method	Location/type	d limits (μm)	peak (μm)	depth (cm)	n
B&W	bubble trap	nearshore sea/breaking-wave	750–1500	none	10	-4.7
K	bubble trap	open ocean	30–640	140	150–800	-3.5
J&C	photographic	coastal sea/background	34–610	100	75	-4.5
C&B	photo/trap	lab sea water/continuous weir	50–8000	100–300	0	-1.5, -4
B&S	photo/trap	lab fresh	20–1000	80	20	-3
B	laser	lab fresh/breaking wave	60–3000	none	8.5–45	-2, -4
M&B	acoustic	open ocean/breaking-wave	60–480	none	25	-2.5, -4
HH&W	laser	lab fresh	800–3000	900	4–10	-2, -4

Table 3.3: Sample literature determinations of the exponent, n , in $C_b \propto d^n$, where C_b is the number of bubbles per litre. The references are, in order, (*Blanchard and Woodcock*, 1957; *Kolovayev*, 1976; *Johnson and Cooke*, 1979; *Cipriano and Blanchard*, 1981; *Broecker and Siems*, 1984; *Baldy*, 1988; *Medwin and Breitz*, 1989; *Hwang et al.*, 1990). The range of bubble diameters measured is given in column 4. The diameter range where the peak concentration was observed is in column 5, where ‘none’ implies that concentrations increased with decreasing diameter down to the smallest diameter measurable. The depth at which the measurements were made is given in column 6.

sample I.D.	time	layer	n	sample I.D.	time	layer	n
Sea 16:16,17	0.9	b	-2.0	Sea 16:32-34	0.9-2.3	a	-1.6
Sea 16:18,19	1.2	b	-2.3	Sea 16:16-21	0.9-2.3	b	-2.5
Sea 16:20	1.6	b	-1.6	Sea 16:8-11	1.2-2.1	c	-1.1
Sea 16:21	2.3	b	-1.2	Sea 16:total	0.9-2.3	a+b+c	-2.2

Table 3.4: Measurements in the seawater plume of the power law exponent, n , relating bubble concentration to diameter. The left-hand columns are individual observations at a single time in layer b. The right-hand columns are the result of accumulated observations over the time ranges indicated in the three layers, first separately, and then collected.

of all bubbles due to hydrostatic pressures and bubble dissolution. In addition large bubbles penetrate to a shallower depth compared with small bubbles.

Existing comparisons between natural seawater and freshwater bubble populations have been limited to acoustic signatures of bubble clouds in an enclosed freshwater loch compared with an open ocean site (*Thorpe, 1982*). The effects of air-water temperature differences (*Hwang et al., 1991*), the degree of saturation of the water (*Thorpe, 1982; Woolf and Thorpe, 1991*) and the presence of organic materials on the bubble spectra remain to be thoroughly investigated.

Results

The exponent, n , of the power law relationship was evaluated for a subset of the data as the slope of log bubble concentration versus log bubble diameter for bubble diameters greater than $500 \mu\text{m}$ (Figure 3.10). The left side of Table 3.4 shows the variation in n over time at one position in the seawater plume. The uncertainty in n is greater at later times because there are fewer bubbles in the populations. If the decrease in n with time is real, it is contrary to what might be expected just from depleting the water of the fast-rising large bubbles. The decreasing n with time rather suggests that small bubbles are disappearing more rapidly than large bubbles. This would be consistent with undersampling of the smallest bubbles, both because they are increasingly more widely dispersed with time, and because of their small depth of focus (as discussed in section 3.4.2). Some small bubbles may also be ‘lost’ through shrinkage by dissolution into bubble sizes that are too small to be measured by this method. There were insufficient bubbles and otherwise too much noise

to calculate reliable exponents from other single time and space observations. When all the data from the tabulated time series in layer b are accumulated the resulting value of n is -2.4. This value, along with the values calculated from the accumulated time series in layers a and c, are tabulated on the right hand side of Table 3.4. When the data from all three depths, over the time frames 0.9 s to 2.3 s, are accumulated, n equals -2.2. Values of n around -2 are consistent with the observations in bubble generation zones of other investigators (Table 3.3). The bubble spectrum is shown in Figure 3.10, along with the spectrum from the accumulated freshwater data. The freshwater spectrum has a maximum concentration at diameters around 2.3 cm and the slope calculated from diameters larger than the maximum has a value -2.7, quite similar to the value from the seawater population, -2.2, measured over a quite different range of bubble diameters.

3.4.4 $C_b(z)$: bubble concentrations as a function of depth

Review

Wu (1981) concluded from a comparison of the photographic measurements of Johnson and Cooke (1979) and Kolovayev (1976) that near the sea surface the total bubble concentration decreased exponentially with increasing depth. Thorpe's acoustic data also showed an exponential decay in acoustic cross-section per unit volume over length scales of 40 cm to 85 cm, the scale being dependent on conditions (Thorpe, 1982). Crawford and Farmer (1987) inferred the same relationship from their acoustic data with e -folding depths of 0.7 m to 1.5 m, depending on wind speed. Laboratory breaking-wave experiments also confirmed a general exponential decay and determined that the entrainment depth, whether it is defined as an e -folding depth or a 50% level, scales on the order of the significant wave height (Hsu *et al.*, 1984; Baldy and Bourguel, 1987; Baldy, 1988). This was also determined to be the case in further interpretation by Hwang *et al.* (1990) of the data of Johnson and Cooke (1979) and Thorpe (1982; 1986). Hwang *et al.* (1990) also suggested that there was an effect of temperature on entrainment depth.

The overall picture is of an exponential decrease in the concentration of bubbles with depth, but experimental details of the relative numbers of different size fractions are not yet available. Bubble populations are likely to be sensitive to contaminants, temperature and saturation levels, as single bubble dissolution studies have found (Detsch, 1990).

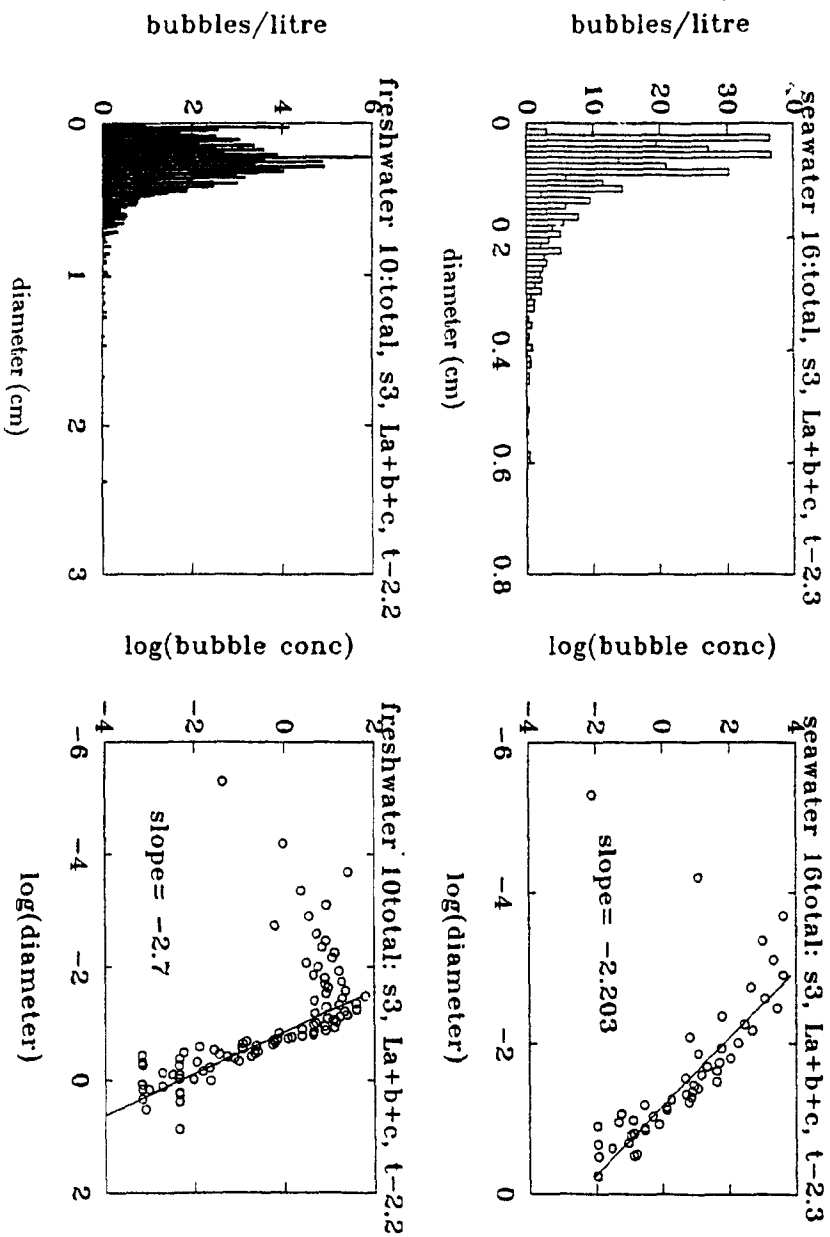


Figure 3.10: Bubble concentration versus bubble diameter for seawater (top) and freshwater (bottom) plume populations; histograms on the left and the same information in log-log form on the right. Note the different scales between the freshwater and seawater histograms in both bubble concentration and bubble size. The data are those accumulated from the midsection of the plume (section 3, layers a+b+c, and all times sampled up to about 2.3 s). The reported slopes (equal to n) are those calculated from diameters larger than that corresponding to the peak in bubble concentration.

Results

Just as bubble plume penetration depths are found to scale as the source wave height, the entrainment depth in the tank experiments is expected to scale as the height from which the water fell. This information was used in my design in which water fell from a height of about 70 cm above the water surface into water that was about 32 cm deep. Bubbles reached the bottom of the tank.

Figure 3.11 shows that total bubble concentration versus depth through the middle of the plume is approximately bounded at all times by $C_b = C_{b0} \exp(-z/z_b)$ with $z_b=20$ cm, $C_{b0}=100$ and 500 as the lower and upper limits in fresh water and $C_{b0}=300$ and 1100 as the lower and upper limits in sea water.

The data are too scattered to determine a value of the e -folding depth, but they do demonstrate that a value of 20 cm is reasonable. There are insufficient data to determine if the e -folding depth in sea water is different from that in fresh water. In all cases the value of C_b is overestimated at the shallowest depth by the exponential decay expression compared with the actual measurements. The measurements are likely underestimates, because the bubbles disperse as they rise. While the numbers of bubbles may be higher at the surface, if they are less densely packed the snapshot at one cross-section will not reveal the higher bubble numbers. Also this photographic method underestimates the number of very small bubbles.

3.5 Summary

In this chapter the techniques used to generate and measure the bubble populations in a simulated breaking-wave have been described. This work represents the first detailed photographic comparison of freshwater and seawater bubble populations produced by a simulated breaking-wave. Significant differences were observed between the populations in the seawater plume compared with the freshwater plume: the bubbles were more numerous, smaller, and were present longer in the seawater plume compared with the freshwater plume. However, undersampling of the smallest bubbles by the photographic/illuminated-slab method did not allow a completely quantitative comparison to be made between the two media. Observations of bubble concentrations as a function of size and as a function of depth in

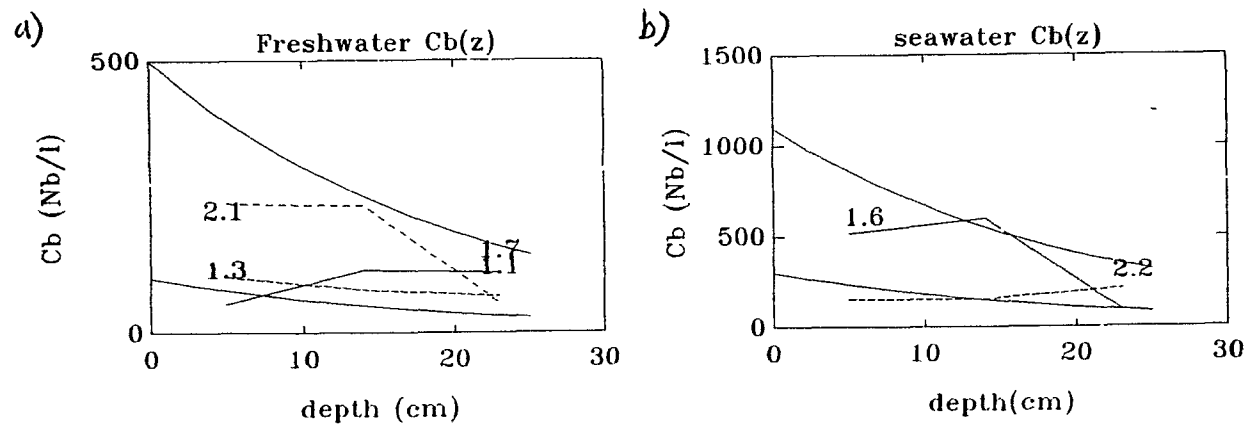


Figure 3.11: Bubble concentrations versus depth measured in the a) freshwater, and b) seawater plumes, at times indicated (in seconds). Bounding curves are of form $C_{b0} \exp(-z/z_b)$.

the water, despite their limitations, were generally consistent with other observations reviewed in the literature. The results give confidence that the intermittent waterfall provides a satisfactory simulation of natural bubble-injection processes.

Chapter 4

A Gas Tension Method for Studying Flux Across a Gas-Water Interface

4.1 Introduction

A gas tension device and its application in laboratory studies of gas transfer is described in this chapter. A portion of this material also appears in Anderson and Johnson (1992). In essence the gas tension device, GTD, provides a dissolved gas pressure measurement in water analogous to a barometric pressure measurement in the atmosphere. The prototype GTD incorporates a solid-state differential pressure sensor that measures the difference between these two gas pressures; one port of the sensor measures the pressure of dissolved gas ('gas tension', for succinctness) and the reference port measures barometric pressure of the overlying gas phase. When the gas-phase pressure is also separately recorded, the gas tension can be calculated. Then, the rate of change of gas tension relative to the gas pressure in the overlying atmosphere measures the rate of gas transfer into, or out of, the water parcel. The differential pressure between phases at steady state measures the degree of saturation of the water. It is apparent from the discussion of gas flux models in Chapter 1 that the direct measurement of degree of gas saturation is extremely valuable. In particular, steady-state supersaturations are an indicator of the role of bubbles in the

gas transfer process.

Since the gas tension method determines the physical property of gas pressure, rather than any chemical gas property, it is possible to conduct single-gas experiments with a range of gases covering widely differing solubilities and diffusivities. Results from different experimental configurations using He, Ar, N₂ and CO₂ are initially reported in this chapter and will be analysed in Chapter 6, following development of a depth-dependent bubble flux model in Chapter 5.

4.2 The Gas Tension Device

4.2.1 Physical description

The essential features of the GTD are illustrated in Figure 4.1 in an exploded view. The pvc cylinder is approximately 13 cm in length by 5 cm in diameter. The membrane surface area is 12.6 cm². The solid-state pressure sensor weighs 5 g and is 2 cm long. The body sections are screwed together while the endcap is attached with suitcase clips, allowing for easy replacement of the membrane.

Gas passes from the water through a gas-permeable membrane into a small sensing volume behind the membrane. The membrane is a 0.0127-cm-thick silicone elastomer product of the Dow Corning Corporation. The sensing volume equilibrates with the dissolved gas pressure in the surrounding water and the signal port of the differential pressure sensor measures this gas tension. The gas-permeable membrane is stretched over a 0.0102-cm-thick silver filter and is secured with the o-ringed endcap. The silver filter, supplied by Flotronics of Spring House, Pennsylvania, has a 74% void volume. This spacer ensures communication of the entire membrane area with the signal port centered in the end of the instrument body. A smooth rigid pvc disk acts as support for the filter and membrane. The rigid support-disk resists deformation of the membrane in response to hydrostatic pressure changes. The brass signal port of the sensor fits into an o-ringed cavity in the underside of the support-disk and is connected to the main sensing volume by a hole 0.5 mm in diameter. The sensing volume comprises the void volume of the support as well as space inside the signal port and its o-ringed cavity, and sensor. The void volume has been minimized to ensure fast response, e.g., by fitting a plastic insert with a small inner bore into the brass

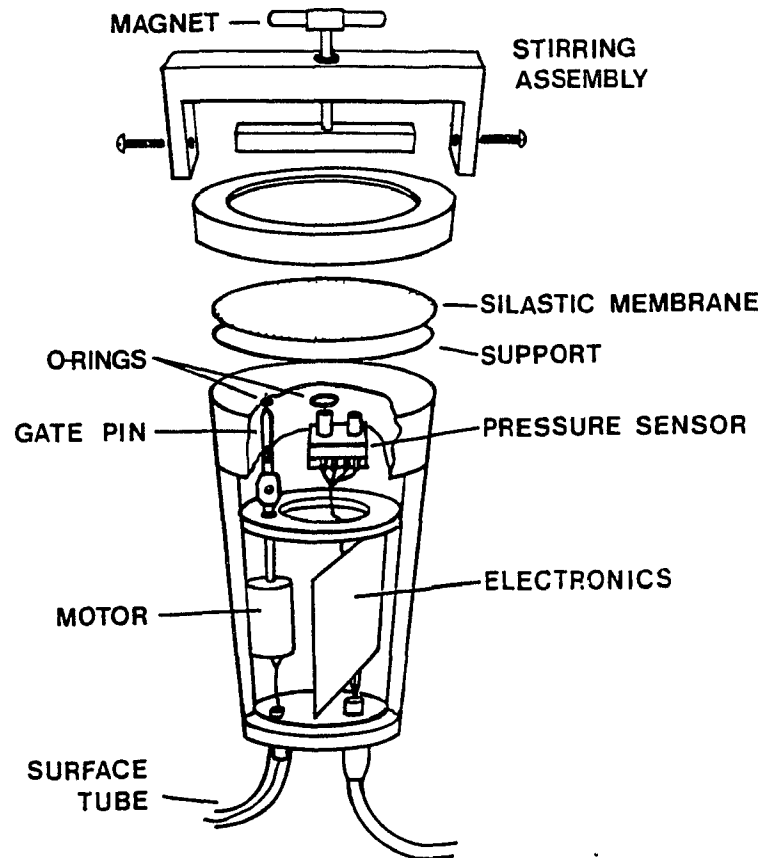


Figure 4.1: Exploded view of the gas tension device (GTD). Approximate dimensions are 13 cm length by 5 cm diameter. The Silastic (TM) membrane is a 0.0127-cm-thick product of Dow Corning Corporation. The support illustrated beneath the membrane is a 0.0102-cm-thick silver filter with 74% void volume. The solid-state differential pressure sensor is SenSym (1989, product LX06001D). The pressure gate separates the sensing volume from the body of the instrument. A magnetically-driven stirrer is attached.

pressure port. An attached magnetically-driven stirrer keeps water moving over the surface of the membrane.

The solid-state differential pressure sensor, SenSym™ model LX06001D, has a range of ± 1 psi (± 7 kPa, 70 mbar) with a rated sensitivity of 0.4 mV mbar^{-1} and is temperature compensated (*SenSym*, 1989). The electronics package in the GTD amplifies the signal using a 5 volt reference and buffers the output voltage. Assuming that responses are due to gas pressure changes only, the voltage output is

$$V = r(P - p) + V_0, \quad (4.1)$$

where r is a calibration ratio, $P - p$ is gas tension less gas-phase pressure, and V_0 is an offset voltage. The offset voltage at zero differential pressure, V_0 , was measured at intervals by opening a motorized pressure ‘gate’ to expose both signal and reference ports to the same pressure, p . Figure 4.2 is a schematic of the pressure sensing arrangement indicating the reference port connection to the gas phase. The ‘gate’ is a pin that may be tightened screw-wise up against a small o-ring to seal the connection to the sensing volume. The pin is driven by a 12-volt DC motor. Typically V_0 is in the range $+0.30 \text{ V}$ to $+0.67 \text{ V}$ and drift is not significant over the course of a few days.

4.2.2 Calibration

Calibration was made by manually applying small pressure increments directly to the sensor’s signal port with a syringe and recording the voltage output versus applied pressure as measured by manometer. The details of the calibration exercise are given in Appendix A. A linear relation between manometer fluid position and pressure was used to calculate a voltage to pressure proportionality ratio, r , of $0.213 \pm 0.006 \text{ V mbar}^{-1}$ ($n=16$, $R^2=0.9997$) over the measured range -3 V to $+6 \text{ V}$.

4.2.3 Theoretical response

When a gas-water system is in steady state, $P - p$ is constant and there is no net gas flux between the phases. When the system is perturbed, for example by applying and maintaining a step change to p , subsequent changes in $P - p$ over time give information

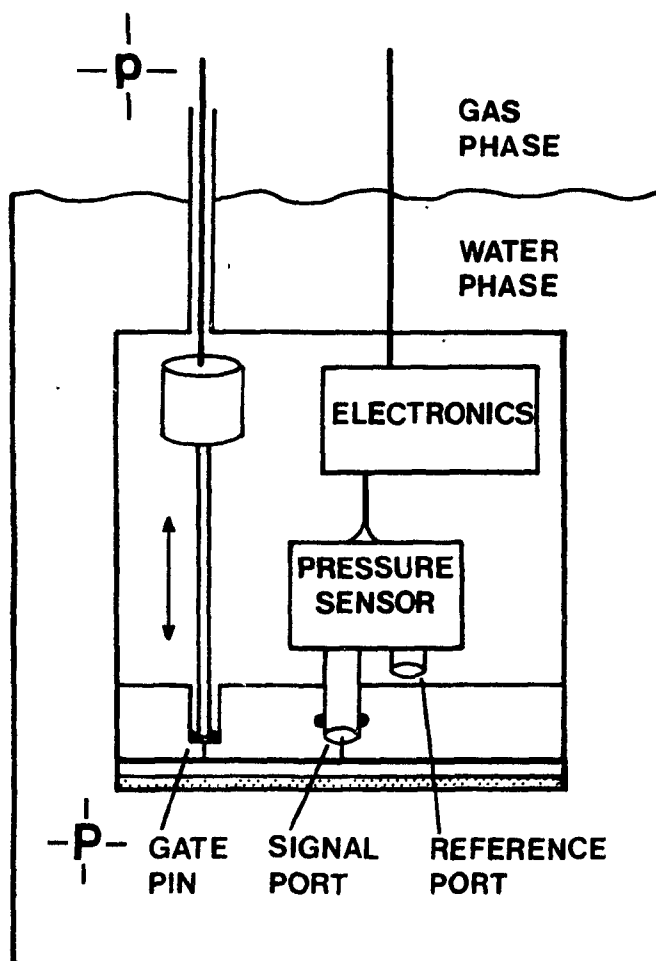


Figure 4.2: Schematic of the GTD pressure-sensing mechanism. The signal port measures a gas pressure in the sensing volume equal to gas tension in the surrounding water, P . The reference port measures gas pressure in the body of the device, equal to gas pressure p above the water. Opening and closing the motorized pressure gate allows measurement of the zero-offset voltage and instrument response time.

about the gas exchange rate (from the time derivative of $P - p$) and the net gas exchange (from the time integral of $P - p$).

Figure 4.3 illustrates the theoretical response of the GTD to gas fluxes induced by step changes applied to the gas-phase pressure. The uppermost figures illustrate time series of the controlled variable — gas-phase pressure; on the left (a) a step increase is applied to induce gas invasion into the water; on the right (b) a step decrease is applied to induce gas evasion from the water. The voltage response of the system, previously at steady-state, is illustrated directly below in each case (c and d). The offsets from zero volts at the beginning and end of the voltage time series are due to V_0 and any steady-state supersaturation. As long as conditions supporting supersaturation (e.g. bubble injection) are unchanged, the value of the offset will be unchanged. Supersaturations are represented by a positive voltage after V_0 is subtracted from V (equation 4.1). The step change in p results in a step change in V of magnitude rp , where r is the calibration ratio. Subsequently a gas flux into the water (illustrated in the LH sequence) or out of the water (illustrated in the RH sequence) restores the gas tensions to values in steady-state with the applied gas-phase pressures. The voltages exponentially return to steady-state values. Gas tensions can be explicitly determined when p , V_0 , and r are known; P is sketched in Figures 4.3 e and f.

4.2.4 Response time

The instrument response time is the time required for the sensing volume to equilibrate with the gas pressure in the surrounding water.

The high gas permeability and inertness of Silastic™ make it the material of choice for artificial lungs (*Galletti et al.*, 1966) and recommend it for the gas tension device. Teflon filters, with their naturally hydrophobic surface, were first tested, but found to be unable to support the necessary hydrostatic pressures. Gas transfer through the membrane is described as solubility controlled rather than diffusion controlled and transfer rates for different gases vary according to their ‘solubility’ in the material. Published values range from (units $\text{cm}^3(\text{STP}) \text{ s}^{-1} \text{ cm}^{-2}$ (area) $\text{atm}^{-1} \text{ cm}^{-1}$ (thickness) at 25°C) 4.14 for CO_2 to 0.39 for N_2 , with values for O_2 and He in between at 0.79 and 0.48 respectively (*Galletti et al.*, 1966). A volume of gas equal to the sensing volume of the instrument ($v_s = 0.22 \text{ cm}^3 \text{ s}^{-1}$) would diffuse through the GTD membrane (area $A = 12.6 \text{ cm}^2$, thickness $\delta_m = 0.0127$

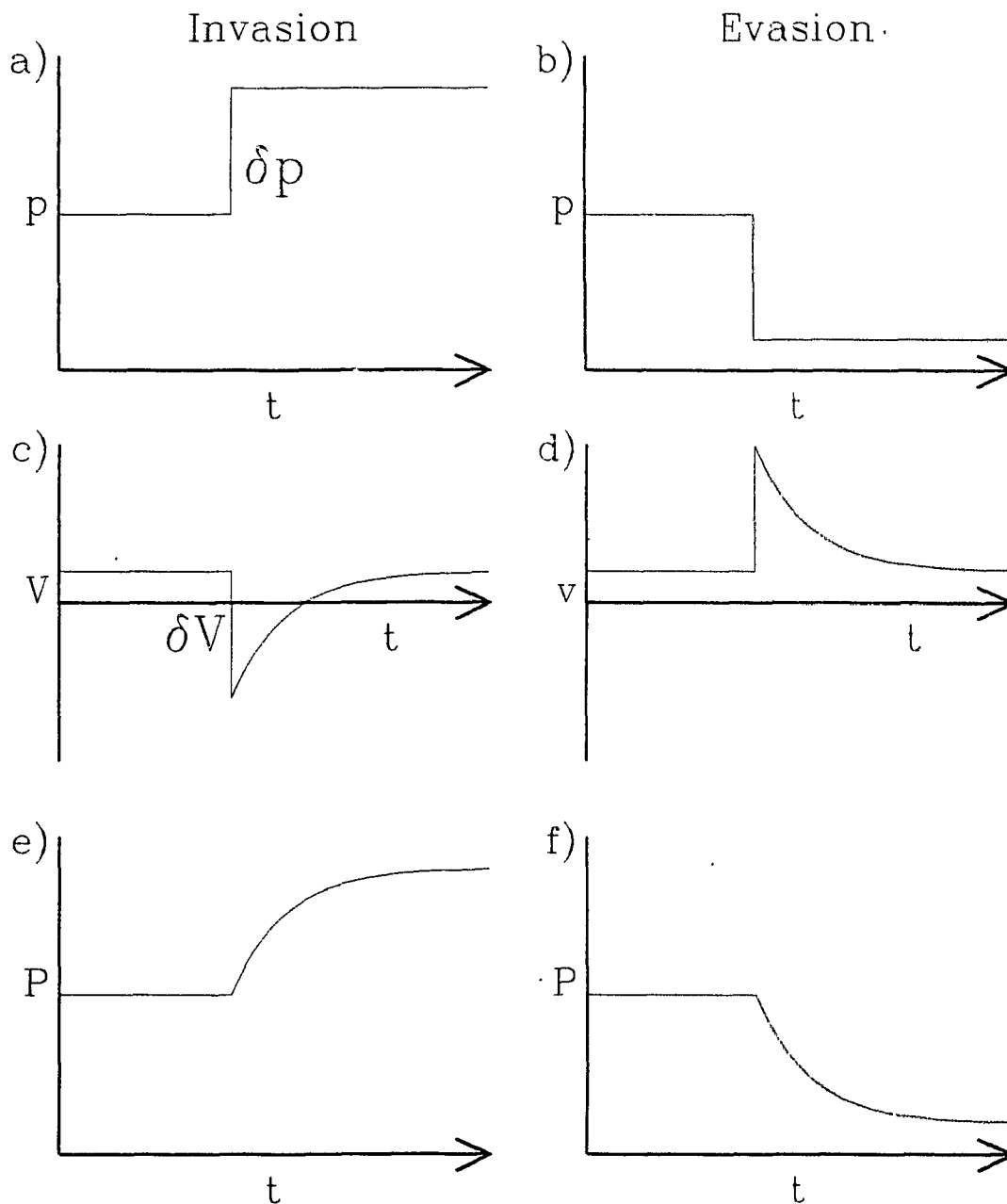


Figure 4.3: Theoretical GTD response. The topmost figures illustrate time series of the controlled variable — gas-phase pressure; on the left (a) a step increase is applied; on the right (b) a step decrease is applied. GTD voltage response of the previously at steady-state system is simulated directly below in each case (c and d). The offset from zero volts at the beginning and end of the time series is due to V_0 and any steady-state supersaturation. The step change in p is seen as a step change in V of magnitude τp , (τ is the calibration ratio). Subsequently a gas flux into the water (LH sequence) or out of the water (RH sequence) gradually restores the gas tension (e, f) to a value in steady-state with the new gas-phase pressure.

cm) in 0.3 s (CO_2) to 3.5 s (N_2) at 1 atm pressure. The contribution to instrument response time for gas transfer through the membrane, τ_m , is therefore estimated at 3.5 s. The estimate is a minimum because it is derived from constants determined for diffusion into a gas space swept free of the diffusing gas, whereas there is a buildup of diffusing gas in the sensing volume of the instrument.

Calculation of the contribution to instrument response time of transfer across the water boundary layer next to the membrane, τ_w , is made based on the film model for transfer across a boundary layer. Equating

$$F = \frac{D}{\delta} \Delta c. \quad (4.2)$$

and

$$F = \frac{v_S}{A} \frac{dc}{dt} \quad (4.3)$$

where D is the diffusion constant for the gas in water, the thickness of the boundary layer is δ_w , and Δc is the concentration step across the layer, it follows that the time constant

$$\tau_w = v_S \delta / AD. \quad (4.4)$$

Diffusion constants for gases in water are small, about $10^{-9} \text{ m}^2 \text{ s}^{-1}$, so to minimize the response time of the instrument the thickness of the hydrodynamic boundary layer, and consequently the diffusive boundary layer, is reduced by stirring the water next to the membrane with a paddle attached to a magnetically-driven stirring bar. Schlichting (1955) defines the thickness of the hydrodynamic boundary layer, δ_0 , as the height for which the deviation of the peripheral velocity is 2%. For the case of a rotating fluid next to a stationary disk

$$\delta_0 = 8 \sqrt{\frac{\nu}{\omega}},$$

where ν is the kinematic viscosity and ω is the angular velocity. Schlichting's solutions show that the thickness of the hydrodynamic boundary layer is twice as thick for a rotating fluid next to a rotating plate as compared with the similar case of a stationary fluid next to a rotating disk. Levich (1962) discusses the relative importance of convective diffusion to molecular diffusion in transport through a fluid to an adjacent surface. In determining boundary layer thickness, molecular diffusion in a diffusive boundary layer is analogous to viscosity in a hydrodynamic boundary layer. The coefficient of diffusion, D , is about 1000 times smaller than the coefficient of viscosity, ν , and therefore the thickness of the diffusive

boundary layer, δ , is much smaller than δ_0 . Levich (1962) solves the equations for convective diffusion and molecular diffusion next to a rotating disk in stationary flow. Levich's result for the thickness of the diffusive boundary layer is multiplied by a factor of 2 to give the theoretical expression relevant for a stirrer rotating water next to a stationary membrane,

$$\delta = 3.22 \left(\frac{D}{\nu} \right)^{1/3} \sqrt{\frac{\nu}{\omega}}.$$

Substituting $D = 2 \times 10^{-5} \text{ cm}^2 \text{ s}^{-1}$ for the diffusivity of N_2 in water at 24°C , $\nu = 10^{-2} \text{ cm}^2 \text{ s}^{-1}$ for the kinematic viscosity of water and $\omega = 30 \text{ s}^{-1}$ for the measured angular velocity of the magnetic stirring bar and hence fluid, the boundary layer is calculated to be $75 \mu\text{m}$. Diffusivities of most gases are similar, but that for He is approximately a factor of 4 larger and consequently the boundary layer for He is about 1.5 times as thick. Subsequently τ_w is estimated at 7 s (3 s for He) by substitution of the relevant parameters in equation 4.4. The estimate is a minimum, with uncertainty due primarily to difficulty in measuring the contributions to v_S , the sensing volume. If the response time, t_{90} , is defined as

$$t_{90} = -(\tau_m + \tau_w) \ln(1 - .90), \quad (4.5)$$

i.e., the time required for 90% of the concentration step to be registered, then the calculated value of t_{90} ranges from approximately 14 s for He to 24 s for N_2 . The calculated values are compared with measured values in section 4.5.

Conditions that drive gas exchange in the ocean, for example atmospheric pressure variations and changes in sea state, occur on the time scale of hours. For example, during the passage of a severe storm atmospheric pressure may drop by 4% (40 mbar) in 20 hours. The GTD response time is sufficiently short in comparison to time constants for these forcing processes. The GTD is sensitive to pressure changes of just ± 0.05 mbar (0.005% of standard atmospheric pressure) whereas the most sensitive chemical methods for measurement of dissolved gas concentrations have precisions of order 0.2% under the best sampling conditions, e.g., Winkler titrations for oxygen, gas stripping followed by gas chromatography or mass spectrometry. The GTD gives continuous measurements and is suitable for mooring. Other methods require discrete sampling and ship-board analyses that become increasingly difficult under the storm conditions of most interest.

4.3 Experimental Program

4.3.1 Apparatus

The experimental tank is illustrated in Figure 4.4. The dimensions of the cylindrical acrylic tank are 1.5 m \times 0.45 m diameter. All fittings except for the pump inlet are through the lid of the tank. The o-ringed lid is secured to the tank with suitcase clips.

Temperature-controlled water was recirculated through copper coils arranged around the inside perimeter of the tank. The coils are shown in a different orientation in Figure 4.4 for clarity. The copper coils are spray painted with an inert paint to retard contamination of the water. Gas passes through copper coils held in the temperature-controlled bath before entering the tank. The outside of the tank is layered with dense foam insulation to a thickness of approximately 4 cm. Temperature measurements are made with a platinum resistance thermometer with a precision of 0.005°C. The thermometer probe is fitted to a stainless steel tube that is o-ringed through the lid of the tank and allows the probe to be raised and lowered to record both gas and water temperatures. Typically temperatures are held constant during an experiment to within $\pm 0.02^\circ\text{C}$. The pressure sensor in the GTD is internally temperature-compensated. The main concern in temperature control was over the possible effect of gas-water temperature differences on gas exchange rates (*Phillips, 1991; Robertson and Watson, 1992*). Temperature effects are discussed in Chapter 7. Bubble populations may also be affected by air-water temperature differences (*Thorpe et al., 1992; Hwang et al., 1991*).

Gas-phase pressure is controlled by a gauge pressure controller on the inlet gas line that ensures that the gas pressure inside the tank is always maintained above ambient atmospheric pressure. A Cartesian diver-type pressure controller, available from Cole-Palmer, was used. Step changes can be applied to the gas-phase pressure in the tank by adjusting the setting of the controller. The size of the adjustment required to change the pressure by a particular amount was determined by trial and error. In addition, the gas flow rate often required adjustment when the pressure setting was changed. The gauge pressure controller ensures that there are no leaks of air into the system and does not require a perfectly gas-tight tank. A disadvantage of this arrangement is that the gas pressure inside the tank will not be held absolutely constant, but rather will be maintained at a constant

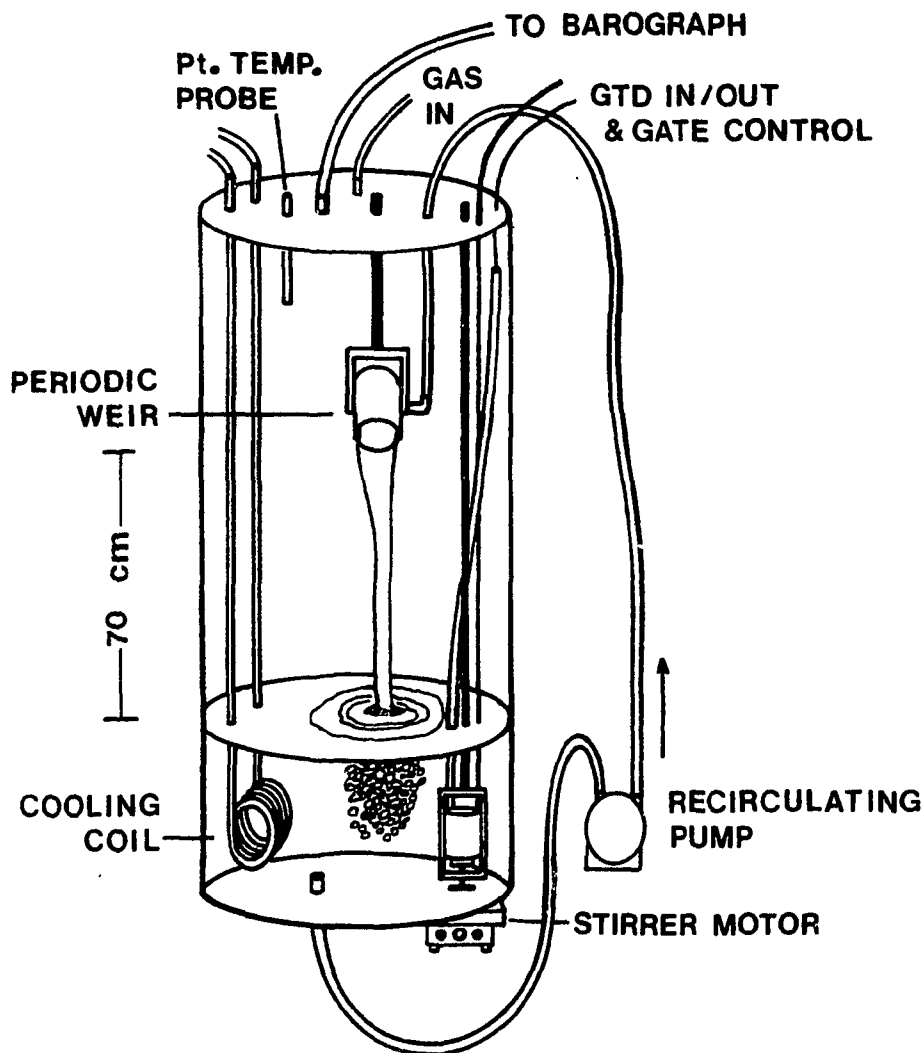


Figure 4.4: Apparatus: tank, 1.5 m×0.45 m diameter acrylic, insulated; mixing, magnetic stirrer next to membrane and recirculation of water via peristaltic pump to periodic weir. Bucket typically dumps 0.8 l from 70 cm above the water surface every 90 s. Gas-phase pressure is controlled by a gauge-pressure controller on the inlet line; measurement is by barograph. Temperature is controlled by circulating temperature-controlled water through copper coils; measurement (to 0.005°C) is by a platinum resistance thermometer that can be moved between phases. GTD has input from the power supply and output to the multimeter and chart recorder.

level above ambient atmospheric pressure. Changes in atmospheric pressure may be of comparable magnitude to the step changes applied to the gas phase to initiate a gas exchange experiment and this causes difficulties. For example, an experiment begun as an evasion experiment could have the driving force for evasion dramatically reduced by a subsequent rise in atmospheric pressure, leaving only very small signals to measure.

Gas-phase pressure is measured by a barograph in a bell jar connected to the main tank. The barograph was kindly supplied by the Atmospheric Environment Service of Canada, in Bedford, Nova Scotia. The barograph chart was changed on a three day cycle and can be read to ± 0.1 mbar on a 1 mbar scale. The experiments are referred to as single-gas experiments, but obviously water vapour pressure is also present. However, being a function of temperature and, to a lesser extent salinity, water vapour pressure has very nearly the same value in each phase. Saturation of the gas phase with water vapour is assumed so there is no net contribution to the measured differential pressure changes.

The GTD is supported just off the bottom of the tank, above a magnetic motor that stirs water across the membrane. Typically 48 l of water is added to the tank to a depth of approximately 30 cm. For experiments in which bubble injection is desired, the water is withdrawn through the bottom of the tank and pumped via a peristaltic pump to a bucket balanced 70 cm above the water surface. Thick-walled Masterflex (TM Cole-Parmer Instrument Company) tubing made of Norprene (TM Norton Company) was used. The bucket becomes unstable upon filling and periodically (every 69 s to 90 s) pivots forward and dumps approximately 770 to 820 cm³ of water in a bubbly plume that reaches the bottom of the tank.

Continuous measurements of p , V , and temperature (T_w or T_g) are recorded on strip charts. Data points are also recorded manually during the rapidly changing periods of the experiments to help synchronize the voltage and pressure records. The pressure record on the barograph suffers from poor time resolution and gas pressure data quality was considerably improved when recorded manually. The pen on the barograph also tended to stick and more reliable results were obtained by tapping the bell jar containing the barograph immediately before taking a reading. All of the data are discretised when they are manually transferred to computer files.

4.3.2 Variables

Gas exchange experiments were carried out in sea water and fresh water with the gases He, N₂, Ar and CO₂. Most of the experiments were carried out with bubble injection provided by the simulated breaking-wave. Both invasion and evasion experiments were carried out under the bubble injection conditions. A number of experiments were carried out in ‘null’ mode, where the only mixing was provided by the GTD’s magnetic stirrer. A few experiments were carried out with the water being circulated through the pump in the same manner as for the breaking-wave, except that on re-entering the tank the water bypassed the tipper and simply flowed through a hose back into the main reservoir.

The freshwater experiments, in the order that they were carried out, are listed in Table 4.1. The seawater series follow in Table 4.2. The length of time that the water (depth d_m) was initially charged with gas is listed. Charging was done in the initial stages with the gas entering through a frit directly into the water and the lid of the tank ajar. Later, the gas inlet would be taken out of the water, the intermittent waterfall turned on, and the system pressurized and occasionally vented to the atmosphere. Comments in the column titled ‘Notes’ indicate when certain improvements were introduced to the method, e.g. when bell-jar insulation was added, or when problems were noticed. Some experiments listed under the I (invasion) column were to measure the response to turning on the bubble-injection — noted as ‘wave-on’ experiments. Similarly a few ‘wave-off’ experiments were also done which doubled as ‘null’ experiments. Gas-phase pressure changes superimposed by atmospheric pressure variations due to the relative nature of the pressure controlling system frequently meant that an experiment that was started as an evasion experiment became an invasion experiment. This was especially true under the ‘null’ conditions and meant that categorization of ‘null’ experiments as invasion or evasion was not possible. High variability in gas-phase pressure was one cause of poor data quality, as discussed in the results section.

FRESH WATER			
Bubble Injection		Null	Notes
I	E		
N ₂ , charged 3 days, $d_m = 25.8$ cm, 40 l			
57	58		T control poor
59	60	61, 62, 64 ^a , 65, 66	^a wave-off
67	68		Insulation added to bell jar &
69	70	71, 72	T, p_{H_2O} meas. added
He, charged 5 days, $d_m = 31.0$ cm, 48 l			
74 ^b		73	^b wave-on
75	76		
77	78		
79		80 ^a , 81 ^c 82 ^d , 83 ^c	^c discontinuities in V ^d large Δp_{H_2O}
Ar, charged 3 days, $d_m = 31.0$ cm, 48 l			
84 ^c	85		^c charged only 24h
86	87		
88		89 ^a , 90, 91, 92	
CO ₂ , charged 3 days, $d_m = 31.0$ cm, 48 l			
94			
96	97		
98	99	01	

Table 4.1: Record of freshwater experiments showing the range of gases and conditions (I= 'invasion' and E= 'evasion') under which experiments (identified by numbers 57-01) were carried out. Sudden discontinuities observed in the voltage record in experiment 81 were of unknown origin. See text for additional information.

SEA WATER				
Bubble Injection		Null	Circ'u	Notes
I	E			
Ar, charged 8 days, $d_m = 35.0$ cm, 54.3 l, S= 22 psu.				
03 ^b	04	02		^b wave-on
05	06			
07				
08	09	10 ^a		
N ₂ , charged 8 days, $d_m = 30.8$ cm, 47.8 l, S= 22 psu.				
11 ^c	12	12		^c wave stopped
N ₂ , charged 3 days, $d_m = 31.2$ cm, 48.3 l, S= 31.2 psu.				
15 ^b		13 ^d , 14		^d large Δp_{H_2O}
16	17 ^c			
18		19 ^a	20, 21	
He, charged 3 days, $d_m = 31.2$ cm, 48.3 l, S= 31.2 psu.				
23 ^e		24 ^e	22 ^e	^e Problematical - 'ballooning' ^f Gas inlet under water
25 ^f	26 ^f			
27 ^f				
29 ^f	30 ^f	31 ^f		
33 ^b				
34	35			
36	37	38 ^a	39	
CO ₂ , charged 2 days, $d_m = 31.2$ cm, 48.3 l, S= 31.2 psu.				
40 ^g	41 ^g			^g stirrer malfunction
42	43			
44	45	46 ^a , 47	48, 49	

Table 4.2: Record of seawater experiments showing the range of gases and conditions (I= 'invasion' and E= 'evasion') under which experiments (identified by numbers 02-49) were carried out. Salinity is recorded in practical salinity units (psu). After difficulties in response were noted, the membrane was found to have 'ballooned' outwards, probably as a result of the excessive supersaturations achieved. See text for additional information.

4.4 Gas-Exchange Results

4.4.1 Example: CO₂ invasion into sea water with bubble injection.

Duplicate experiments investigating the uptake of CO₂ into seawater with bubble injection are now presented as an example of the gas tension method.

In sea water, dissolved CO₂ dissociates into the inorganic ions HCO₃⁻ and CO₃²⁻ and this dissociation can, in some cases, affect the rate of uptake of CO₂ (*Bolin, 1960; Hoover and Berkshire, 1969; Quinn and Otto, 1971; Emerson, 1975*). The extent to which dissociation occurs is largely a function of pH. Over pH ranges of normal sea water, less than 1% of the CO₂ is present in its dissolved gas form while at pH < 5 it is almost completely in dissolved form (*Skirrow, 1975*). In the laboratory experiments an atmosphere of pure CO₂ is used. Sea water in equilibrium with pure CO₂ at one atmosphere has a calculated pH of 5.2; the pH of the tank water was measured at 5.0. Therefore limited dissociation into carbonate ions occurred and models predict that the uptake of CO₂ was not enhanced. The transfer time across the boundary layer under turbulent conditions is short compared with the time constant for dissociation for CO₂, so no enhancement of the rate of CO₂ uptake due to the chemical reactivity of CO₂ is expected (*Hoover and Berkshire, 1969; Liss, 1973; Liss, 1983*).

Filtered seawater (0.2 μm, salinity 31.2 practical salinity units (psu)) was used in these experiments and the 48.3 l filled the tank to a depth of 31 cm. The system was purged and equilibrated over 70 h with CO₂ in the manner described previously prior to the start of the experiments. Atmospheric pressure variations were small over the relatively short duration of these two experiments. The water temperature was controlled to 22.98±0.01°C and the gas-phase temperature was 22.95±0.01°C.

In the first run, a 25-mbar (2%) increase in CO₂ gas-phase pressure was applied at time zero that remained to within 3 mbar over 400 min (Figure 4.5). The raw GTD voltage initially dropped (Figure 4.5) (since voltage is proportional to $P - p$). Subsequently the voltage increased exponentially, the result expected from a gas flux into the water. Gas tension is evaluated by adding p , as recorded by the barograph, to the differential pressure calculated from V using the measured values of r (0.213 V mbar⁻¹) and V_0 (+0.40V).

The steady-state supersaturation is evaluated at about 10 mbar, or 1%. The value is modest, yet the GTD provides a sensitive measurement. The important consequence that

a nonzero flux can exist, even at the point where the gas pressure difference between the gas phase and the water phase is zero, is demonstrated in the experiment. From Figure 4.5, the e -folding time for the gas flux to restore the voltage is approximately 105 min.

4.4.2 Further results

A selection of plots showing the GTD response under a variety of experimental conditions is presented. The i.d. of the experiment indicates the conditions: S for sea water, F for fresh water; I for invasion, E for evasion; W for 'wave-breaking', N for 'null' mixing, C for 'circulation-only'. The steady-state supersaturation, s^0 , is estimated from the value of $P - p$ ($(V - V_0)/r$) at long times.

1. Experiment S.CO₂.IW44 (Figure 4.6) is a duplicate of the experiment described in section 4.4.1 — CO₂ invasion into sea water with bubble injection. The gas-phase pressure, p , was not sustained at the high setting and consequently the voltage response appears to approach equilibrium faster than it otherwise would, because of the component of p in the voltage. Gradually varying gas-phase pressures, a consequence of ambient atmospheric variations on the gauge-pressure controller, are typical of experimental conditions. Time constants calculated directly from the voltage response are not accurate under changing p conditions and ultimately another method is used. An estimate for the time constant for gas exchange from Figure 4.6*b*, not taking into account p changes, is 105 min.
2. Experiment S.CO₂.EW43 (Figure 4.7) is an example of CO₂ *evasion* from sea water with bubble injection. This evasion experiment can be compared with the previous invasion experiments. The response is flatter at the beginning than expected and is typical of the results of many evasion experiments. A time constant of order 100 min is estimated, not taking into account p changes, and s^0 is about 10 mbar.
3. Experiment S.He.IW29 (Figure 4.8) is an example of *He* invasion into sea water with bubble injection. This experiment can be compared with the CO₂ experiments under the same conditions. The time constant for voltage recovery is about 75 min, not taking into account p changes, and s^0 is estimated at about 10 mbar.

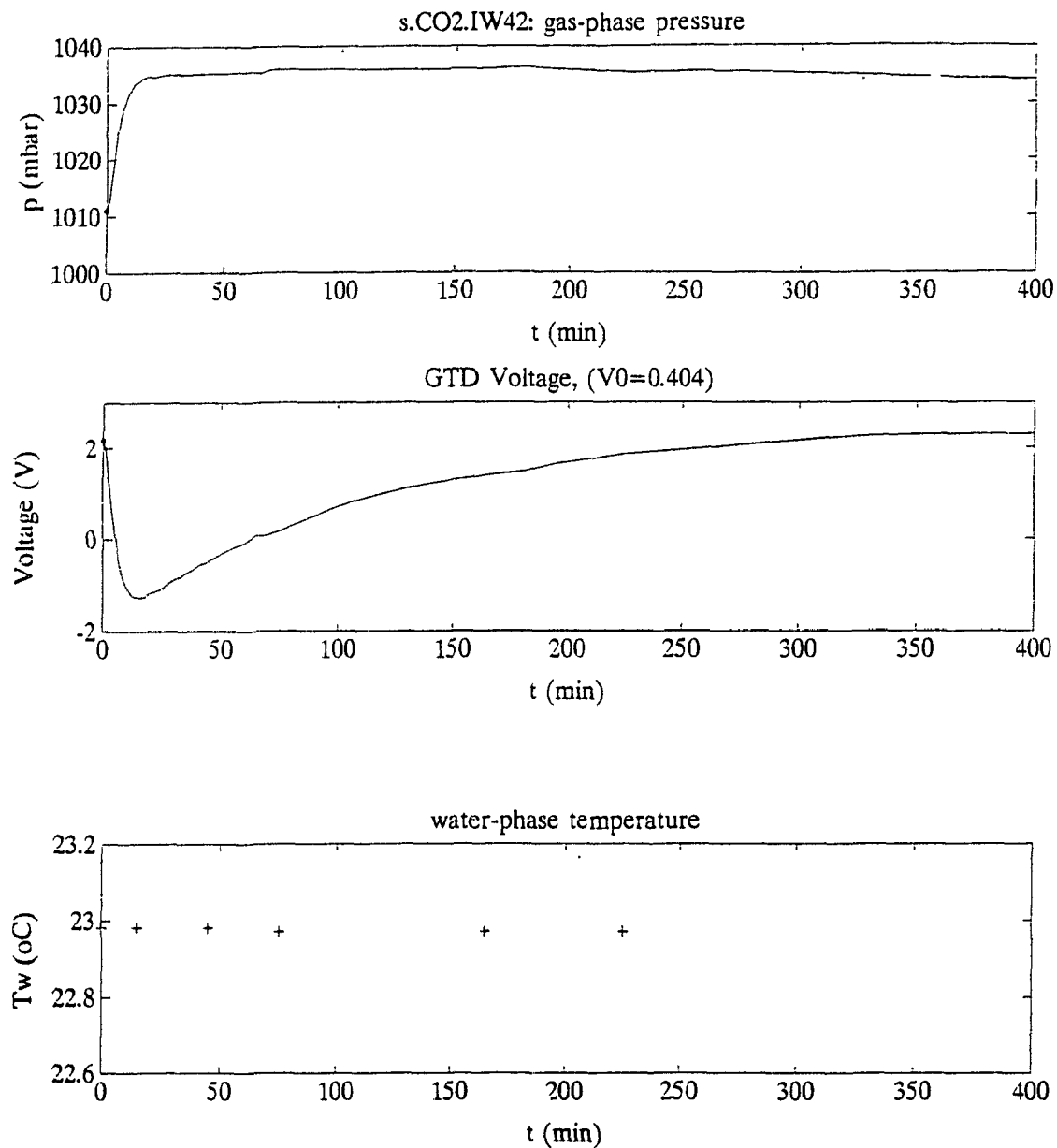


Figure 4.5: CO₂ invasion experiment: raw data. The gas-phase pressure, p , is illustrated, showing the step increase applied starting at time zero. Below is the raw GTD voltage, showing the response to the increase in p and subsequent rise in gas tension. The results compare well with the predicted response illustrated in Figure 4.3. Water temperature, T_w , is given in the third plot.

4. Experiment F.He.IW77 (Figure 4.9) is an example of He invasion into *fresh* water with bubble injection. This experiment can be compared with the He experiment in sea water. The experiment did not run long enough for steady-state conditions to be reached. For s^0 estimated at 4.5 mbar, a time constant of 190 min is estimated. This seems abnormally high — longer than for He in S and for CO₂. Analysis of another F.He.IW experiment had an estimated time constant of 100 min, not taking into account p changes, and s^0 of 3 mbar.
5. Experiment F.N₂.IW67 (Figure 4.10) is an example of N₂ invasion into fresh water with bubble injection. This experiment can be compared with the experiment with He under the same conditions. For an estimated s^0 of 5mbar the time constant is estimated at 100 min, not taking into account p changes.
6. Experiment F.N₂.IN62 (Figure 4.11) is an example of N₂ invasion into fresh water under *null* mixing conditions. This can be compared with the N₂ experiment carried out with ‘wave-breaking’. The step increase applied to p is eroded over the course of observations and most of the changes in the voltage record are due to changes in p . It does appear that the s^0 is around zero millibars, as expected when steady state is in fact an equilibrium condition. Explicit calculation of P shows gas tension increasing, although initially in a rather unrealistic fashion. Responses of this nature are investigated further in terms of the instrument response to hydrostatic pressure changes (section 4.6). The temperature, as measured in the gas phase, increased by approximately 1°C over the experiment, a large amount compared with later experiments with improved bell-jar insulation.
7. Experiment S.N₂.IC20 (Figure 4.12) is an example of N₂ invasion into sea water with ‘*circulating*’ conditions. This experiment can be compared with the N₂ experiments carried out in both null and ‘wave-breaking’ modes, although the null experiment was in fresh water. There doesn’t seem to be any voltage recovery in response to the step change applied in p . The likely reason is that the system was not in steady state previously and the applied change in p actually brought the system closer to equilibrium, effectively removing any driving force for gas exchange. In addition, the gas exchange under circulation conditions may also be very slow. However, when p

was subsequently dropped by nearly 40 mbar to try to induce evasion, there was again no subsequent change in V after the initial change. It appears that the GTD became insensitive to gas tension changes (see below).

The illustrated examples are generally similar to the theoretical response discussed in section 4.2.3. Departures occur when p is not maintained at a fairly constant level, and are particularly apparent for the experiments where gas exchange is slow. The 'null' and 'circulation' experiments are difficult to interpret at this simple level, largely for this reason. For the experiments conducted under breaking-wave conditions, a slightly supersaturated steady state is reached with a time constant of order 100 minutes. The time constants for the gas exchange are about 30 times larger than the theoretical time constants for instrument response time.

The earlier experiments were generally run until it appeared steady-state conditions were reached. The experiments conducted later were frequently not continued for such a long period. The signal-to-noise ratio deteriorates as the driving force for gas exchange becomes small. When a steady state is not established, a simplistic interpretation of the time series is not reliable. All of the experiments will be analysed in detail following development of a model in Chapter 5.

The volume of the bell jar constitutes about 30% of the gas volume of the system and temperature control of the system was significantly improved when the bell jar was insulated. The bell jar was isolated from the tank for change-over of the barograph chart every 3 days, unavoidably interrupting the longer experiments.

On a number of occasions the GTD appeared to become unresponsive. If the GTD became completely unresponsive it was usually an indication that there was water leaking in around an improperly sealed o-ring, ultimately affecting the electronics. On other occasions however the GTD seemed to respond to p changes, but not to changes in P , i.e. would respond to hydrostatic changes to the exclusion of gas tension changes. A dramatic example of this was when the seawater system was first charged with He. The response in the first three experiments was suspicious and subsequent inspection found that the membrane had 'ballooned' outwards. This and other incidents lead to the conclusion that problems tended to occur when gas tension was high compared with the total hydrostatic pressure. It is the hydrostatic pressure that forces the membrane up against its support. In the ballooning

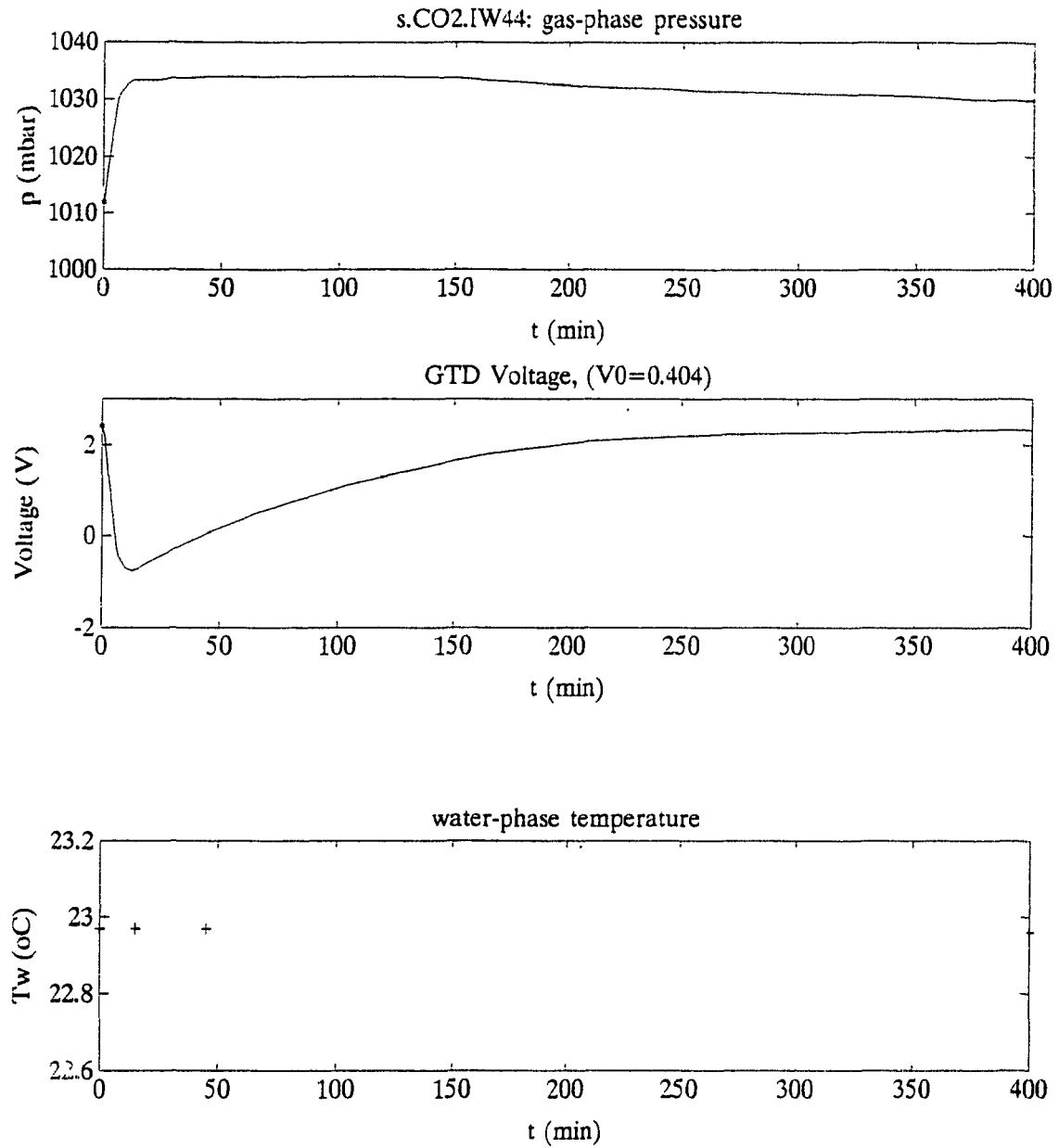


Figure 4.6: CO_2 invasion into sea water with bubble injection. Time series of (top) gas-phase pressure, raw GTD voltage, and (bottom) water temperature, T_w .

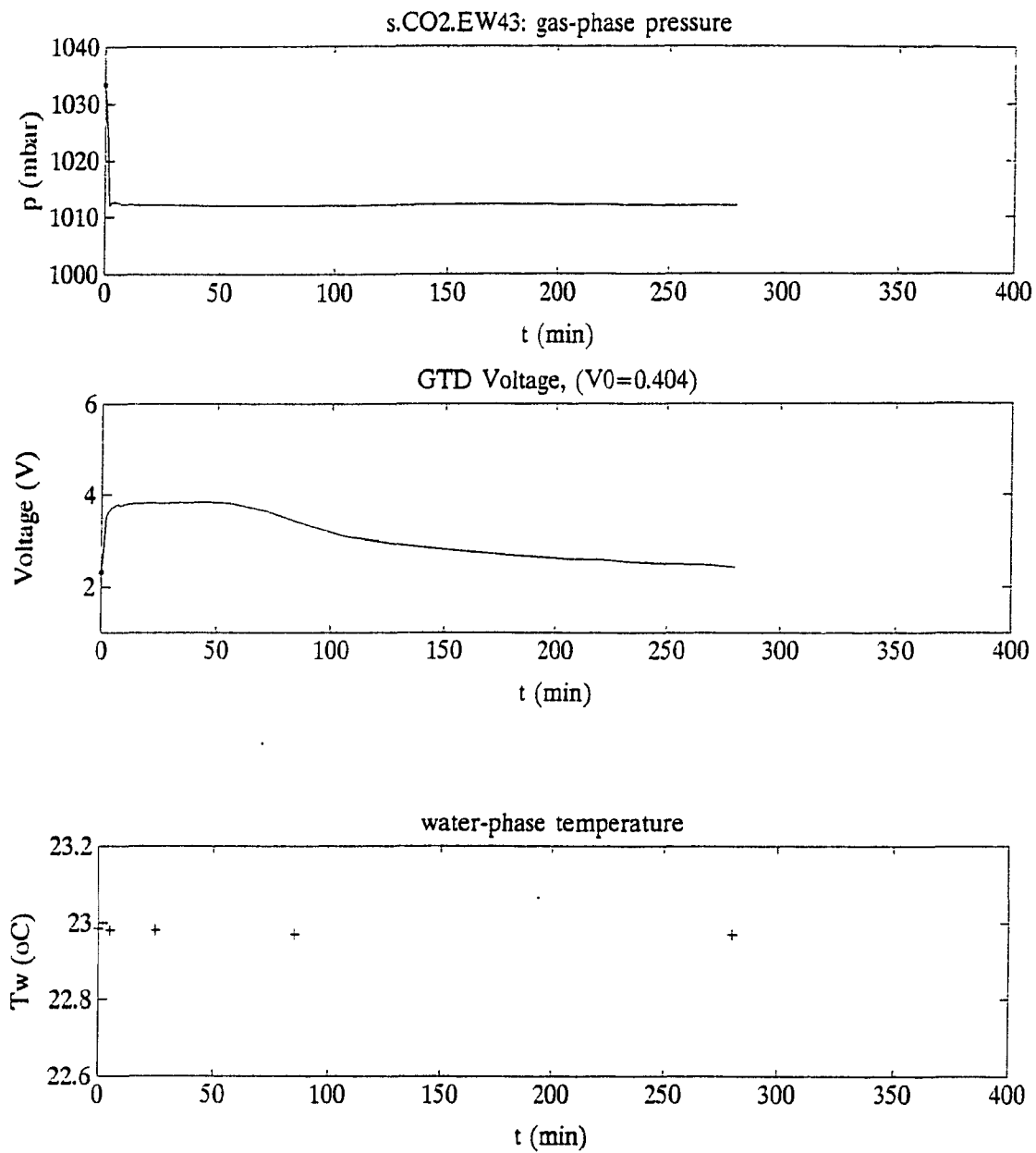


Figure 4.7: CO_2 evasion from sea water with bubble injection. Time series of (top) gas-phase pressure, raw GTD voltage, and (bottom) water temperature, T_w .

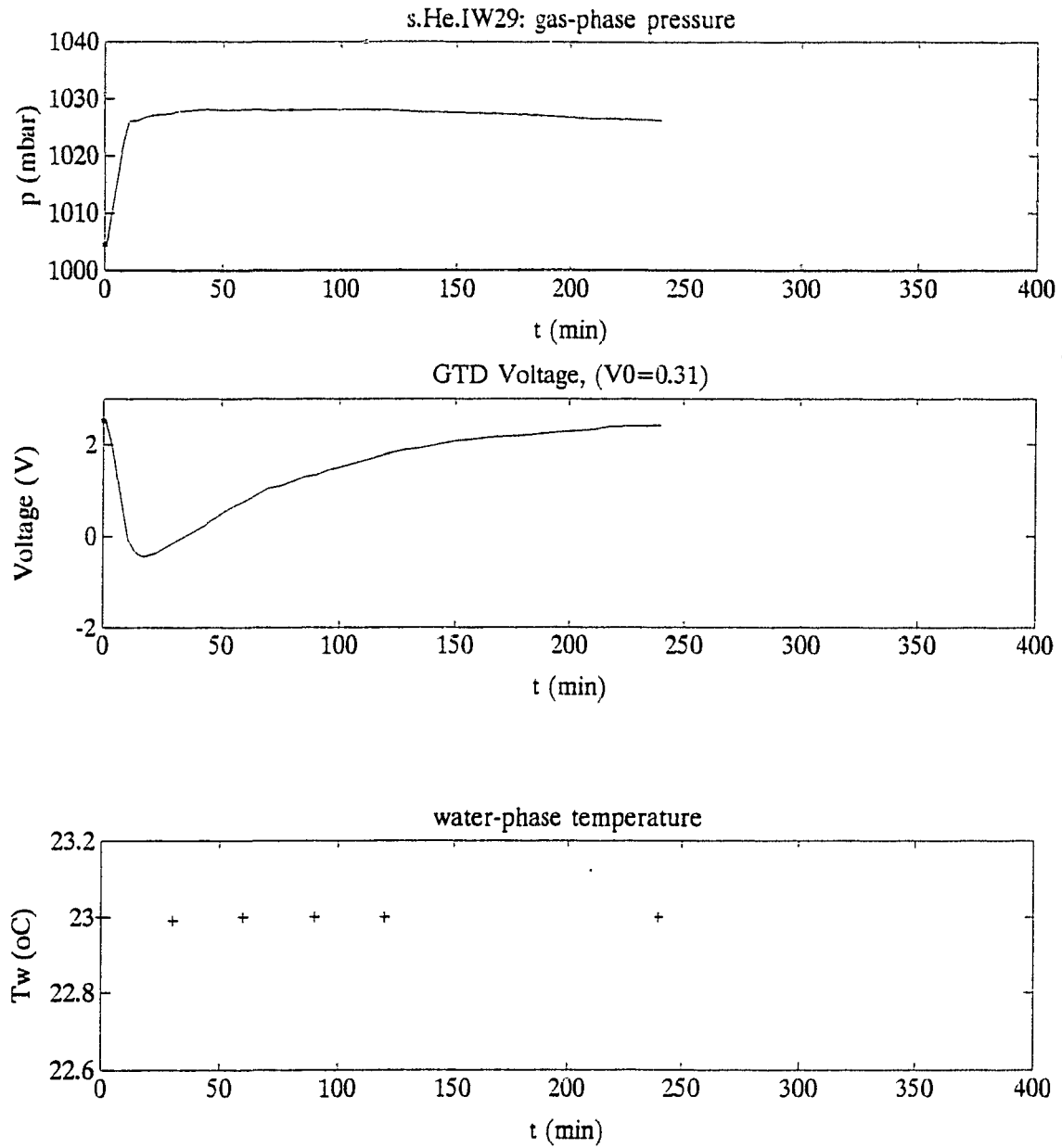


Figure 4.8: He invasion into sea water with bubble injection. Time series of (top) gas-phase pressure, raw GTD voltage, and (bottom) water temperature, T_w .

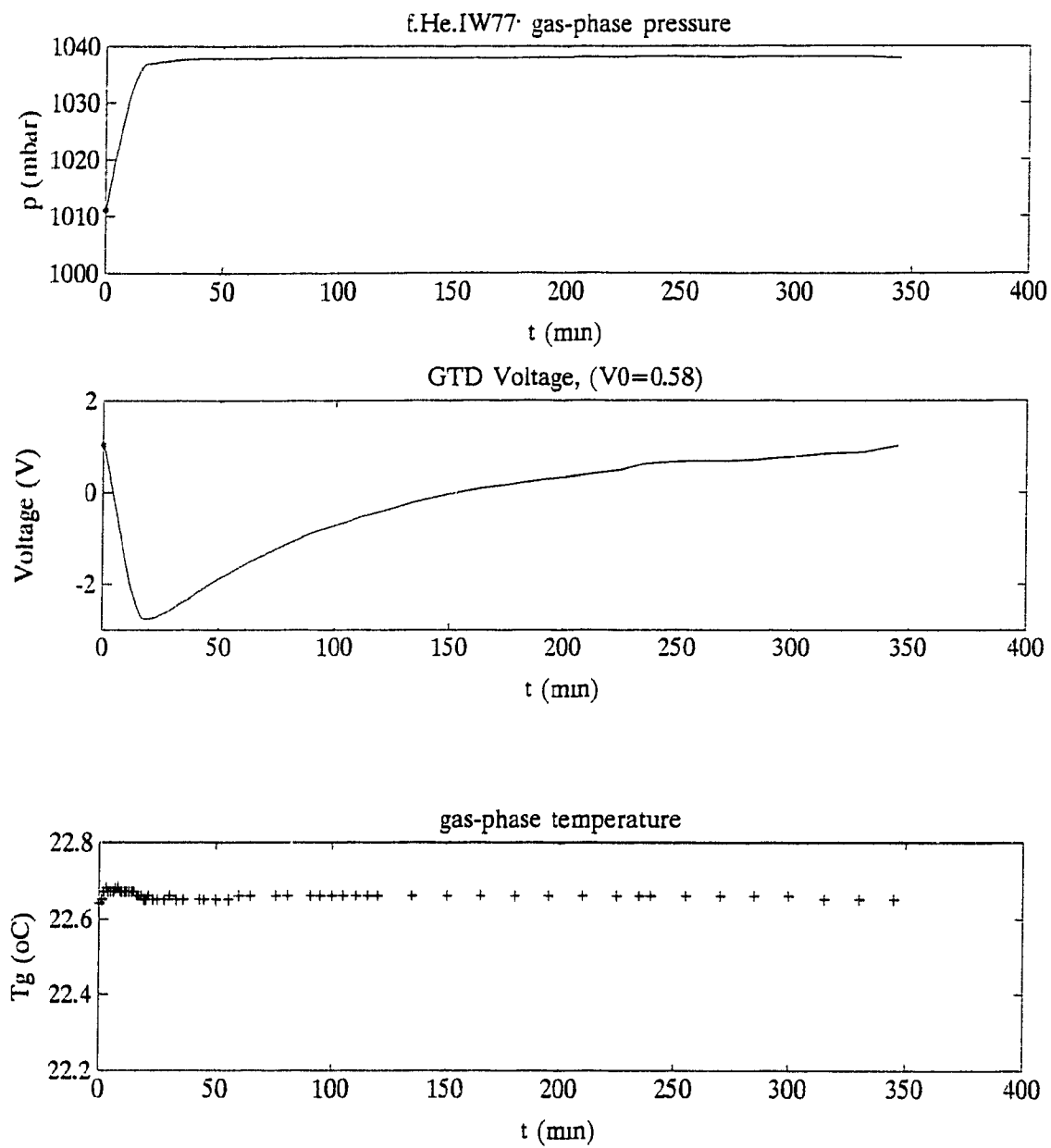


Figure 4.9: He invasion into fresh water with bubble injection. Time series of (top) gas-phase pressure, raw GTD voltage, and (bottom) gas-phase temperature, T_g .

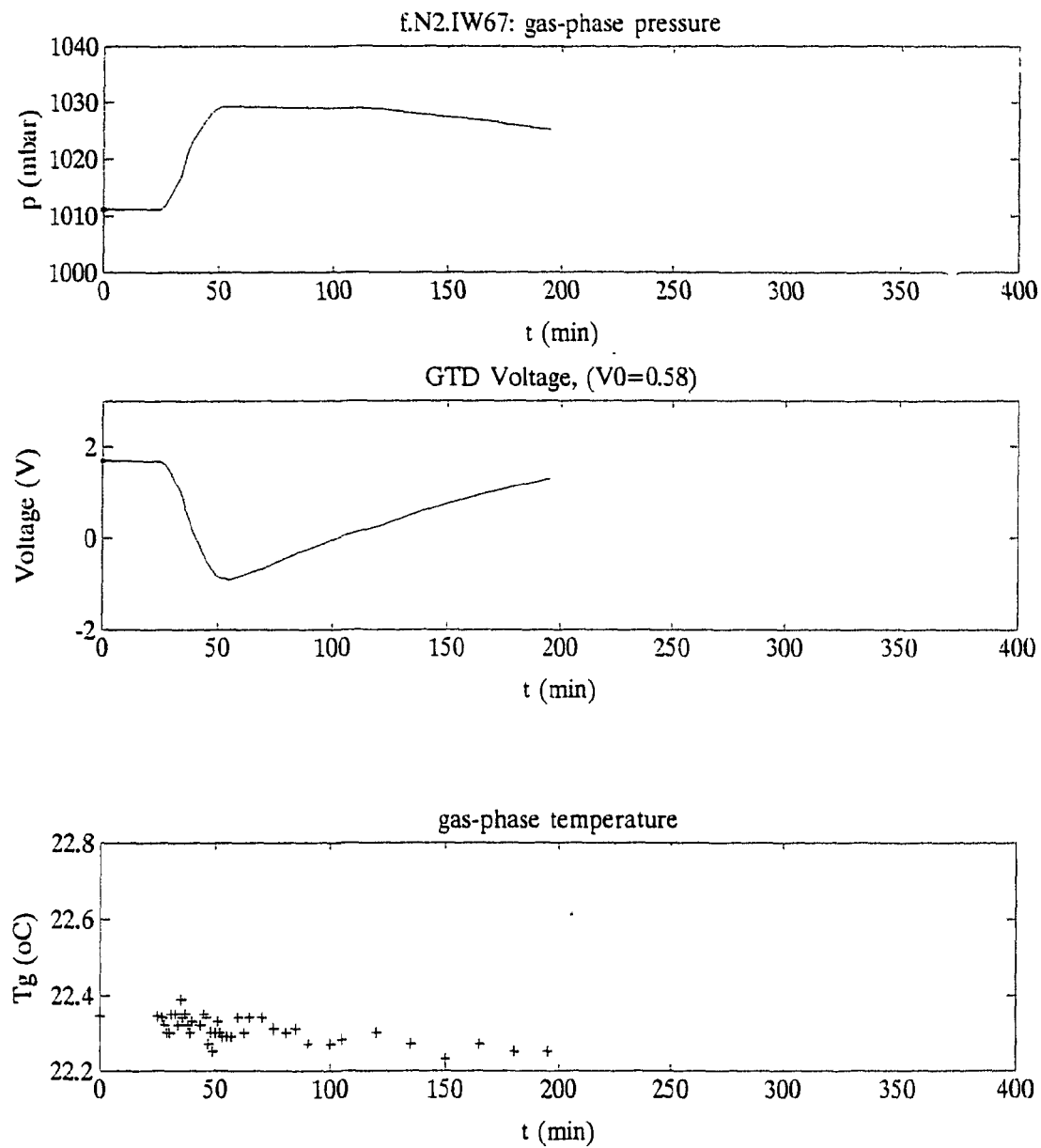
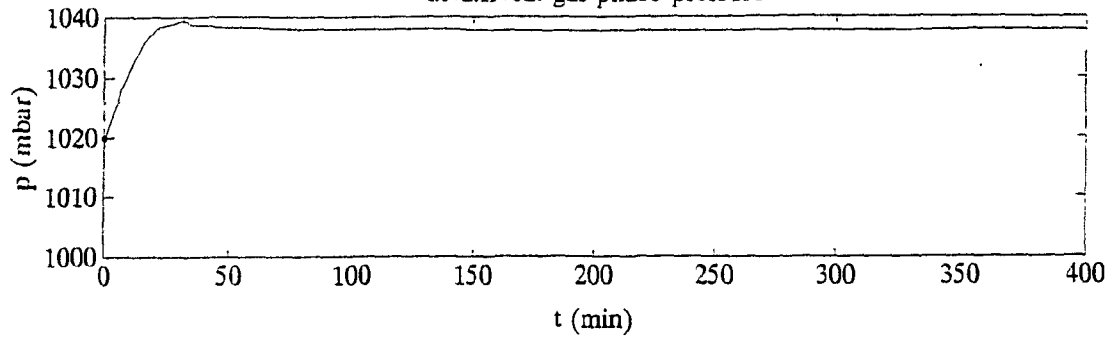
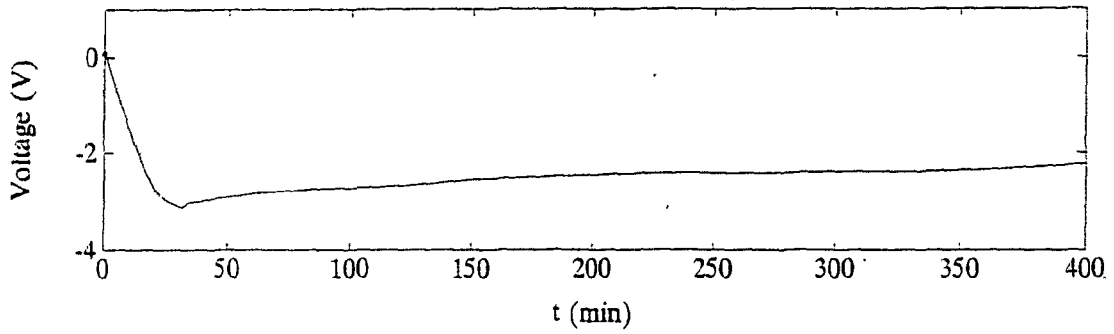
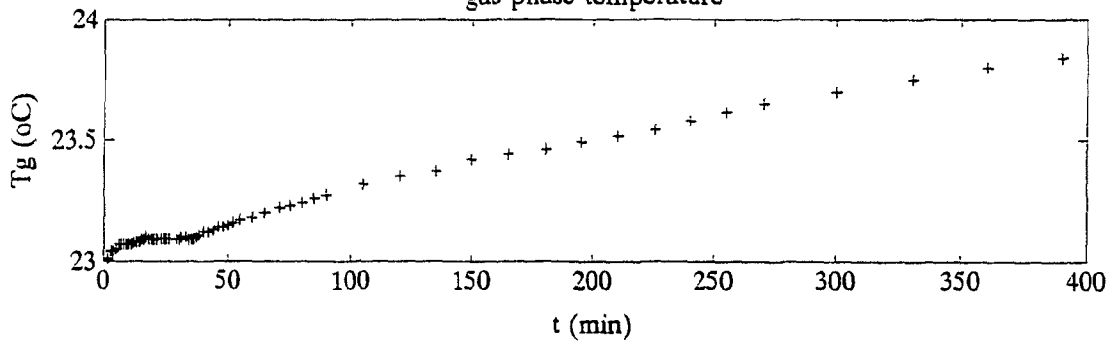


Figure 4.10: N_2 Invasion into fresh water with bubble injection. Time series of (top) gas-phase pressure, raw GTD voltage, and (bottom) gas-phase temperature, T_g .

GTD Voltage, ($V_0=0.46$)

gas-phase temperature



f.N2.IN62: gas tension

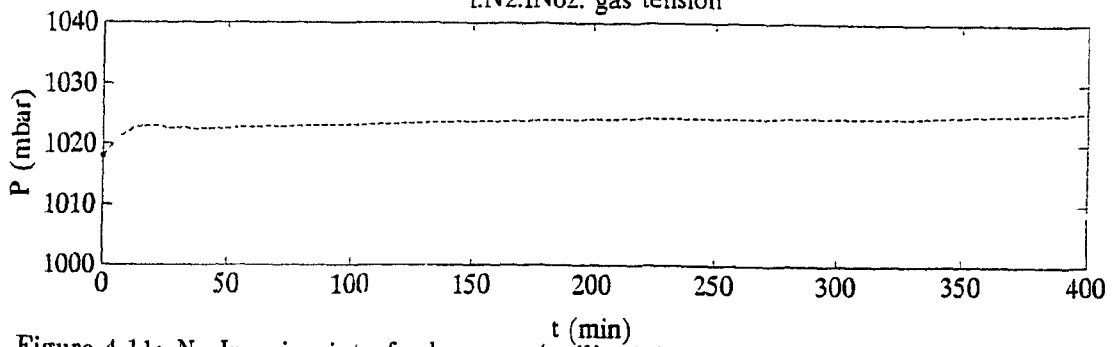


Figure 4.11: N_2 Invasion into fresh water, 'null' mixing conditions. Time series of (top to bottom) gas-phase pressure, raw GTD voltage, gas-phase temperature, T_g , and gas tension, P .

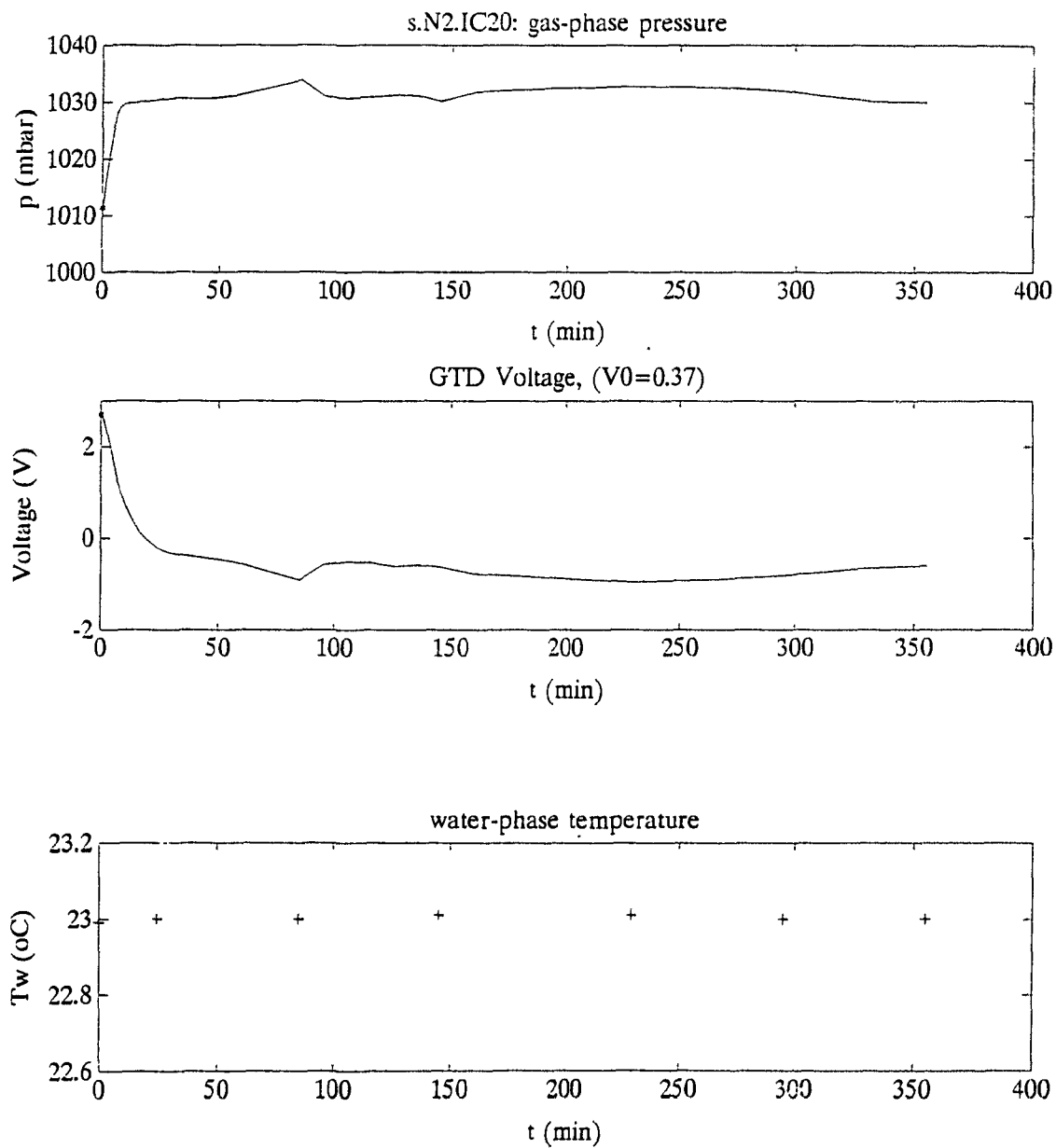


Figure 4.12: N_2 Invasion into sea water under 'circulation' mixing conditions. Time series of (top) gas-phase pressure, GTD voltage, and (bottom) gas-phase temperature, T_g .

example, it was likely that a large gas tension built up as He invaded the water much more rapidly than the previous gas, N₂, evaded. Hydrostatic effects are investigated in further detail in section 4.6. However, poor response in the immediately previous experiments (N₂ under ‘circulating’ mixing conditions) may indicate that the problem started earlier than when the change to He was made. These cases have been omitted from further study.

4.5 V_0 Measurement

As mentioned in section 4.2.1, the voltage at zero differential pressure, V_0 , can be measured during GTD operation by opening the pressure gate. Retracting the motorized pin exposes both ports of the sensor to the same pressure, p . When the gate is again closed the sensing volume re-equilibrates with the gas tension of the surrounding water, including any adjustment arising from membrane flexure. Series of V_0 measurements serve as an indicator of sensor drift and the time constant for re-equilibration is a determination of instrument response time. The voltage response during a V_0 measurement is illustrated in Figure 4.13.

The value of V_0 ranged between 0.51 V and 0.59 V in measurements made between experiments, every 2 to 3 days, over the 30 day duration of the series of freshwater experiments and between 0.31 V and 0.43 V over the 60 day duration of the seawater experiments (Table 4.3). Outlying values generally indicated problems and consequently the sensor would be inspected and the membrane and seals checked. Variations in V_0 between one reading and the next were generally less than 0.02 V and therefore do not contribute any significant error to the calculation of dP/dt . Any uncertainty in the accuracy of V_0 would translate into uncertainty in the value of s^0 but not in the value of the exchange velocity.

The time constants in Tables 4.3 and 4.4 are converted to t_{90} values, the time for 90% recovery, by multiplying by 2.3. All of the values are much larger than theoretical t_{90} 's (section 4.2.4) by factors of order 10 to 40. The measured values are fastest for He and slowest for N₂ in agreement with the theoretical values. This result suggests that indeed the transfer time across the water boundary layer, τ_w , largely determines the response time of the instrument rather than transfer across the membrane material. The estimate for the size of the sensing volume is a likely source of error in the theoretical calculation, both because it is difficult to measure and because it is unknown to what extent it varies depending on hydrostatic pressure conditions. The instrument response time will likely be improved by

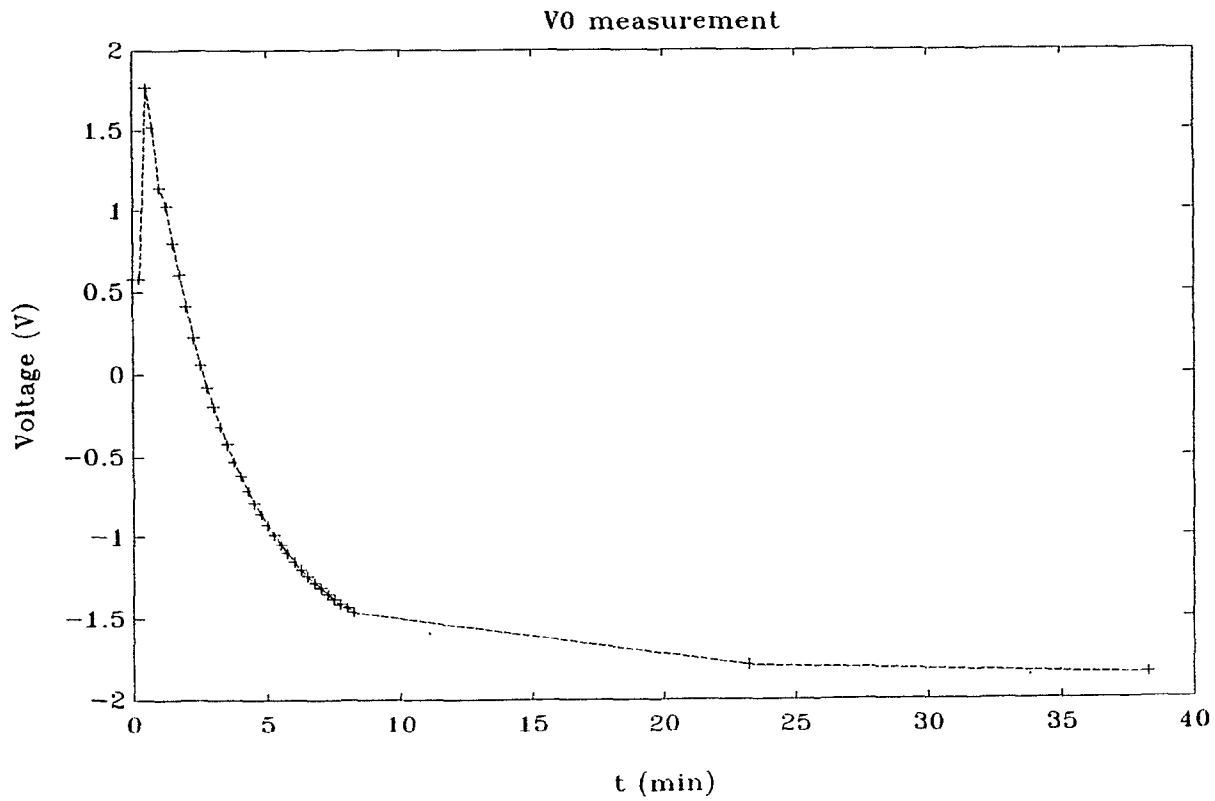


Figure 4.13: Voltage response after a V_0 measurement ($V_0 = 0.58$ V). Reequilibration of the sensing volume with gas tension in the surrounding water follows closing of the pressure gate at time zero. The time constant is calculated as the time required for the the voltage to fall to $1/e$ of the difference between its maximum and final values.

Gas	V_0 (V)	τ (min)
Ar	0.58	3.5
Ar	0.33	5.5
N ₂	0.36	7.5±1
N ₂	0.36	8.7±1
N ₂	0.37	6.2±.3
He	0.58	3.3
He	0.31	1.8
He	0.31	0.5
He	0.31	0.8
CO ₂	0.43	3.8
CO ₂	0.33	2.7

Table 4.3: A sample of V_0 measurements. The value of V_0 ranged between 0.51 V and 0.59 V over the series of freshwater experiments and between 0.31 V and 0.43 V over the series of seawater experiments. Variations between one reading and the next were generally less than 0.02 V. The time constant for the recovery of the signal after a V_0 measurement is τ .

Gas	$\bar{\tau}$ (s)	t_{90} (s)
Ar	270	620
N ₂	450	1040
He	78	180
CO ₂	198	460

Table 4.4: Recovery time constants. The tabulated recovery time constants are the average values from Table 4.3.

working in greater water depths and by any reductions that can be made in the sensing volume. The response times measured after the V_0 measurements are, at most, about 8% of the time constants estimated for the gas-exchange experiments, and usually significantly better (2–5%).

4.6 The Hydrostatic Effect

The response of the GTD to changes in hydrostatic pressure is now examined in more detail. The response arises because the instrument's membrane is not perfectly immobilized, despite efforts taken in the design and construction. As a consequence, hydrostatic pressure changes arising from both changes in gas-phase pressure and water depth can cause the membrane to deform. This causes an interference with the gas tension signal. The effect is of particular concern for a field instrument where large and relatively rapid hydrostatic pressures changes arise due to waves.

The construction of the GTD is important in the context of the hydrostatic pressure response. The silicone rubber membrane material is thin and elastic and is firmly stretched over a silver filter against a smooth and rigid pvc disk. When the GTD is introduced under water, hydrostatic pressure pushes the membrane up against its support, compressing the gas behind it. Gas passes through the membrane and into the water until pressure is equalized on both sides of the membrane. Minimizing the gas sensing volume makes the transition back to isostatic equilibrium rapid.

While the time constant for recovery from a hydrostatic pressure change is considered to be included in the V_0 recovery measurement, the magnitude of the response to hydrostatic pressure changes is still unknown. If the GTD simply behaved as a perfect pressure sensor, its response to hydrostatic pressure changes would be one-to-one. However the signal is damped some extent. A number of observations give estimates of the degree, f , to which the GTD responds to hydrostatic pressure changes. Figure 4.14 shows a voltage response to smoothly decreasing water depth of 0.143 V cm^{-1} corresponding to $f = 0.67$. The instrument response to deformation of the membrane by hydrostatic pressures is felt instantaneously and it is only any resulting transfer of gas across the membrane, negligibly small increments in in this case, for which there is some delay. There is a suggestion, especially from similar filling data, that dV/dx decreases with increasing water depth, and

this result is consistent with the membrane becoming resistant to further deformation. In another exercise, f equal to 0.28 was measured when supersaturated water was decreased in depth in 1 cm increments.

Variability in f has been shown to depend both on the water depth and the state of gaseous equilibration of the system. It is concluded that the membrane is hydrostatically supported, i.e. shows little tendency to deform with further increases in hydrostatic pressure, when the total hydrostatic pressure, $p + \rho g d$, is large in comparison with the gas tension, P . This condition is equivalent to the water depth, in millibar equivalents, being large in comparison to $P - p$. Hydrostatic support of the membrane may also be reduced by the Bernoulli effect. Gradients in water velocities, such as those caused by the stirrer, cause a pressure gradient that tends to pull the membrane away from its support. The pressure difference between the edge of the membrane (where the fluid velocity is estimated at 1 m s^{-1}) and the center of the membrane is calculated to be of order 5 mbar. In the gas exchange experiments $P - p$ values become comparable at times to the head provided by the 30 cm depth of water less a Bernoulli pressure.

In a typical gas exchange experiment where 20-mbar gas-phase pressure changes are applied, the GTD response to the hydrostatic change is estimated at between 5 to 13 mbar. The t_{90} recovery time is a maximum for N_2 of about 17 min (Table 4.4). In the data analyses of Chapter 6 the first 15 to 20 minutes of data after the application of the step gas-phase pressure change are discarded, largely so that functions need not be fitted to inflexion points in the data, but also so that the hydrostatic pressure contribution to the signal will be small. Not only will the hydrostatic signal be less than 10% of its initial value after 17 minutes, but more importantly for the analysis, dV/dt due to hydrostatic changes will be a very small error term. Obviously difficulties arise when p varies during an experiment in any large or rapid manner and this was a basis for not including an experiment in further analysis.

Surface waves have a higher frequency than the signals of interest, unless gas tension response to individual breaking wave events is desired. High frequency response would be filtered out of field measurements. The magnitude of the hydrostatic pressure signals will be smaller the deeper the instrument is deployed and are expected to be negligible below the larger of 1 m or one wave height if supersaturations do not exceed 10%.

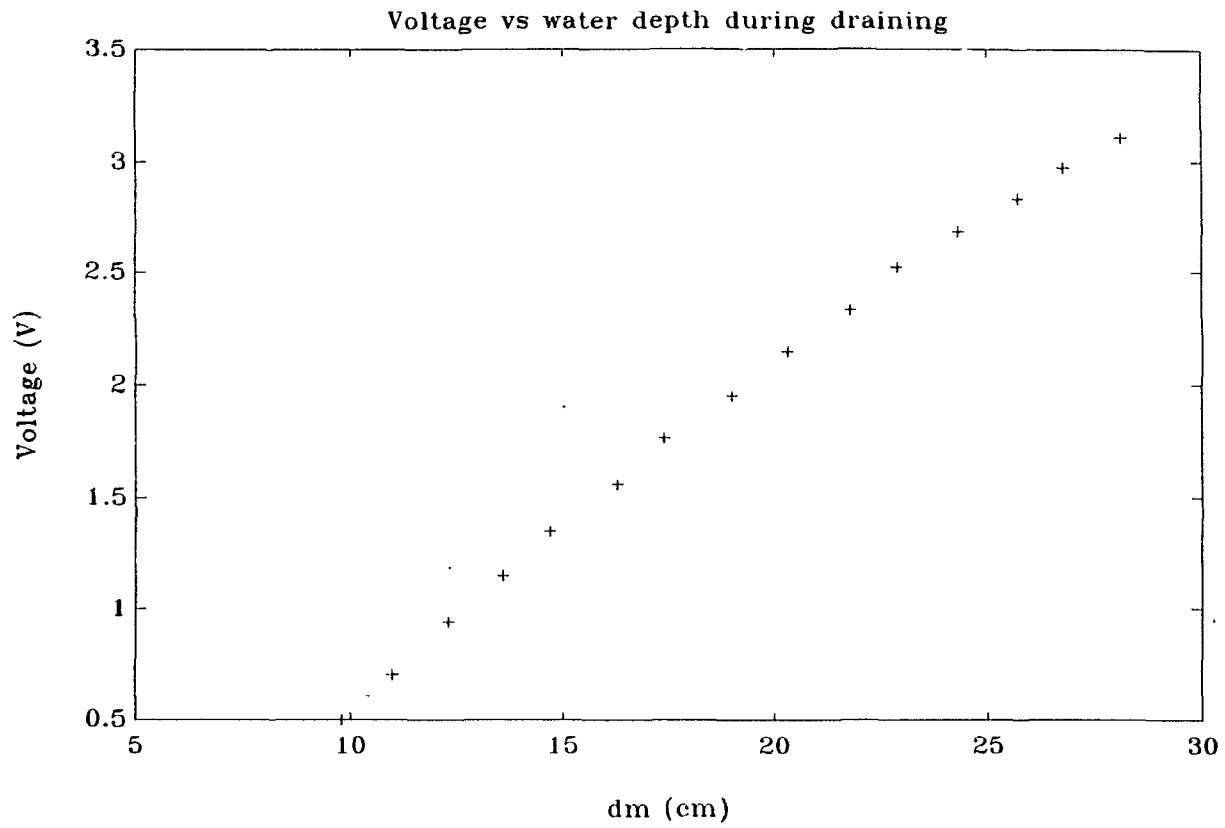


Figure 4.14: Record of GTD voltage output versus water depth during draining of the water in the experimental tank.

4.7 Summary

A gas tension device, GTD, has been described and its performance demonstrated in the laboratory. The GTD provides continuous measurement of total dissolved gas pressure relative to overlying gas pressure and introduces a new method to the study of gas transfer across air-water interfaces. The features of the GTD include:

- a sensitivity of ± 0.01 V equivalent to ± 0.05 mbar gas pressure difference
- a continuous time series output of differential gas pressure
- no gas specificity
- small and correspondingly easy to use in the field
- inexpensive

Because the GTD does not rely on determination of a chemical property, it can be used in experiments with gases covering a wide range of solubilities and diffusivities, as demonstrated by the results of experiments reported in this chapter.

The GTD measurement is sensitive to at least ± 0.05 mbar, but relatively poor measurement of gas-phase pressure will contribute uncertainty to subsequently calculated gas tension. In the experiments reported here, p was measured with a precision of ± 0.1 mbar, and this uncertainty is reflected in the determination of P .

The hydrostatic response of the GTD has been investigated. It has been shown that hydrostatic effects can become important when gas tension becomes comparable to the total hydrostatic pressure in a system.

The response time of the instrument may introduce an offset between the compared variables p and P , but this will be unimportant in field gas-exchange studies where conditions change over periods of hours compared with an instrument response time on the order of a few minutes. By simply improving gas-phase pressure measurement and removing manual data handling, uncertainties in the method might be improved to better than 1%.

Chapter 5

Depth-dependent Gas Flux Model

5.1 Introduction

In this chapter a simple model of gas exchange is developed that includes the role of bubbles as mediators of gas transfer. The model is developed in terms of gas pressure driving forces for gas exchange, incorporating dissolved gas pressure (gas tension). The motivation for the development of this model is as a tool for interpreting the gas exchange data preliminarily described in Chapter 4.

Thorpe (1982) and Merlivat and Mémery (1983) pioneered models of the contribution of bubbles to gas exchange in the ocean. Thorpe's model combines his own field observations of bubble depth distributions as a function of wind speed with empirical mass flux results (Thorpe, 1982; Thorpe, 1984). More recently Smith and Jones (1985) and Woolf and Thorpe (1991) have suggested that air-sea gas transfer should be represented by a flux equation of the form,

$$F = -k(c_a + \delta c - c_w). \quad (5.1)$$

where the extra term, δc , is the steady-state supersaturation of gas resulting from the balance of free-surface and bubble-mediated fluxes. It is clear that when $c_a = c_w$ there remains a flux, driven by δc . It may also be considered that the driving force for gas invasion is increased by the amount δc due to bubble-supported supersaturation. Smith and Jones consider δc to be the result of a 'pumping' pressure — a combination of hydrostatic, Laplace and hydrodynamic pressures on injected bubbles. Woolf and Thorpe describe δc ($c_a \Delta_e$ in

their notation) as a function of wind speed (*Woolf and Thorpe, 1991*).

Similar to Thorpe (1982) and Woolf and Thorpe (1991), depth dependencies of the bubble flux are given primary consideration in the development of the present model. However, more emphasis is placed on relating the bubble flux directly to observable properties of the bubble population. The final form of the flux equation in my model is similar to equation 5.1 and the two will be compared in the discussion section of this chapter. It is hoped that the contribution of bubbles to total gas fluxes might be simply defined by a bulk description of the bubble population, even though a variety of factors are newly recognized as affecting bubble populations (*Thorpe et al., 1992*). If the role of bubbles may be accounted for separately from the surface gas flux, it may then be possible to develop a separate predictive relationship for the bubble-mediated gas flux. This bubble flux might then be simply 'added' to the surface flux, for which the behaviour of the exchange velocity is relatively well known. Consequently a two component approach to the modelling of air-water gas transfer is developed here. It is an extension of a simple model described previously (*Anderson and Johnson, 1992*).

The first component is the direct flux across the sea surface. This flux shall be referred to as an equilibrium flux because it drives the system toward a steady state where gas pressures are equal in both phases, i.e. at equilibrium. The second component is the contribution to the total gas flux of gas transfer between injected bubbles and their surrounding water. A significant characteristic of the bubble flux is that it tends to drive the system toward a state of supersaturation, i.e. steady state is not an equilibrium condition in the usual sense. Gas transfer via bubbles may also be large and rapid under certain circumstances. The accounting of the equilibrium and bubble fluxes is facilitated because now a new measurement of gas tension may be incorporated into the model. The instantaneous gas tension measurement, when combined with a measurement of gas-phase pressure, is an instantaneous measure of the state of the system with respect to gaseous equilibrium between phases.

For the benefit of gaining possible further insight into the gas exchange process, the consequence of a depth-dependent term in the formulation of the bubble flux is also investigated in this chapter.

5.2 Model Development

5.2.1 Equilibrium flux

The equilibrium component of the gas flux (per unit sea surface area) is the usual formulation based on Fick's first law,

$$F_e = -k \frac{1}{H} (P - p), \quad (5.2)$$

where k is the exchange velocity across the sea surface, P is gas tension, and p is gas-phase pressure. Henry's law constant, H , describes the gas-phase pressure that would be in gaseous equilibrium with the gas concentration in water (units of pressure per unit concentration). Figure 5.1 illustrates the notation and the chosen convention that the flux is positive for gas transfer from the gas phase to the water phase. Notation throughout the literature is unfortunately inconsistent. Notation similar to Woolf and Thorpe's (1991) is used as much as possible. The $1/H$ factor is preferred to an alternative substitution of a solubility coefficient simply because there are so many definitions of solubility. The bulk fluids are assumed to be well mixed so that the gas pressures are uniform throughout.

5.2.2 Individual bubble flux

The form of the expression for the bubble flux is developed by first considering the gas flux across the surface of an individual bubble into the surrounding water. Similar to the equilibrium flux, the individual bubble flux is expressed in terms of an exchange velocity multiplied by a factor for the driving force for gas exchange across a bubble surface. The contribution of a single stationary bubble of radius r at depth z to the volume gas flux is expressed as,

$$q_b(z) = -4\pi r^2 j \frac{1}{H} (P - p_b) \quad (5.3)$$

i.e., the bubble surface area times the individual bubble transfer velocity, j , multiplied by a driving force for gas transfer. The driving force for bubble dissolution or growth is the difference between gas tension in the surrounding water, P , and the gas pressure inside the bubble, p_b . Internal pressure, p_b , is made up of three terms,

$$p_b = p + \rho g z + \frac{2\sigma}{r}. \quad (5.4)$$

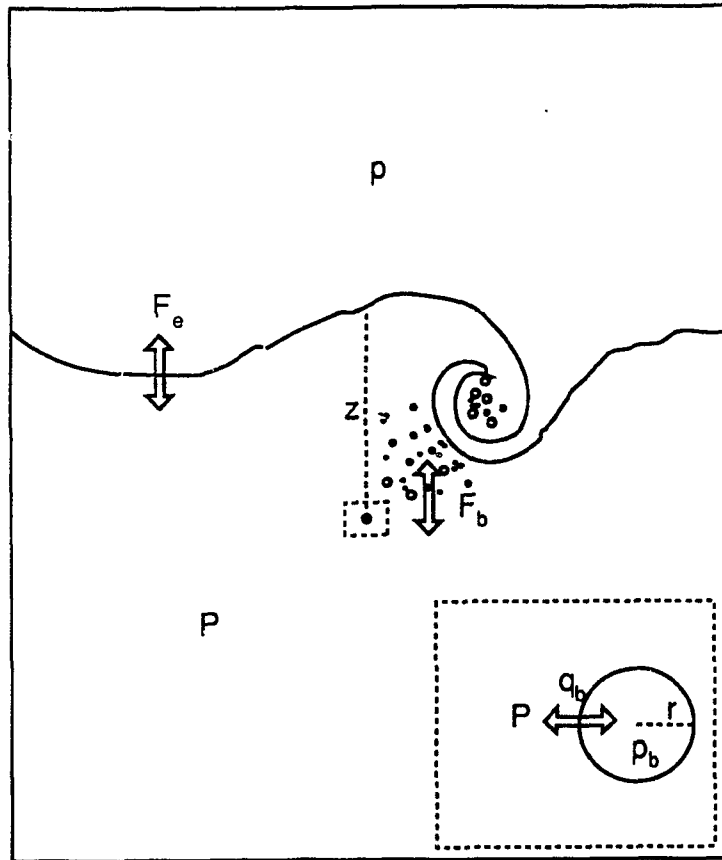


Figure 5.1: Gas flux model notation: F_e , air-to-sea flux across the sea surface, and $q_b(z)$, flux across the surface of an individual bubble. A positive flux into the water is the chosen convention.

The first term is the gas pressure provided by the sum of the partial pressures of the component gases in an unconstrained volume, equal to atmospheric pressure. The second term is the hydrostatic pressure, ρgz , due to the overlying water. Hydrostatic pressure increases at the rate of approximately one millibar per centimetre increase in depth. The third term in 5.4 is the Laplace pressure arising due to the surface tension at the air-water interface. The magnitude of the Laplace term depends on the ratio of surface tension to radius and is highest for small bubbles with clean interfaces. Bubbles rapidly accumulate surface-active materials in natural waters and a surface tension value, σ , of $3.6 \times 10^{-2} \text{ N m}^{-1}$, about half the value for clean bubbles, may be appropriate (*Thorpe, 1982*). Laplace pressure is negligible for large bubbles, but for a $100 \mu\text{m}$ diameter bubble the value is 1.4 kPa (14 mbar). Although the Laplace pressure is small relative to gas-phase pressure, it may be large relative to the driving force for gas exchange. The Laplace term is always positive and has the effect of forcing bubbles to dissolve with a positive feedback that the smaller the bubble becomes the higher the Laplace pressure. The fact that Laplace and hydrostatic pressure terms always tend to enhance bubble dissolution over bubble growth is one aspect of the asymmetry referred to in bubble-mediated gas exchange (*Atkinson, 1973; Woolf and Thorpe, 1991*).

5.2.3 Depth-dependent bubble (DDB) flux

In the next step the gas flux is integrated over all bubbles at a given depth and expressed in terms of flux per unit sea-surface area so that the term may be combined at a later stage with the similarly expressed equilibrium flux. A definition of $N_b(z, r)$ as the number of bubbles of radius r , at depth z beneath a unit area of sea surface is useful. Then the total bubble flux per unit sea surface area at depth z is the sum over all radii of the product of $N_b(z, r)$ and the individual bubble flux,

$$F_b(z) = \sum_r \dot{N}_b q_b. \quad (5.5)$$

$F_b(z)$ is a function of bubble radius through q_b (equation 5.3), both because j in q_b is a function of r , and because of the surface area factor. The nature of the bubble surface also affects j ; whether the bubble surface is clean or dirty affects the transfer velocity directly and also indirectly by affecting the mobility of the bubble gas-water interface and hence the rise time of the bubble.

It is assumed that evaluation of 5.5 returns an expression of similar form to the expressions for the equilibrium flux and the individual bubble flux, i.e. with an exchange velocity factor multiplied by a driving force for gas exchange. The depth-dependent bubble (DDB) gas flux is

$$F_b(z) = -\frac{k_b(z)}{H}(P - (p + \rho gz)), \quad (5.6)$$

where $k_b(z)$ is a bubble exchange velocity for the entire bubble population at depth z and the driving force for gas exchange is the difference between gas tension and a simplified internal bubble pressure. Looking at $z > 14\text{cm}$, so that $\rho gz > \frac{2\sigma}{r}$ for $r \geq 100\mu\text{m}$, the Laplace pressure term can be dropped. The value of $k_b(z)$ will depend on the number and size distribution of bubbles as well as the total surface area they provide per unit sea surface area – also, therefore, on the bubble volume to surface area ratio. In general, any factors, including gas diffusivity, that might affect the efficiency of gas transfer from a bubble should be considered to be included in k_b . Thus the dynamics of the bubble and the relative proportion of very small bubbles in the population also affect k_b .

In this simple model I start from the premise that the most significant variations in bubble exchange velocity and bubble dissolution driving force occur with depth. A bubble injected deeply has both a large driving force for dissolution and a long rise-out time over which to equilibrate. There is general agreement in the literature that in natural bubble populations the number of bubbles falls off approximately exponentially with depth (Wu, 1981; Thorpe, 1982; Crawford and Farmer, 1987; Wu, 1988; Hwang *et al.*, 1990). The bubble exchange velocity, k_b , is chosen to be represented by an exponentially decaying function over depth,

$$k_b(z) = k_{b0} \exp(-z/z_b). \quad (5.7)$$

This parametrization could be improved upon later, e.g. when improved bubble population measurements become available so that weighting might be applied for the relative numbers of small bubbles. The factors contributing to k_b will likely vary differently with depth, and to different degrees depending on the time scales appropriate for the particular conditions. (Jähne *et al.*, 1984b). In this analysis the net result is considered to be an exponential decay of k_b over an e -folding depth, z_b . The e -folding depth of penetration of the bubble population will typically determine z_b . Others have also incorporated an exponential decay

factor into their models based on their photographic (Broecker and Siems, 1984), laser-scattering (Jähne *et al.*, 1984b), and acoustic (Thorpe, 1982) observations of the variations of bubble populations with depth. Few experiments have been carried out to evaluate bubble flux models that include measurement of the bubble population (Jähne *et al.*, 1984b; Siems, 1980; Broecker and Siems, 1984), but it is a field of rapidly growing interest.

5.2.4 Total bubble flux

The depth-averaged bubble exchange velocity over a mixing-layer depth d_m is,

$$\begin{aligned}\langle k_b \rangle &= \frac{1}{d_m} \int_0^{d_m} k_b(z) dz \\ &= c_1 k_{b0},\end{aligned}\tag{5.8}$$

where

$$c_1 = I(1 - \exp(-1/I))\tag{5.9}$$

$$I = \frac{z_b}{d_m}.\tag{5.10}$$

And the ratio I is considered to be the depth 'intensity' of bubble injection. The intermediate steps in the integration are given in Appendix B. The depth-averaged bubble flux per unit area of sea surface is the integral of F_b , equation (5.6), from the surface to the depth of the mixing layer, divided by the mixing-layer depth,

$$\begin{aligned}\langle F_b \rangle &= -\frac{1}{d_m} \int_0^{d_m} k_b \frac{1}{H} (P - (p + \rho g z)) dz \\ &= -\frac{\langle k_b \rangle}{H} (\langle P \rangle - p) + \frac{\langle k_b \rangle}{H} \rho g d_m c_2 / c_1,\end{aligned}\tag{5.11}$$

where (note the symmetry with c_1),

$$c_2 = I(c_1 - \exp(-1/I))\tag{5.12}$$

and the details of the integration are again given in Appendix B. The depth variations in the bubble flux, and consequently in gas tension, have been averaged in this step to match the requirements of the equilibrium flux model that the bulk fluids are well mixed. Consequences of persisting variations in gas tension with depth are investigated in section 5.5. $\langle F_b \rangle$ is now in the same terms as F_e and subsequently the qualifying parentheses are dropped, while their significance remains, namely that the gas pressures and the gas fluxes are average values over the depth of the mixing layer.

5.2.5 Total gas flux

The total gas flux is the sum of the equilibrium and bubble fluxes and may also be equated to the rate of increase of gas in the water volume per unit sea surface area,

$$F = \frac{d_m}{H} \frac{\partial P}{\partial t}. \quad (5.13)$$

Equating 5.13 to the sum of F_e and F_b (5.2 and 5.11) and rearranging gives

$$\begin{aligned} \frac{\partial P}{\partial t} &= -\frac{k}{d_m}(P-p) - \frac{\langle k_b \rangle}{d_m}(P-p) + \frac{\langle k_b \rangle}{d_m} \rho g d_m c_2 / c_1 \\ &= -\frac{k'}{d_m}(P-p) + \langle k_b \rangle \rho g c_2 / c_1 \end{aligned} \quad (5.14)$$

where the combined exchange velocity is k' ,

$$k' = k + \langle k_b \rangle.$$

The combined exchange velocity is comparable to the total exchange velocity measured by other experimenters, but, because of the additional term involving $\langle k_b \rangle$ in (5.14), it cannot be described as the 'total' exchange velocity here.

Integration of $\partial P / \partial t$ (equation 5.14) over time when p is constant (details in Appendix B) gives an expression for the average gas tension over the mixing-layer depth as a function of time,

$$P(t) = \left(p + \rho g d_m \frac{\langle k_b \rangle c_2}{k' c_1} \right) (1 - e^{-\frac{k'}{d_m} t}) + P_0 e^{-\frac{k'}{d_m} t}. \quad (5.15)$$

5.3 Discussion

5.3.1 Analysis of the total gas flux equation

Converting $\partial P / \partial t$, equation 5.14, to a downward flux in concentration terms by multiplying by d_m / H gives an expression,

$$F = -k'(c_u - c_a) + \frac{\langle k_b \rangle c_2}{H c_1} \rho g d_m \quad (5.16)$$

that can be compared with that of Woolf and Thorpe (equation 5.1). There is a sign difference between the expressions owing to different conventions selected for the direction of a positive flux. When $c_a = c_w$, Woolf and Thorpe's expression for the flux becomes

$$F = -k c_n \Delta c, \quad (5.17)$$

Feature	Driving force	Rate
deep injection	+	
large area/volume		+
large $2\sigma/r$	+	
long rise time		+

Table 5.1: Bubble population features and their qualitative effect on gas transfer.

i.e. the additional flux driving the system to supersaturation is a function of the total exchange velocity and some unknown supersaturating factor that increases the concentration above c_a . The equivalent situation in my flux equation gives

$$F = \frac{\langle k_b \rangle c_2}{H c_1} \rho g d_m. \quad (5.18)$$

where the additional flux driving the system to supersaturation is a function of the bubble exchange velocity, solubility (via H), and properties of the bubble population itself (through c_2/c_1). This new formulation makes the distinction that the *bubble* exchange velocity is the relevant factor for the supersaturating flux component. The supersaturations that can result via bubbles are a function both of the solubility of the gas and of the efficiency of the bubble population in transporting the gas. Because a single gas situation is appropriate for the gas exchange experiments in the laboratory, the ‘concentration’ of the gas in the atmosphere is not an explicit factor. The contribution of bubbles to the exchange velocity is explicitly determined in this new formulation. A ‘total’ exchange velocity in my equation 5.16 is an ambiguous reference, due to the appearance of more than one term containing an exchange velocity. Consequently I refer to k' as the combined exchange velocity and point out that use of k' alone will underestimate the ‘total exchange velocity’ and the total gas flux because an additional term explicitly containing the bubble exchange velocity is required.

5.3.2 Bubble population effects

For the same total volume of injected gas, a bubble population that has proportionately more small bubbles than large bubbles has several features that can be considered to enhance either the driving force or the rate (exchange velocity) of gas exchange. These features are outlined in Table 5.1.

Small bubbles, having relatively small buoyancy forces to counteract the downward momentum imparted by falling water, reach depths where they will be subject to relatively higher hydrostatic pressures. The smallest bubbles, especially those of diameter $100\ \mu\text{m}$ or less, in addition are susceptible to collapse due to Laplace pressure. Both deep injection and Laplace pressure work to increase the potential supersaturation and hence driving force for the bubble gas flux. The Laplace pressure term has been neglected, as being small for bubbles larger than about $100\ \mu\text{m}$ that are injected to deeper than 14cm . Depending on the relative concentration and importance of small diameter bubbles, presently poorly known in any natural bubble population, this may or may not be an important omission. While dynamical arguments suggest that small bubbles are relatively more efficient gas exchangers than large bubbles, it is unclear just what segment of the small bubble population contributes the most. Impedence of gas transfer by natural surfactant coatings is an increasingly important consideration for bubbles with small surface areas, perhaps offsetting their higher impetus for dissolution, e.g. (*Johnson and Wangersky, 1937*).

The features of a population of small bubbles that may increase the bubble exchange velocity include a high surface area to volume ratio and relatively long rise-out times. These features increase the efficiency of each bubble, and therefore each plume, by allowing more time to equilibrate with the surrounding water.

A complicating factor, suggested by Woolf and Thorpe (1991), is a possible feedback from the degree of saturation of the water on the bubble population and hence on rates of bubble dissolution, i.e. a feedback between driving force and exchange velocity. As an extreme example, consider bubbles injected into completely degassed water: the large driving force for dissolution will dissolve a large fraction of each bubble and significantly alter each bubble's buoyancy and hence rise-out time. As described above, the extended rise-out time then translates into a relatively higher bubble exchange velocity. This feedback would cause a changing efficiency of gas transfer via bubbles with time. Since k_b is a large component of k' in this case, a changing $\langle k_b \rangle$ would be apparent as a departure from a straight line of dP/dt versus $P - p$ in gas-tension exchange experiments. As indicated by Woolf and Thorpe (1991), the feedback mechanism requires special consideration when the dissolving bubbles contain a gas mixture because then a co-dependence of exchange rates of one gas on another may exist.

A change in bubble dissolution rates has been observed in the laboratory (*Schulze and Schlürder, 1985*) and treated theoretically (*Davies, 1986*) as being the consequence of the changing mobility of the bubble surface due to collection of surface active materials. The effect has been shown to be significant for soluble gases resulting in exchange velocity enhancements by a factor of 3 for periods of several seconds.

5.3.3 Bubble size and dynamics

To assume that the gaseous content of a bubble is constant over its lifetime is an oversimplification. Bubble contents change both in total amount and in composition: bubbles dissolve or grow as a result of gas exchange, and different gases exchange at different rates (*Woolf and Thorpe, 1991*). Even if gases exchange at the same rate there are other effects that may control the efficiency of transfer of the bubble population as a whole. For a given bubble injection rate, the more bubbles that equilibrate before they rise out, the higher is the gas transfer efficiency. Large bubbles have high buoyancies and consequently spend less time in the water column than small bubbles, because they are not injected as deeply and do not take as long to rise out. Therefore populations of large bubbles will have lower bubble exchange velocities than populations of small bubbles, even when the individual bubble exchange velocity, j , is the same in each case.

Woolf and Thorpe (1991) compared theoretical equilibration times and rise times as a function of bubble size (illustrated in their Figure 3) for single-gas bubbles. Their calculated equilibration times are under the simplified conditions of constant pressure and constant radius. The difference in behaviour between CO₂ and the other less soluble gases is marked: over the time it takes bubbles to rise 10 cm, bubbles of CO₂ up to a radius of about 380 μm fully equilibrate, while only those bubbles up to a radius of about 90 μm equilibrate with any of the other gases. Over a rise distance of 100 cm still only those bubbles up to about 200 μm equilibrate with the less soluble gases. Woolf and Thorpe suggest that the transfer of the more soluble gas is less sensitive to changes in the bubble population. The experimental results of Broecker and Siems (1984) also appear to support this suggestion. As bubble populations increased with increasing wind speed the exchange velocity of O₂ increased more rapidly than the exchange velocity for more soluble CO₂. The number of bubbles less than about 200 μm are considered to be particularly important for gas exchange

(*Woolf and Thorpe, 1991*).

Bubble dynamics are complex, especially for bubbles containing gas mixtures, and become more so under field conditions when large scale turbulence, Langmuir circulations, and organic films are influences.

5.3.4 Anti-bubble Bias

Having described in this chapter some of the properties of bubbles and a couple of models for bubble-mediated gas exchange, some further points can now be made concerning the way studies involving bubble-mediated gas transfer have been carried out. Almost invariably gas exchange studies are conducted in only one direction — as evasion experiments. Typically a tracer is introduced to the water and its subsequent disappearance from the water, or, less frequently, appearance in the overlying gas space is monitored. Budgeting of gas losses besides escape to the gas phase is frequently a problem, especially in field exercises, and is one reason why invasion experiments are avoided. This one-sided view of gas exchange biases against a full appreciation of the bubble flux mechanism.

As mentioned, tracer gas exchange studies typically involve adding a source of tracer to the water and flushing the gas phase to keep it tracer-free so that the concentration difference between the phases is initially large and always well known (if precise measurements of the dissolved gas are made). The rate of disappearance of tracer from the water, when divided by the concentration difference, is linearly related to the exchange velocity (e.g. equation 5.2). However, a tracer-free atmosphere is not representative of the situation of interest in the ocean. Both the rate of uptake and the degree of uptake, or final state of saturation, are important questions. A tracer-free atmosphere will not support tracer supersaturation in the water when bubble injection is an active process. Whereas, in the case where the atmosphere contains tracer, bubble injection can increase the capacity of the water to take up tracer.

In cases where the overlying atmosphere is not maintained tracer-free, or is erroneously assumed to be tracer-free, there are important consequences. Specifically, if bubble injection is sufficient to support a steady-state supersaturation, then the driving force for gas evasion is reduced by exactly the amount of supersaturation that is supported at steady state. When the exchange velocity is calculated by the typical methods, the exchange velocity will

be *underestimated* in evasion experiments where the driving force is uncorrected for a non-zero tracer concentration *and* the degree of supersaturation that is consequently supported. The degree of the underestimation is equal to the degree of steady-state supersaturation when the surface flux balances the bubble flux, both in percent. The model of Woolf and Thorpe (1991) addresses this concern, using the factor Δ_e for the fractional supersaturation that is supported at steady state. My formulation also addresses the difficulty, because the combined exchange velocity, which is determined from the ‘uncorrected’ driving force is not the total exchange velocity — there is an additional bubble exchange velocity.

It is interesting to speculate how other results reported in the literature might be reinterpreted. If, for example, a higher supersaturation is supported by the less soluble gas (for a given wind speed and bubble population) an appropriate correction to the driving force would decrease the calculated net exchange velocity for the less soluble gas relative to the more soluble gas. The reported divergence in exchange velocity with windspeed due to gas solubility might then disappear.

These examples of how bubble-mediated gas exchange can be both underestimated and overlooked make further careful studies of the process imperative. The gas tension method offers sensitive measurement of the instantaneous difference in gas pressures between phases — an invaluable measurement for evaluating the role of bubbles in gas exchange.

5.4 A Tool for Gas-Exchange Analysis

The main results of the above model formulation are expressions for the rate of change of gas tension, $\partial P/\partial t$ and $P(t)$ (equations 5.14 and 5.15), with a distinct parametrization for the contribution of bubbles. Equation 5.14 shows that experimentally determined values of $\partial P/\partial t$ and $P - p$ should give a linear relationship where the slope yields the combined exchange velocity divided by the water volume to surface area ratio. The value of the intercept represents the positive constant that drives P beyond an equilibrium value and towards supersaturation. By selecting a value for the e -folding depth of penetration of the bubble population relative to the mixing layer depth, d_m , the constant c_2 can be determined. Subsequently, from the intercept and c_2 , the value for k_{b0} , the bubble exchange velocity at the surface, can be determined. The combined exchange velocity, k' , can then be separated into components k and k_b .

In practice, to avoid noisy derivatives and evenly weight the data, a method that determines a best fit to the observed values of $P(t)$ is used. To get an expression for $P(t)$ when p is not constant, a cubic expression is fit to the observed values of p_{obs} beginning where p changes are smaller than 0.1 mbar per minute,

$$p = ht^3 + lt^2 + mt + n. \quad (5.19)$$

Then $\partial P/\partial t$ (equation 5.14) can be integrated (details in appendix C) to give

$$\begin{aligned} P_{calc} = & \left(p - \frac{d_m}{k'} \frac{\partial p}{\partial t} + \left(\frac{d_m}{k'} \right)^2 \frac{\partial^2 p}{\partial t^2} - \left(\frac{d_m}{k'} \right)^3 \frac{\partial^3 p}{\partial t^3} + \rho g d_m \frac{\langle k_b \rangle c_2}{k' c_1} \right) \\ & - \left(p(0) - \frac{d_m}{k'} \frac{\partial p(0)}{\partial t} + \left(\frac{d_m}{k'} \right)^2 \frac{\partial^2 p(0)}{\partial t^2} - \left(\frac{d_m}{k'} \right)^3 \frac{\partial^3 p(0)}{\partial t^3} \right. \\ & \left. + \rho g d_m \frac{\langle k_b \rangle c_2}{k' c_1} \right) e^{-\frac{k'}{d_m} t} + P_0 e^{-\frac{k'}{d_m} t}. \end{aligned} \quad (5.20)$$

i.e. $P_{calc} = f(a, b, p, t)$ where

$$a = k'/d_m \quad (5.21)$$

$$b = \rho g \langle k_b \rangle c_2 / c_1. \quad (5.22)$$

And it can be seen that a corresponds to the 'slope' and b to the 'intercept' of the dP/dt versus $P - p$ method. By iteration and inspection values of a and b that provide the best fit of P_{calc} to observed $P(t)$ are obtained. Further details of the analysis method are given in Chapter 6.

Comparison of the calculated values of k for the different gases to $k \propto D^{1/2}$ predictions for 'rough' surface conditions provides a check on the model, if only in a relative sense.

The relative importance of diffusivity, solubility and bubble populations on k_t can then be investigated. The following section will show how the degree of saturation at steady state also provides an indication of the relative importance of the factors solubility, diffusivity, and bubble population on gas flux.

5.5 Steady-state Supersaturations

From examination of $P(t)$, (5.15), at long times it follows that gas tension approaches a steady-state value of $p + \rho g d_m \frac{\langle k_b \rangle c_2}{k' c_1}$. Equivalently the steady-state gas tension can be

evaluated from the value of P which satisfies $F_e + F_b = 0$. The time constant for the gas transfer is d_m/k' . The steady-state saturation anomaly, s^0 , defined as the excess gas tension over gas-phase pressure at steady state, is next examined at its limits.

$$s^0 = (\rho g d_m c_2 / c_1) \frac{\langle k_b \rangle}{k'}. \quad (5.23)$$

The value of s^0 is calculated from experimental data from b/a .

As defined previously, c_1 (5.9) and c_2 (5.12), are functions only of I , the ratio of the e -folding depth of bubble penetration to the mixing-layer depth. The steady-state supersaturation is the product of two components in which the first, $(\rho g d_m c_2 / c_1)$, can be considered a potential supersaturation. The ratio of the bubble exchange velocity to the combined exchange velocity, always less than or equal to one, then determines the extent to which the potential supersaturation is reached. From a consideration of the limits of c_1 and c_2 ,

$$\begin{aligned} \lim_{I \rightarrow \infty} c_1 &= 1 \\ \lim_{I \rightarrow \infty} c_2 &= 0.5 \\ \lim_{I \rightarrow 1} c_1 &= 1 - 1/e \\ \lim_{I \rightarrow 1} c_2 &= 1 - 2/e \\ \lim_{I \rightarrow 0} c_1 &= I \\ \lim_{I \rightarrow 0} c_2 &= I^2, \end{aligned}$$

it follows that

$$\begin{aligned} \lim_{I \rightarrow \infty} s^0 &= 0.50 \rho g d_m \frac{\langle k_b \rangle}{k'} \\ \lim_{I \rightarrow 1} s^0 &= 0.42 \rho g d_m \frac{\langle k_b \rangle}{k'} \\ \lim_{I \rightarrow 0} s^0 &= \rho g z_b \frac{\langle k_b \rangle}{k'}. \end{aligned}$$

The more physically likely limits are $I \rightarrow 0$, for shallow bubble injection, and $I \rightarrow 1$, when bubble injection is strong enough to mix bubbles throughout the mixing layer. If the maximum depth to which bubbles are mixed is equal to d_m then z_b , the e -folding depth of bubble penetration, will be quite similar to $0.42d_m$. The limits converge, even for $I \rightarrow \infty$, and the model is well-behaved. The behaviour of the model is shown (Figure 5.2) in mesh and contour plots of normalized supersaturation as a function of z_b/d_m and $\langle k_b \rangle/k'$.

The supersaturation is normalized relative to $\rho g d_m$. As the above described limits lead one to expect, normalized supersaturation reaches a plateau approximately at values of $z_b/d_m > 0.75$. Significantly, when bubble injection is strong and $\langle k_b \rangle/k'$ therefore tends to one, the supersaturation is dependent only on z_b/d_m . The level of supersaturation becomes independent of the gas exchange velocities and therefore independent of the gas properties.

5.6 Predictions from the DDB Flux Model

5.6.1 Predictions relevant to the bubble-injection experiments

The DDB flux model equations separates the combined gas exchange velocity into components for the surface exchange velocity and the bubble exchange velocity.

From the Schmidt number relationship discussed in Chapter 1, the calculated values of the surface exchange velocities, k , are expected to compare as $D^{1/2}$, i.e. fastest for He and equal for the other gases. All k 's are expected to be smaller in sea water compared with fresh water, due to the lower gas diffusivities in seawater and the higher viscosity of seawater. These results are expected assuming that surface gas exchange doesn't evolve a different Sc relationship due to the presence of bubbles.

The bubble populations measured in the seawater plume compared with the freshwater plume, when considered in light of the discussion on the dynamics of bubbles due to gas uptake, allow some predictions to be made regarding the relative magnitudes of the bubble exchange velocities expected in the gas-exchange experiments. The large numbers of small bubbles in the seawater plume are expected to be efficient gas exchangers. Higher k_b 's are expected in sea water compared with fresh water, despite the factors working to the opposite effect (diffusivity and viscosity) on the gas exchange velocities for individual bubbles (j). In particular, the highest k_b is expected under the most efficient conditions of high gas diffusivity, low gas solubility, and large numbers of small bubbles, i.e. He in sea water. In contrast, when conditions are more inefficient, in particular due to low numbers of small bubbles and low gas diffusivity, lower k_b 's are expected. Solubility is not expected to influence efficiency to the same degree in fresh water, where there are more large bubbles, as it might in sea water.

Interestingly, the analysis of the steady-state supersaturation suggests when bubble

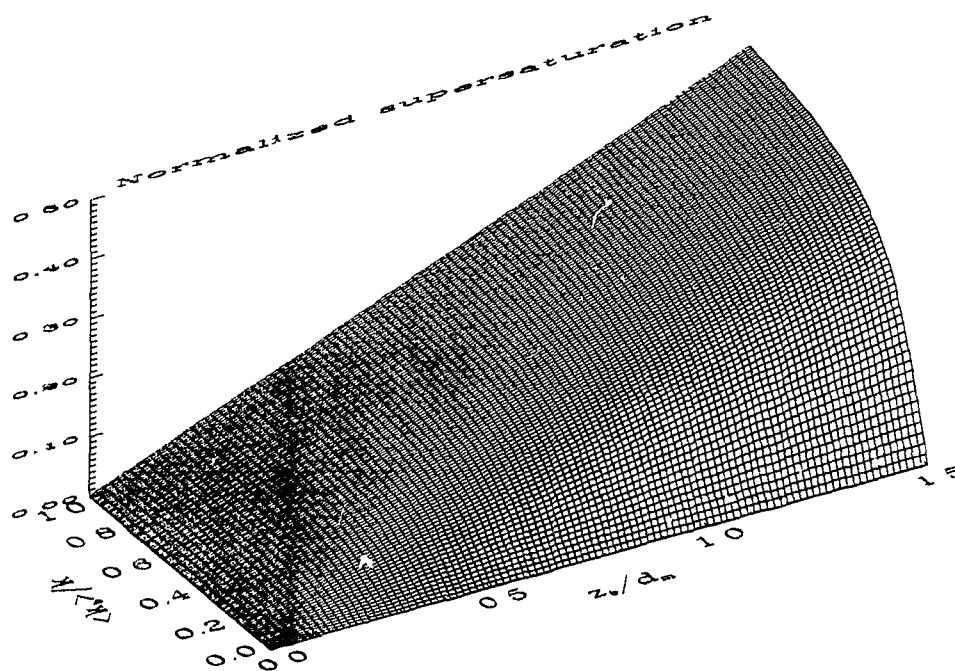
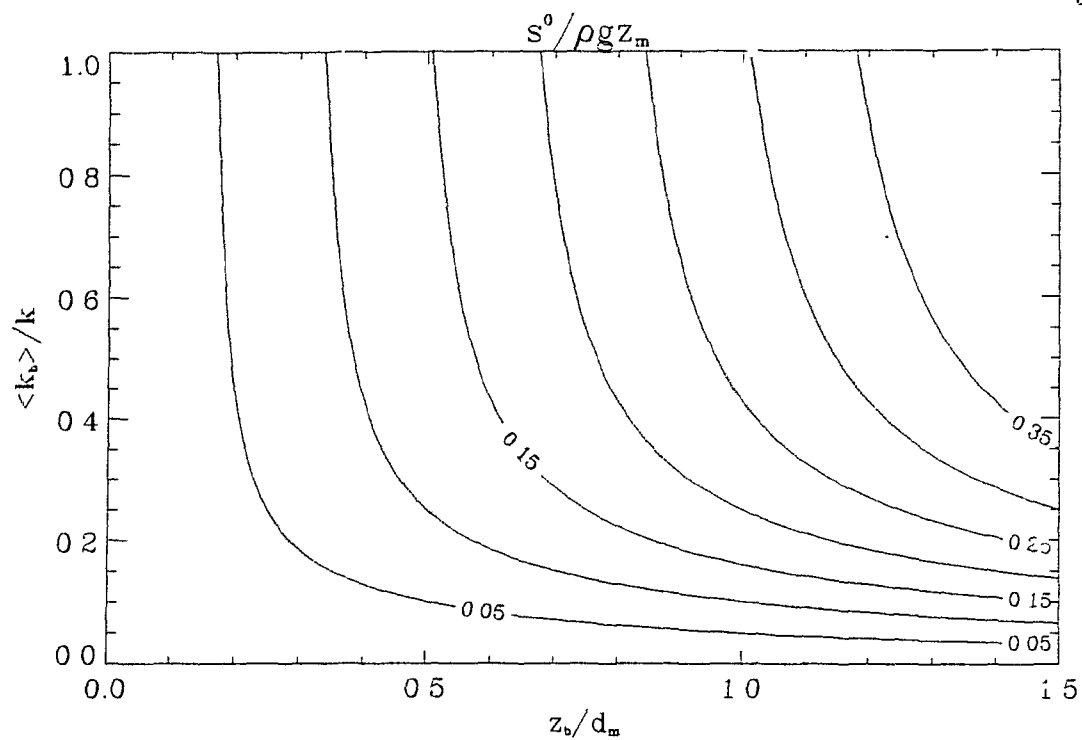


Figure 5.2: Normalized supersaturation as a function of the ratios z_b/d_m and $\langle k_b \rangle / k'$. The normalized supersaturation tends to a maximum value of 0.5 when bubble injection is strong, i.e. at high ratio values.

injection is strong that the steady-state supersaturation becomes independent of the gas properties. Consequently the supersaturations of the four different gases are expected to be much more similar to each other in sea water than they are in fresh water.

5.6.2 Gas tension profiles

The depth-dependent bubble flux model predicts a subsurface maximum in gas tension arising from the product of 1) an exponentially decreasing bubble population with depth, and 2) a linearly increasing driving force for bubble dissolution with depth. In application of the model it is assumed that these depth variations are completely removed by mixing. Other factors that might result in such a gas tension profile and the implications of a subsurface maximum in gas tension are now considered.

Summer profiles of O_2 in the ocean frequently develop a subsurface maximum that is supported by both biological and physical processes (*Shulenberger and Reid, 1981; Jenkins and Goldman, 1985*). Craig and Hayward (1987) measured saturation anomalies for O_2 and the inert gases N_2 and Ar at 5 depths in the top 60–80 m of the North Pacific during summer. Profiles of the inert gases allowed them to separate the physical contributions further into contributions from air injection, pressure deviations from one atmosphere, and temperature changes after equilibration. Although their sampling is meagre, Craig and Hayward's data do show subsurface maxima in the calculated amount of air injected at a depth corresponding to the depth of maximum supersaturation. While this may be an observation in support of the predictions of the DDB model, some cautions must be stated. First, the signal is small. Of a typical 9% saturation anomaly in O_2 , air injection contributes 1.5%, temperature and pressure effects contribute a further 1.5% and biological activity contributes the remainder. Observation of the time and depth evolution of profiles of gas tension, now possible with a field version of the gas tension device, may well be necessary in order to determine if bubble gas fluxes are supporting vertical gradients in gas tension. With sufficient measurements, gas tension may also be a useful tracer of mixed layer deepening. Mixed layer gas budgets involve complex modelling (*Thomas et al., 1990; Spitzer and Jenkins, 1989*) and there is the complication, because gas solubility is a mildly nonlinear function of temperature, that mixing of two saturated waters of different temperatures results in a supersaturation.

If a subsurface maximum in gas tension due to a bubble gas flux persists despite some degree of mixing there are important consequences. Most importantly, the high supersaturations at depth will be insulated from the equilibrium flux that vents excess gas across the water surface by a layer of water with low gas tension. The excess gas in the supersaturated water will then be available for mixing deeper into the water column.

There are consequences for design of gas exchange experiments if gradients in gas tension exist due to bubble-mediated gas flux. It is possible that the GTD could overestimate the average gas tension in the water by registering just the gas tension in the region of the maximum value. However, in these tank experiments, mixing is provided not only by the turbulence associated with the falling water and the motion of the stirring bar, but also by the recycling of the tank water. It is therefore unlikely that gradients in any water properties could persist in the tank experiments. If the average gas tension in the water were overestimated, then, while the calculated k' would be unchanged, the calculated value of k would be underestimated and k_b would be proportionately overestimated.

In equilibrium gas flux models the degree of mixing of the water column, usually wind speed by proxy, is included only for the role it plays in reducing the thickness of the diffusive resistance layer between phases. The bulk fluids are always considered to be well-mixed. Equilibrium gas flux models have met with a reasonable amount of success under calm to moderate conditions, but are clearly not sufficient to describe gas transfer under dynamic conditions. A separate bubble flux has been formulated here, but further improvement in the ability to model gas transfer under dynamic conditions may require replacement of the usual form of equilibrium flux with a revised form, e.g., one appropriate when gradients in gas tension exist down the water column.

5.7 Summary

In this chapter a simple two component model has been developed to describe gas exchange both across the water surface and across the interface provided by injected bubbles. The bubble flux is represented as varying with depth to model typical bubble depth distributions and hydrostatic pressure effects. The driving force for gas exchange in the model is in terms of gas pressures and allows a clear description of the interaction between gas-phase pressure, internal bubble pressure and dissolved gas pressure.

The difference between dissolved gas pressure (gas tension) and gas-phase pressure has been measured directly in the gas exchange experiments reported in Chapter 4. The model provides a tool for analysing these time series and will be applied in Chapter 6. The model allows a combined gas exchange velocity to be calculated, and further separated into components for the equilibrium flux and the bubble flux. The steady-state supersaturations calculated, and observed in some cases, will also serve to indicate the relative contributions of the bubble fluxes for the different gases. Some expected results have been suggested following the observed differences in bubble populations between sea water and fresh water and the discussion on the effects of bubbles on gas transfer.

Using the gas tension method, measurement of profiles of gas tension is a possibility. The consequences of depth variations in gas tension were considered.

Chapter 6

Invasion Experiments with Bubble Injection

6.1 Introduction

The depth-dependent bubble (DDB) flux model that was developed in Chapter 5 is now used to analyse the results of gas-exchange experiments. Many experiments were carried out in the configuration of gas invasion with bubble injection, a configuration for which limited data exist in the oceanographic literature, and this set of results was chosen for further analysis. The results from invasion/bubble-injection experiments with Ar, N₂, CO₂ and He, in both fresh water and sea water, are discussed. The discussion emphasizes a comparison of fresh water and sea water results.

A combined exchange velocity, k' , is determined in the analysis and further separated into components k , for the surface exchange velocity, and $\langle k_b \rangle$, for the bubble exchange velocity using the equations of Chapter 5. The value of the steady-state supersaturation is also calculated. Inputs for each analysis are, 1) time series of p and V , 2) the water depth, d_m ¹, and 3) an arbitrary, but reasonable value for the e -folding depth of $\langle k_b \rangle$, $z_b = 20$ cm. The choice of z_b was made in Chapter 3 and is discussed in section 6.6.2.

First, further experimental details, including temperature measurements, are reported. Then, the exchange velocities and supersaturations are calculated and compared. The

¹Due to displacement of water by equipment in the tank, the actual water depth is greater than d_m , the water volume to free-surface area ratio.

discussion compares the calculated results with those expected and explores temperature and other effects.

6.2 Experiments

6.2.1 Purging

An estimate of the time needed to purge the system of one gas and replace it with the next was made by following the decrease in oxygen when air-saturated sea water was purged with argon. Water samples were withdrawn for Winkler titration analysis. After 22 h the O_2 content was down to 20% of its initial value and after a further 18 h it was at 12% (Figure 6.1), near the detection limit of my Winkler technique. This rate of purging was achieved with the weir tipping and the gas being introduced under the water surface. Consequently at least 40 hours were allowed for initial equilibration with each gas.

6.2.2 Gas-Exchange Experiment Details

Details of the series of fresh and sea water gas invasion experiments with bubble injection are given in Table 6.1.

On average, a 20-mbar step increase was applied to the gas-phase pressure (column 2). In practice the magnitude of the pressure increase was limited to the difference between the initial p , somewhat determined by ambient atmospheric pressure, and the maximum p recordable by the barograph, 1040 mbar. Water vapour pressure is considered to be an invariant 100% of saturation in each phase in the following analyses.

In the seawater experiments, water-phase temperature, T_w , was monitored continuously, otherwise both gas-phase temperature, T_g , and T_w were measured occasionally. Measurement of T_g was prone to inducing leaks in the tank and was consequently taken less often. T_g measurements are generally lower than the corresponding T_w measurement by 0.1 to 0.2°C, most likely because the probe had evaporating water drops on it. Table 6.2 indicates the tight range of temperatures between all experiments. These small temperature differences, on average less than 0.31°C, are small enough to be neglected, as discussed further in Chapter 7.

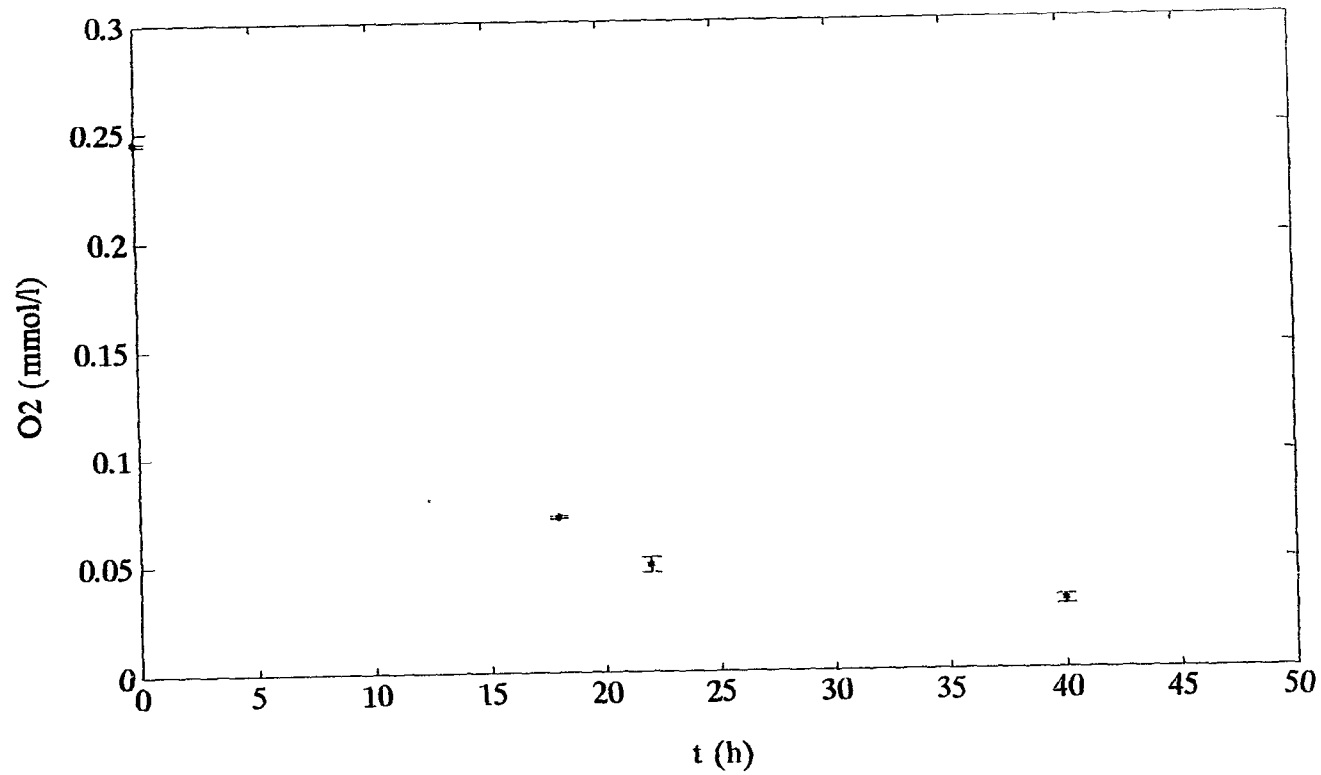


Figure 6.1: Displacement of the oxygen in the experimental tank water by purging with argon. Oxygen measurements by Winkler titration with a detection limit near $3\mu\text{moles l}^{-1}$. Vertical error bars indicate the estimated uncertainty in each measurement.

Experiment I.D.	Δp (mbar)	T_w ($^{\circ}\text{C}$)	T_g ($^{\circ}\text{C}$)	Notes
F.N ₂ .IW67	+18	22.66		
F.N ₂ .IW69	+22	22.68–22.64	22.32–22.46	
F.He.IW75	+29	22.72		
F.He.IW77	+17	22.72	22.66	
F.He.IW79	+24	22.74	22.71	
F.Ar.IW86	+23	22.76	22.59	
F.Ar.IW88	+22		22.60	
F.CO ₂ .IW94	+21	22.59–22.73	22.45–22.7	
F.CO ₂ .IW98	+17	22.79	22.5–22.6	
S.Ar.IW03	wave on			S= 22 psu
S.Ar.IW05	+17	23.15–23.12		S= 22 psu
S.Ar.IW07	+33	23.07–23.05	22.96	S= 22 psu
S.N ₂ .IW16	+8	22.95–22.93		
S.N ₂ .IW18	+15	22.95–22.93		
S.He.IW25	+13	22.96–22.98		gas inlet under water
S.He.IW27	+15	22.97–22.99		gas inlet under water
S.He.IW29	+23	22.99–23.00		gas inlet under water
S.CO ₂ .IW42	--24	22.97–22.99	22.95 \pm 0.01	
S.CO ₂ .IW44	+22	22.96–22.97	22.95 \pm 0.01	

Table 6.1: Invasion experiments with bubble injection--experimental conditions. Under I.D. the gas and conditions are indicated: F for fresh water, S for sea water, I for invasion, and W for 'wave-breaking-with-bubble-injection'. The initial gas-phase pressure step that was applied is in column 2; In the seawater experiments water-phase temperature, T_w (column 3), was monitored continuously, otherwise both T_w and gas-phase temperature, T_g (column 4), were measured occasionally. Seawater salinity was 31.2 psu unless noted otherwise. The accuracy of p measurements improve following experiment S.Ar.IW03 when 'tapping' the bell jar became routine.

Gas	T_w in F, mean \pm max. range (°C)	T_w in S, mean \pm max. range (°C)	ΔT_w (S-F)
N ₂	22.66	22.94 \pm 0.01	0.28
He	22.72 \pm 0.01	22.98 \pm 0.02	0.26
Ar	22.76	23.07 \pm 0.06	0.31
CO ₂	22.73 \pm 0.05	22.97 \pm 0.02	0.24
	22.73 \pm 0.07	22.99 \pm 0.08	0.26

Table 6.2: Temperature range between experiments

The setting of the variable-flow-rate pump was unchanged over the course of the experiments. Three different estimates of the flow rate were made during the time the experiments were being carried out.

- 1) The volume dumped by the bucket was measured at 770 cm³ and divided by the dumping interval of 82 s to calculate a water flow rate of 0.56 l min⁻¹.
- 2) The flow from the tubing at the point where it normally entered the bucket was collected in a measuring cylinder. The flow rate was measured at 0.55 l min⁻¹.
- 3) During draining and refilling of the tank, water depth was seen to be changing at approximately 0.35 cm min⁻¹. From the surface area of water in the tank the flow rate was then estimated at 0.54 l min⁻¹. This measurement is the least accurate of the three.

The bucket was delicately balanced so that it would dump its accumulated load and return to a resting position where it would again accumulate water. Unavoidably the balance was interfered with every time the lid of the tank was disturbed and consequently more frequent in situ flow rate measurements were not made. Even while the water flow rate did not change, the dumping frequency could change, if the balance of the bucket were upset so that it would hold a smaller or larger quantity of water before it became unstable. The dumping frequency was measured by two methods.

- 1) By directly timing the bucket dumps. The dumping interval at the end of the series of fresh water experiments was 69.4 s with a standard deviation of less than 0.5 s.
- 2) When the bucket dumped its load there was a blip in the voltage recorded on the chart recorder. This was easily resolved under some conditions and not under others. During a He invasion experiment into sea water the dumping interval was calculated to be 90 s.

Since the water flow rate is the same in each case, the volume of air entrained as bubbles

will be the same over comparable periods of time. There is not expected to be any difference in the gas exchange rates due to the different frequency of bubble injection. However it is more difficult to estimate the effect of different degrees of mixing when larger or smaller volumes of water are dumped. Better control over the volume/frequency of dumping events would have been desirable in retrospect.

6.3 Review of Analysis Technique

As outlined in section 5.4, the technique is to fit an expression of the form $P = f(a, b, p, t)$, derived from the depth-dependent bubble flux model, to the observed time series of gas tension. The fit is optimized by brute force: varying coefficients a and b and selecting those values which minimize the root mean square error between observed and calculated gas tension. An e -folding depth of penetration of the bubble population is then used to resolve the coefficients into two gas exchange velocities.

First the differential gas pressure, $P - p$, is evaluated from the raw voltage by adjusting for the offset at zero differential pressure and dividing by the voltage to pressure calibration ratio (equation 4.1). Gas tension, P , is evaluated by adding the discrete data for p (from barograph records), to the differential pressure.

A subset of data is selected for analysis by inspection of gas-phase pressure. Typically the 'step' increase in p is established over 15 minutes and a cubic function adequately describes the subsequent pressure changes. The start point is selected where dp/dt is first $\leq 0.1\text{mbar min}^{-1}$. The end point is chosen as the shorter of 400 min or the end of the time series. The cubic fit is strongly controlled by the start of the time series, when more measurements were made, which is desirable because most of the response is in the first 100 minutes and therefore it is critical that this portion of the data be well described.

In order to calculate differences between calculated and observed time series it is necessary to have observations at the same times in each series. The original observations were recorded continuously, but were manually subsampled at non-uniform time intervals. Rather than make the comparisons on this basis, a more uniform time grid for sampling and comparing the functions is generated. First, the continuous nature of the initial observations is regenerated by fitting natural cubic splines to the discrete observations of gas tension and gas-phase pressure, functions P_{obs} and p_{obs} respectively. The average sampling

interval from the early (first 60 min) subset of discrete data is used to subsample the first 60 min of continuous data. Similarly the average sampling interval from the remaining discrete data is used to subsample from 60 min for the duration of the observations. Typically the resulting sampling frequencies are once every 5 min and once every 15 min. The total number of 'subsamples' taken from the functions is then similar to the number of data points in the discretized series and becomes the factor N used in calculation of root mean square errors (rms).

Using equation 5.20, P_{calc} is evaluated for a range of a and b values. Optimal values for a and b are found through iteration as those values which generate the minimum rms error between P_{calc} and P_{obs} . At the optimal value of a , a value for b which increases the minimum rms error by a factor $\sqrt{2}$, and likewise at the optimal value of b , a value for a which increases by $\sqrt{2}$ the minimum rms error, are recorded as an indication of the sensitivity of the fit to the coefficients. If just a small change in a coefficient increases the minimum rms error by $\sqrt{2}$, then the optimal coefficients are known with relatively high precision.

P_{calc} generated from equation 5.20 is then compared visually with P_{obs} . If the minimum rms error is small (< 0.4 mbar) and the fit is especially satisfactory over the first 100 min or so (as indicated by time series of errors) then further calculations to yield gas-exchange velocities are made. If, however, the fit is poor at the beginning of the series and is reflected in a high minimum rms error then a further short segment of data is dropped and a reevaluation of coefficients made. Typically the reason for a poor fit of calculated to observed gas tension is due to variable gas-phase pressure. For experiment s.Ar.IW05 the minimum rms error for the data subset was initially 0.61 mbar, but improved to 0.53 mbar on dropping the next data point (one minute) and further improved to 0.35 mbar by dropping the following data point (5 minutes) (Figure 6.2).

Further inputs required for the calculation of exchange velocities and steady-state supersaturations are the calculated water depth, d_m and the e -folding depth of bubble penetration. The combined exchange velocity, k' , and the steady-state supersaturation, s^0 , are calculated from ad_m and b/a respectively. The relevant equations are 5.21 and 5.22 as detailed in Chapter 5. The subsequent steps to separate the combined exchange velocity into its components are to calculate I (equation 5.10), c_1 (equation 5.9), and c_2 (equation 5.12). The equation for s^0 (5.23) is then rearranged and the appropriate values substituted to

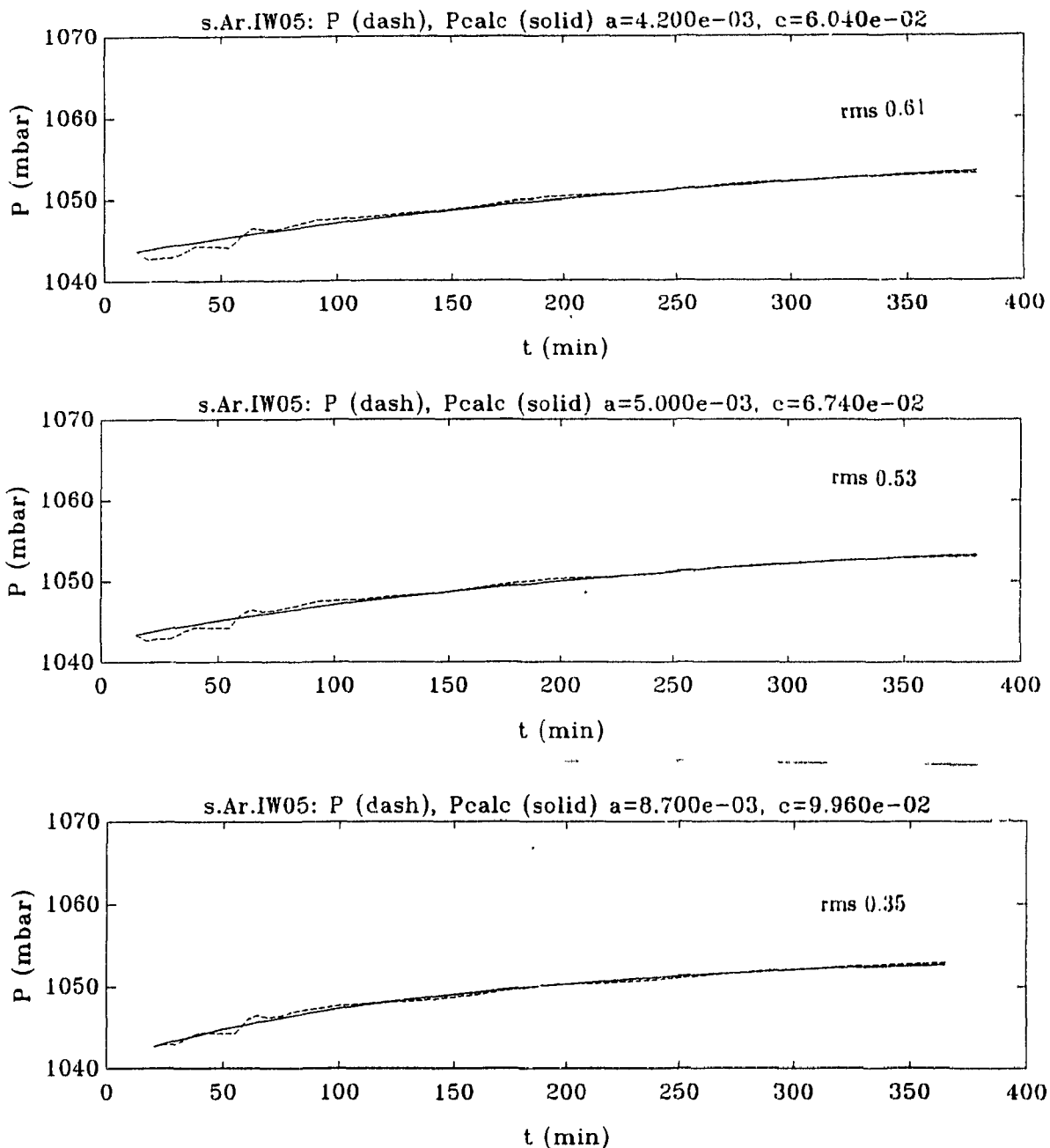


Figure 6.2: A starting time for analysis of experiment s.Ar.IW05. is first suggested by where dp/dt becomes small (at $t=14$ min). But inspection shows (top figure) that the minimum rms error is large due to a poor fit at the beginning. A smaller error is found by starting at the next data point, one minute later (middle figure). Dropping the next discrete data point (and another 5 minutes) improves the error to a satisfactory 0.35 mbar (bottom figure).

solve for $\langle k_b \rangle$,

$$\langle k_b \rangle = \frac{k' s^0}{\rho g d_m c_2 / c_1} \quad (6.1)$$

The surface exchange velocity is given by the difference between k_b and k' (equation 5.2.5).

Supersaturation at steady state is calculated both as an absolute value, s^0 (equation 5.2.3), and as a percentage (of the mean gas-phase pressure), Δ^0 . The gas-phase pressures between experiments are quite similar so the percentage values for different experiments may be compared directly.

6.4 Results Example

Duplicate CO₂ invasion experiments in sea water are analysed as examples. Figure 6.3 (top) shows observed p and P in the first experiment (s.CO₂.IW42). The cubic fit to p over the selected portion is shown below (rms=0.1 mbar). Gas tension calculated from the optimal coefficients ($a = 0.0109 \text{ min}^{-1}$ and $b = 0.0927 \text{ mbar min}^{-1}$) is compared to P_{obs} in the third plot. Below are shown time series of the difference between P_{calc} and P_{obs} . The optimal coefficients result in a minimum rms error of just 0.1 mbar. A similar sequence of plots is shown in Figure 6.4 for the second experiment (s.CO₂IW44). The optimal coefficients agree to within $\pm 5\%$ in a and to within $\pm 3\%$ in b between the two experiments. Gas-phase pressure was particularly steady over the duration of these two experiments, contributing to better than average data quality.

The GTD measurement is sensitive to at least ± 0.05 mbar. At best p is measured with a precision of ± 0.1 mbar, but poor time resolution in the barograph records can double this in periods when p is changing. From equation 5.20 it is seen that uncertainty in dp/dt also contributes to uncertainty in $P(t)$. For example, if $dp/dt = 2.0 \pm 0.4 \text{ mbar h}^{-1}$ and d_m/k' approximately 1 h^{-1} , the uncertainty contributed to P is 1.2 mbar. The response time of the instrument may introduce an offset between p and P , apart from any offset introduced by the data handling. These contributions to uncertainty are sufficient to explain the differences between the duplicate CO₂ experiments. By simply improving gas-phase pressure measurement and removing manual data handling, the uncertainties in the method would be improved to better than 1%.

The average values of the slopes is multiplied by the water depth, d_m , to give a combined

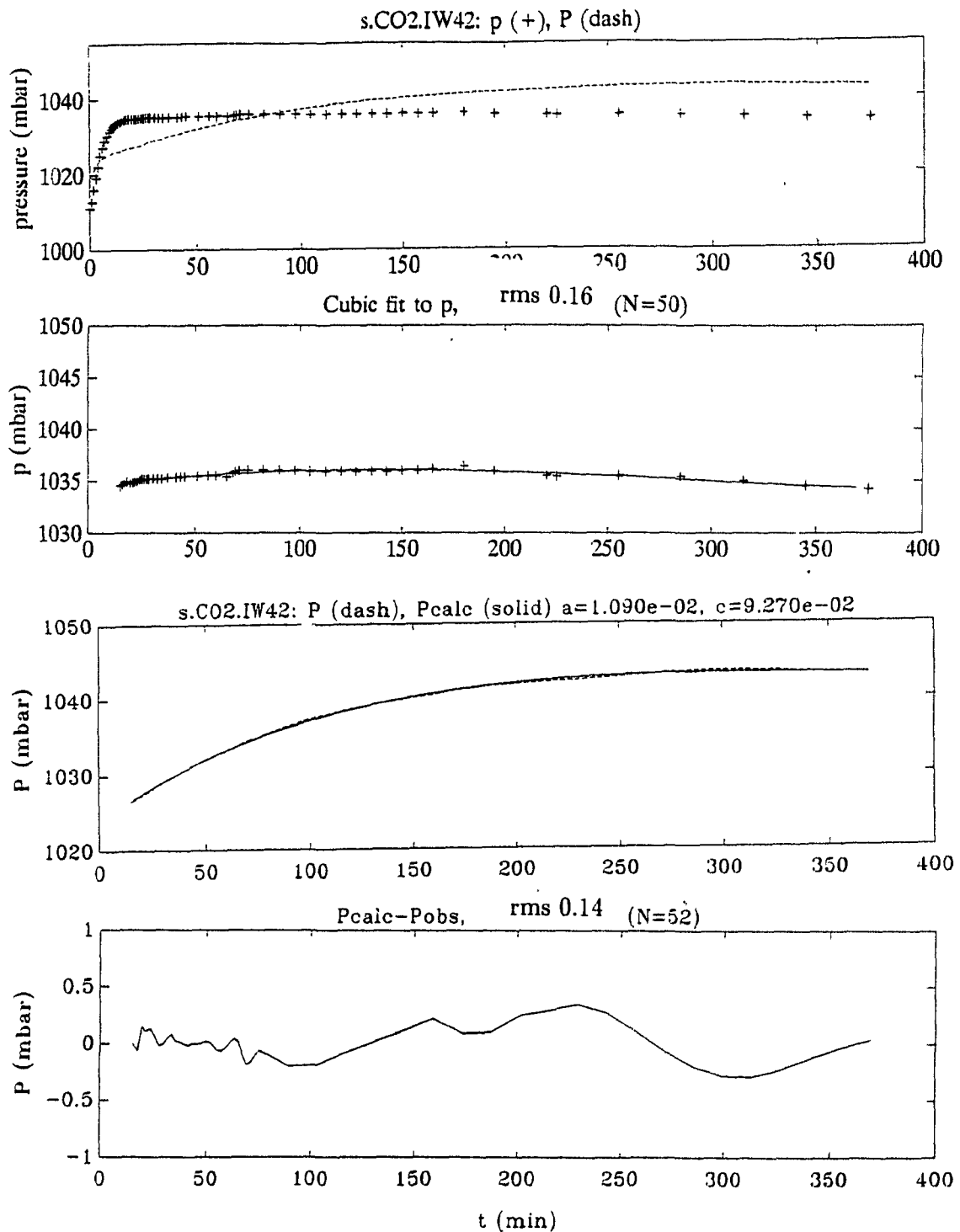


Figure 6.3: CO₂ invasion into sea water with bubble injection (see figure 4.5 for raw voltage). Topmost plot shows observed values of p and P . Below the cubic fit to p over a subset of the time series is illustrated. In the third plot P_{calc} evaluated using the optimal coefficients a and b is compared to P_{obs} (the natural spline fit to the observed values of P). Time series of the error in the fit is shown beneath.

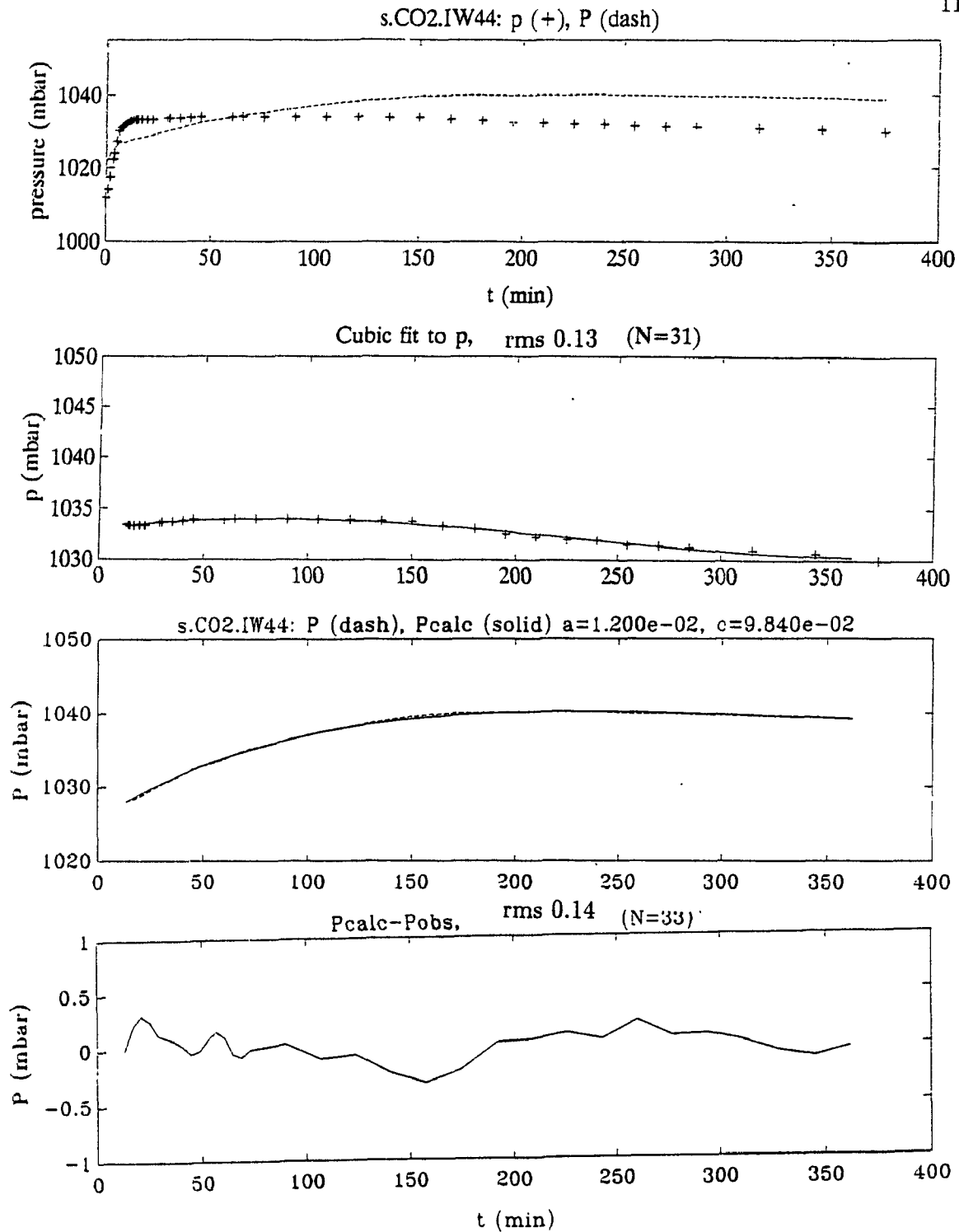


Figure 6.4: CO₂ invasion into sea water with bubble injection (duplicate) see figure 4.6 for corresponding raw data. Topmost plot shows observed values of p and P . Below the cubic fit to p over a subset of the time series is illustrated. In the third plot P_{calc} evaluated using the optimal coefficients for a and b is compared to P_{obs} . Time series of the error in the fit is shown beneath.

Experiment	a (min^{-1})	δa (min^{-1})	b (mbar min^{-1})	δb (mbar min^{-1})	rms (mbar)
S.CO ₂ .IW42	0.0109	0.0003	0.0927	0.0024	0.1
S.CO ₂ .IW44	0.0120	0.0004	0.0984	0.0024	0.1
	k' (cm h^{-1})	k (cm h^{-1})	$\langle k_b \rangle$ (cm h^{-1})	s^0 (mbar)	Δ^0 (%)
Mean	21.4	6.2	15.3	8.3	0.81
St. dev.	1.5	0.8	0.6	0.2	0.02

Table 6.3: Duplicate CO₂ invasion-into-seawater with bubble-injection experimental results. Tabulated are the optimal values of coefficients a and b , along with the incremental increase in each that increases the root mean square error (rms) by $\sqrt{2}$. Water depth $d_m = 31.2$ cm, and bubble penetration depth $z_b = 20$ cm are used with a and b to calculate the remaining values. Tabulated are the mean and standard deviation between the two experiments of the combined exchange velocity, k' , surface exchange velocity, k , the depth-averaged bubble exchange velocity, $\langle k_b \rangle$, absolute and percent supersaturations, s^0 and Δ^0 .

exchange velocity of 21.4 ± 1.5 cm h⁻¹. Such an exchange velocity is expected for u_{10} wind speeds around 11 m s⁻¹. At wind speeds of 11 m s⁻¹ the frequency of wave breaking in natural waters is 0.019 ± 0.004 s⁻¹, or about once every minute, as inferred from Thorpe and Humphries' figure 1 (Thorpe and Humphries, 1980). The frequency of breaking of the simulated wave was also about once every minute. The combined exchange velocity measured in the experimental tank is in the range of exchange velocities expected under some reasonable conditions in the field.

The bubble exchange velocity is more than double the surface exchange velocity and the net result is a supersaturation of nearly 1%.

6.5 Results

P_{obs} determined from the GTD response to the step change applied in p is compared to P_{calc} for a subset of the experiments (Figures 6.5-6.11). The coefficients a and b indicated in the figures are in units of min^{-1} and mbar min^{-1} respectively.

The full set of calculated results are tabulated in Table 6.4 and illustrated in Figure 6.12. In each case the results are the average of two or more experiments (those tabulated in Table 6.1). Uncertainties are stated as the standard deviation about the mean of the

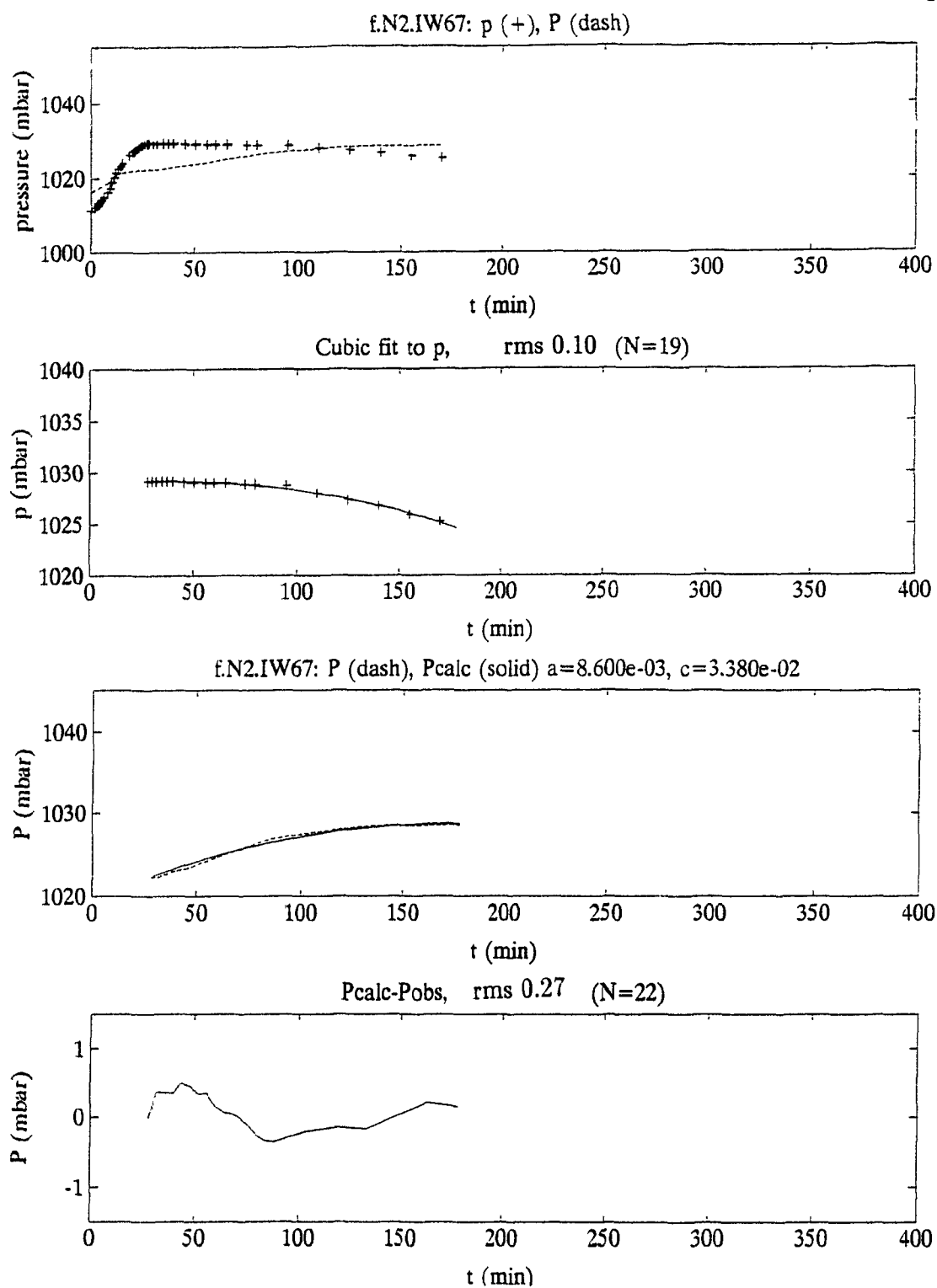


Figure 6.5: N_2 invasion into fresh water with bubble injection. See Figure 4.10 for raw data. Observed p and P in the top plot are followed by the cubic fit to p over a subset of the data. The lower two figures compare P_{calc} and P_{obs} .

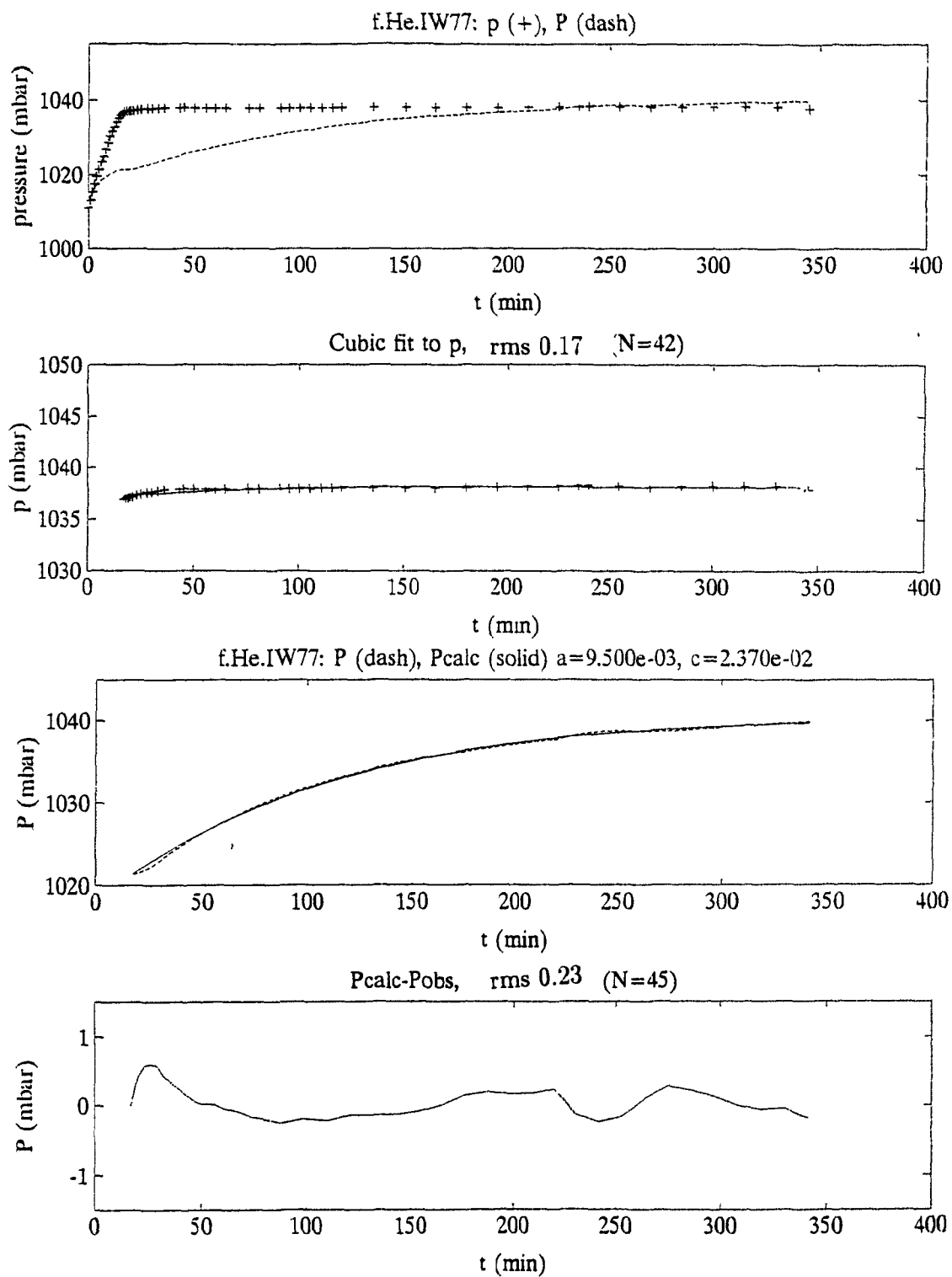


Figure 6.6: He invasion into fresh water with bubble injection. See Figure 4.9 for raw data. Observed p and P in the top plot are followed by the cubic fit to p over a subset of the data. The lower two figures compare P_{calc} and P_{obs} .

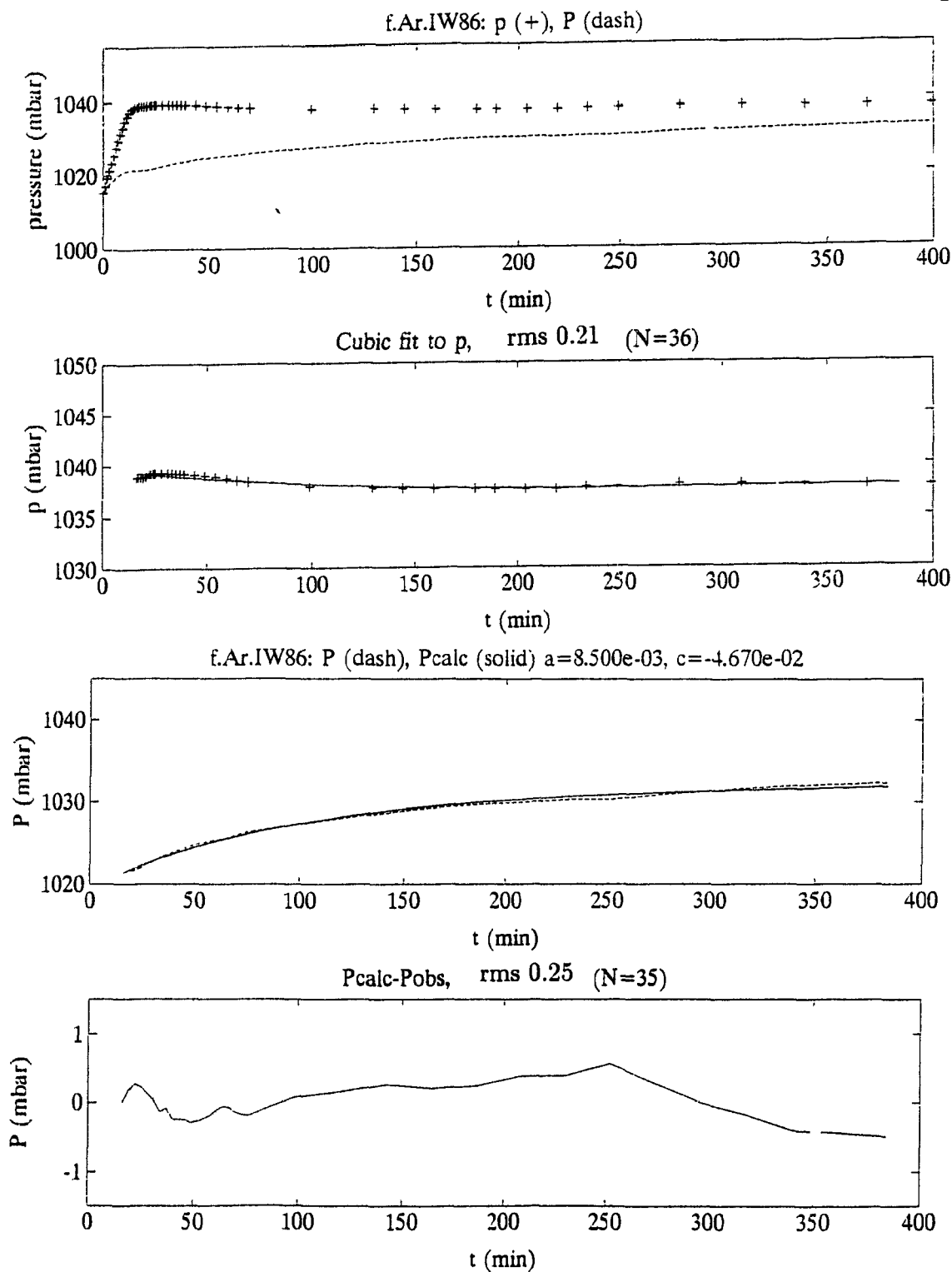


Figure 6.7: Ar invasion into fresh water with bubble injection. Observed p and P in the top plot are followed by the cubic fit to p over a subset of the data. The lower two figures compare P_{calc} and P_{obs} .

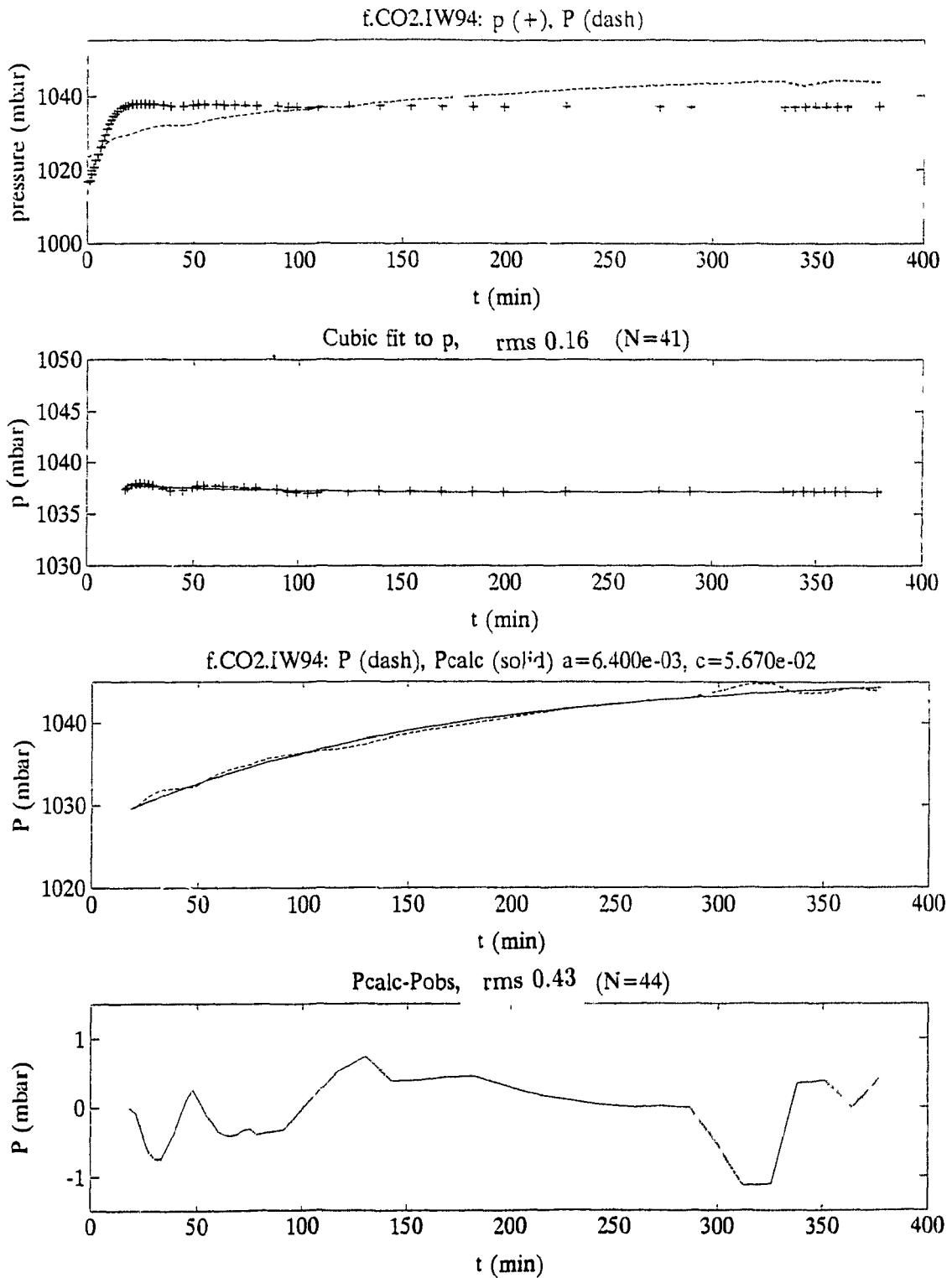


Figure 6.8: CO₂ invasion into fresh water with bubble injection. Observed p and P in the top plot are followed by the cubic fit to p over a subset of the data. The lower two figures compare P_{calc} and P_{obs} .

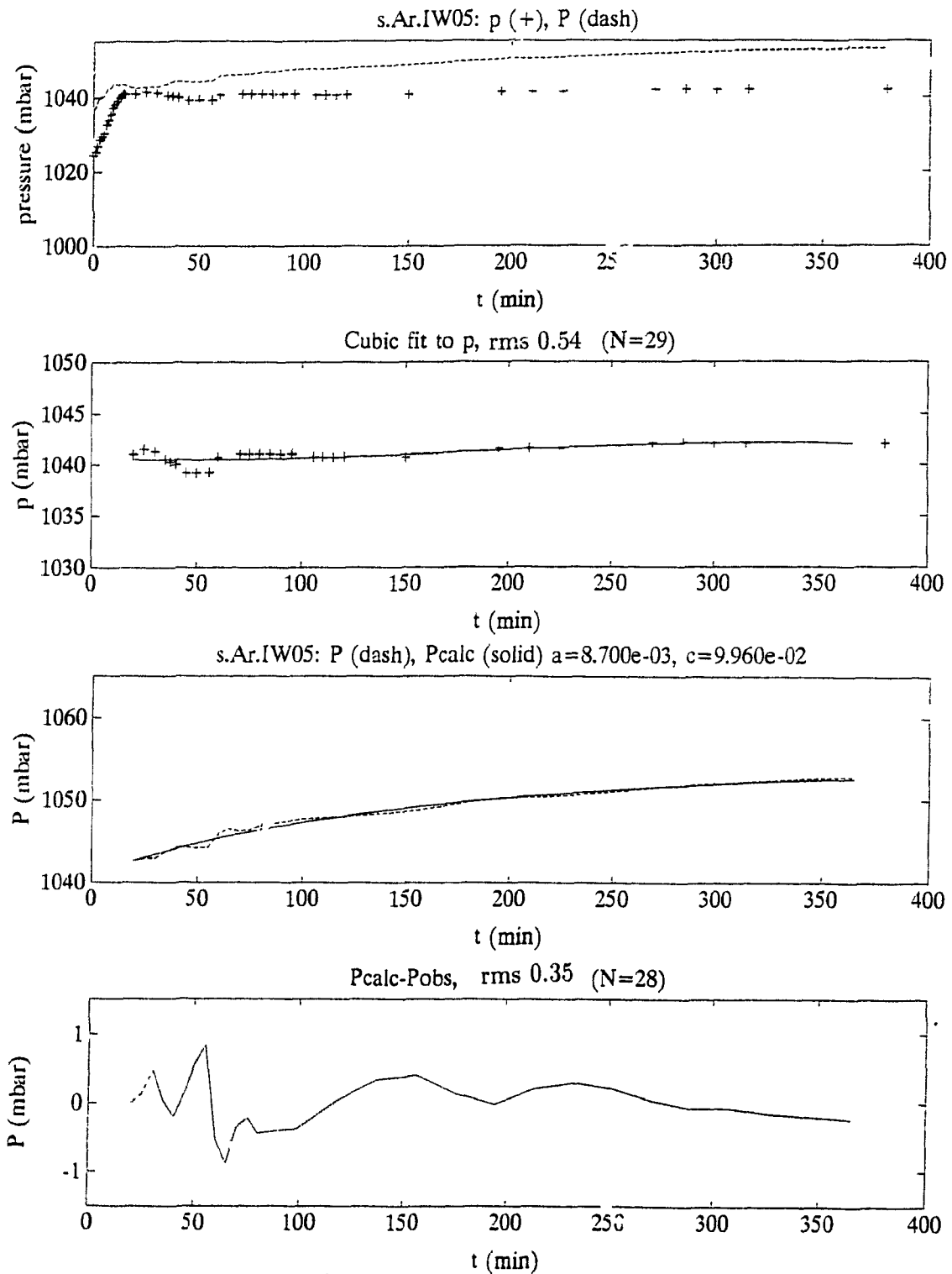


Figure 6.9: Ar invasion into sea water with bubble injection. Observed p and P in the top plot are followed by the cubic fit to p over a subset of the data. The lower two figures compare P_{calc} and P_{obs} .

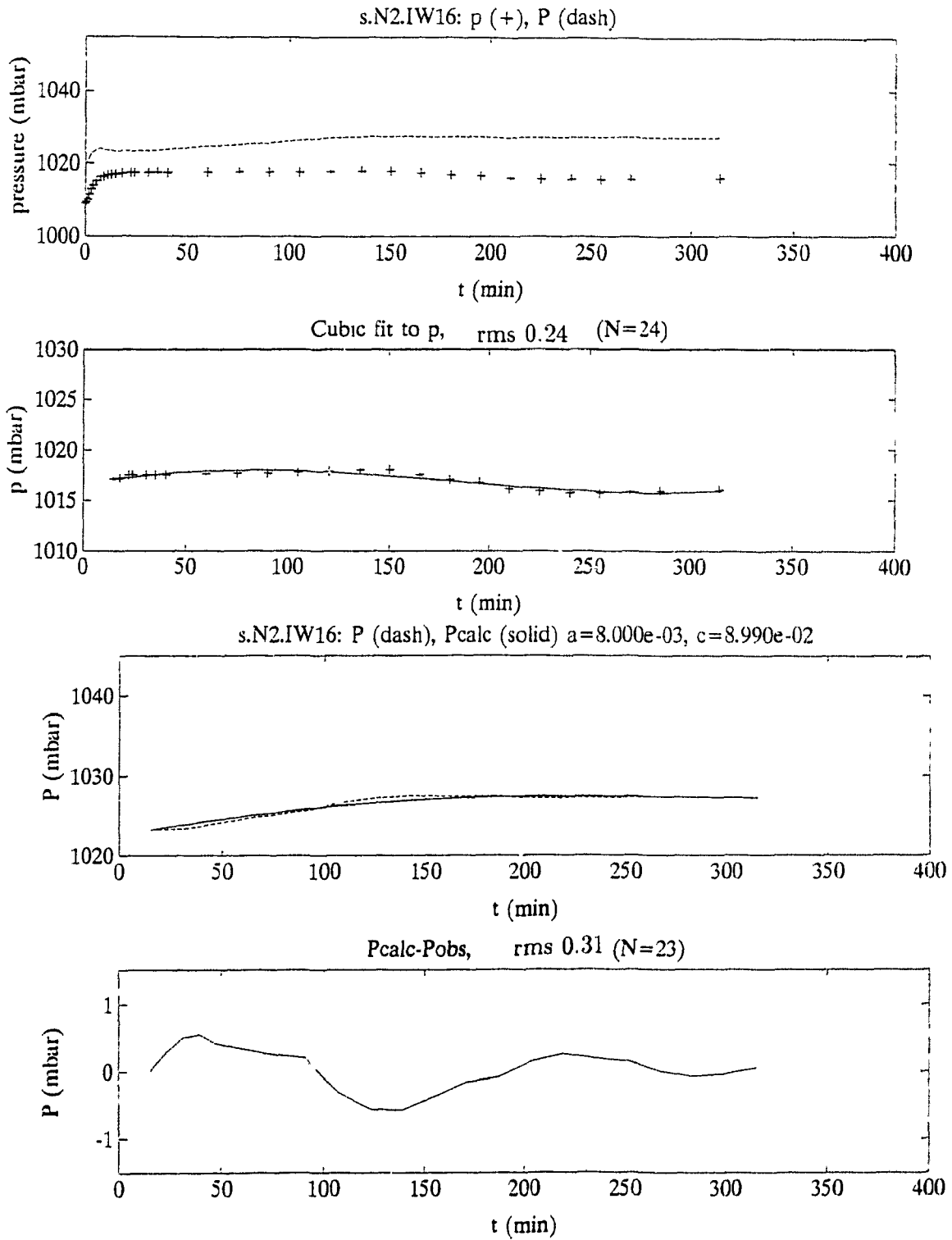


Figure 6.10: N_2 invasion into sea water with bubble injection. Observed p and P in the top plot are followed by the cubic fit to p over a subset of the data. The lower two figures compare P_{calc} and P_{obs} .

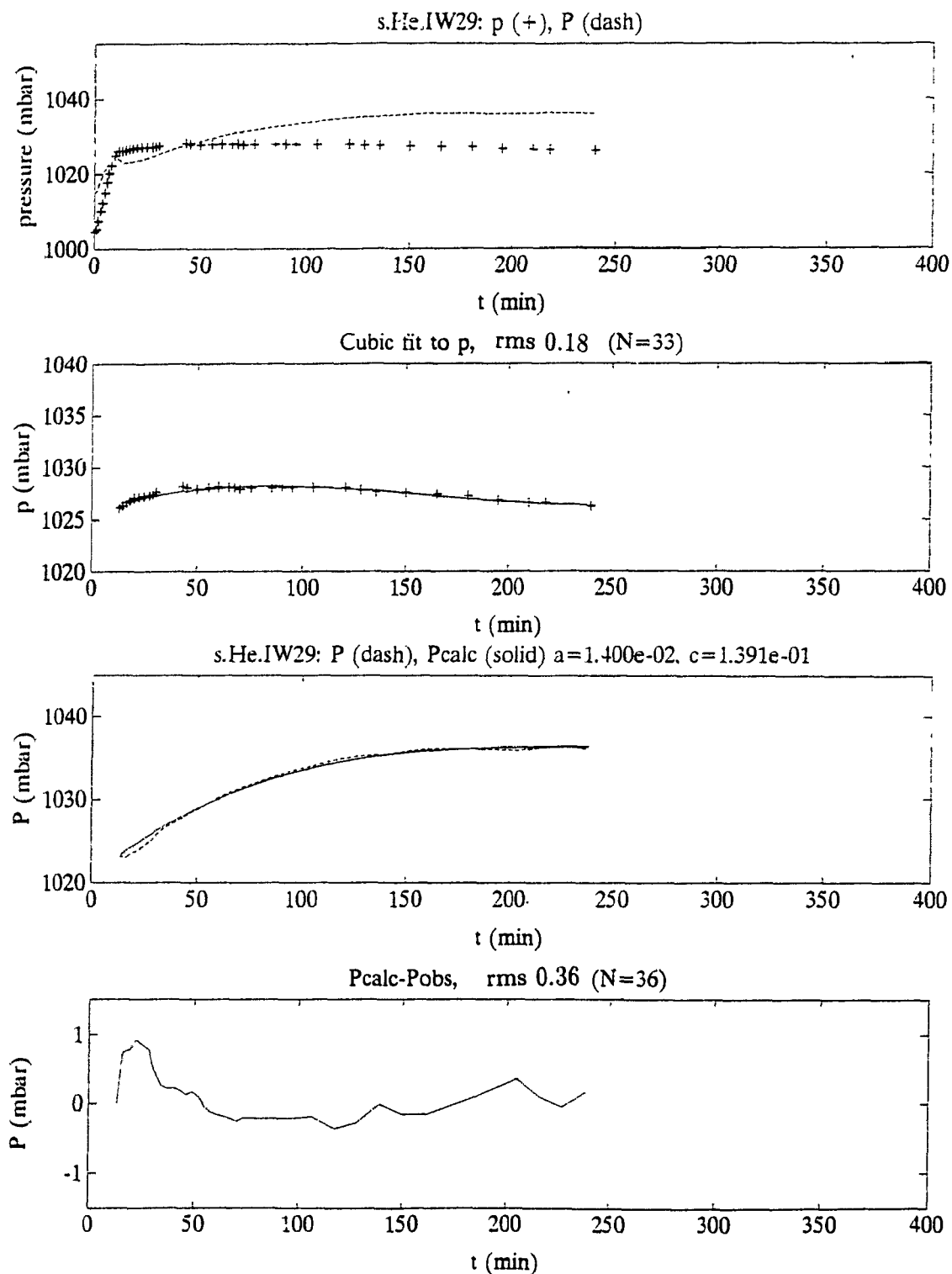


Figure 6.11: He invasion into sea water with bubble injection. See Figure 4.8 for raw data. Observed p and P in the top plot are followed by the cubic fit to p over a subset of the data. The lower two figures compare P_{calc} and P_{obs} .

averaged runs. The following section describes in words the same information given in Table 6.4 with an emphasis on a comparison between the seawater and freshwater results.

6.5.1 Combined gas-exchange velocity, k'

Combined gas-exchange velocities (lower column 3 of Table 6.4) have uncertainties that average 7% (except for Ar in fresh water, whose uncertainty is considerably higher).

Fresh water: k' values for CO₂, Ar and N₂ are all the same 14 cm h⁻¹ within the limits of uncertainty. k' for He is 35% higher than for the other gases.

Sea water: k' for N₂ and Ar are around 17 cm h⁻¹, for CO₂ about 25% higher, and for He about 60% higher than the N₂ and Ar values. The Ar experiments were inadvertently carried out in sea water with lower salinity (22 psu) than the other experiments (31.2 psu). The differences arising in solubility, diffusivity and bubble populations due to the small difference in salinity are not considered significant.

S-F comparison: k' s for Ar and N₂ are about the same, or slightly higher, in sea water compared to fresh water. For both CO₂ and He the values of k' are about 50% higher in sea water than in fresh water.

6.5.2 Surface gas-exchange velocity, k

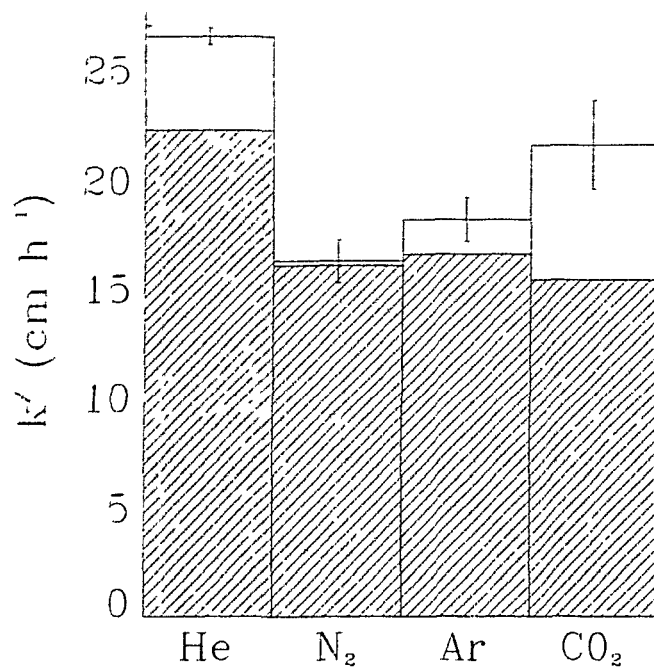
The gas-exchange velocities for exchange across the free surface (lower column 4 of Table 6.4), calculated according to the DDB model, are described and compared in this section. Since k is calculated as the difference between k' and $\langle k_b \rangle$, when k is a small component of the combined exchange velocity the uncertainty in its value is correspondingly high.

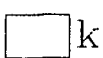
Fresh water: Rather a wide range of k values, from 4.4 cm h⁻¹ for CO₂ to 17 cm h⁻¹ for Ar, are calculated. The separation of k' for Ar into components k and k_b is suspect, as illustrated by the negative values calculated for $\langle k_b \rangle$ and supersaturations.

Sea water: Values for k range from 0.2 cm h⁻¹ for N₂ to 6.2 cm h⁻¹ for CO₂.

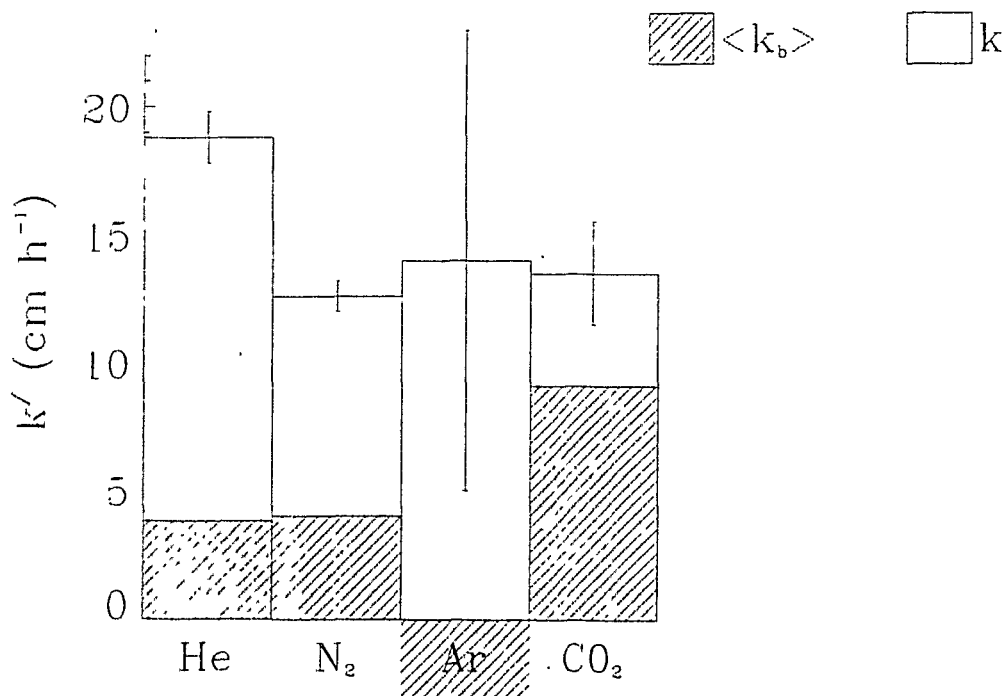
S-F comparison: Overall, the k values for CO₂ are about the same in fresh water compared with sea water, while for the other gases k is significantly depressed in sea water compared with fresh water, even given the fairly high uncertainties.

Seawater



 $\langle k_b \rangle$  k

Fresh water



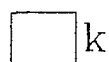
 $\langle k_b \rangle$  k

Figure 6.12: Combined gas-exchange velocities are illustrated as the sum of bubble and surface exchange velocities. The gases are listed left to right in order of increasing solubility.

Water.Gas	a (h^{-1})	δa (h^{-1})	b (mbar h^{-1})	δb (mbar h^{-1})	rms (mbar)	d_m (cm)
S.CO ₂	0.69 ± 0.05	0.05	5.7 ± 0.2	0.3	0.14	31.7
F.CO ₂	0.44 ± 0.07	0.14	3.41 ± 0.01	0.3	0.33	31.15
S.He	0.85 ± 0.01	0.10	8.3 ± 0.1	0.3	0.33	31.7
F.He	0.61 ± 0.04	0.04	1.4 ± 0.2	0.4	0.20	31.2
S.N ₂	0.50 ± 0.04	0.06	5.8 ± 0.6	0.7	0.30	31.7
F.N ₂	0.50 ± 0.02	0.1	1.7 ± 0.5	0.7	0.22	26.5
S.Ar	0.51 ± 0.04	0.05	5.9 ± 0.6	0.7	0.27	35.4
F.Ar	0.44 ± 0.10	0.10	(-1.3 ± 2.4)	1.3	0.25	31.1
Water.Gas	n	k' (cm h^{-1})	k (cm h^{-1})	$\langle k_b \rangle$ (cm h^{-1})	s^0 (mbar)	Δ^0 (%)
S.CO ₂	2	21 ± 2	6.2 ± 0.8	15.2 ± 0.6	8.3 ± 0.2	0.81
F.CO ₂	2	14 ± 2	4.4 ± 2	9.09 ± 0.03	8 ± 1	0.8
S.He	3	27.0 ± 0.4	4.3 ± 0.7	22.2 ± 0.4	9.8 ± 0.3	0.95
F.He	3	19 ± 1	15 ± 1	3.8 ± 0.5	2.3 ± 0.3	0.23
S.N ₂	2	16 ± 1	0.2 ± 0.5	16 ± 2	11.5 ± 0.4	1.13
F.N ₂	2	12.9 ± 0.6	8.6 ± 0.6	4 ± 1	3.4 ± 0.8	0.33
S.Ar	3	18 ± 1	1.6 ± 0.4	16.5 ± 1.5	11.6 ± 0.4	1.12
F.Ar	2	14 ± 9	(17 ± 8)	(-3 ± 0.5)	(-2.8 ± 0.6)	(-0.27)

Table 6.4: Gas-exchange velocities - summary of experimental results. Abbreviations are F for fresh water, S for sea water, and other symbols as introduced in the text (see list of symbols). Tabulated are the mean values of n experiments \pm one standard deviation. A value of $z_b = 20$ cm is used. Values in brackets are suspect. See Table 6.1 for additional experimental notes.

6.5.3 Bubble exchange velocity, $\langle k_b \rangle$

The bubble exchange velocities (lower column 5 of Table 6.4), calculated from the combined exchange velocity according to the DDB flux model, are described and compared in this section. Uncertainties in the values average 9.5% (excluding Ar in fresh water).

Fresh water: A negative value of $\langle k_b \rangle$ for Ar is anomalous and matches a similarly anomalous result, with large uncertainty, for the k in fresh water. There were no problems apparent with the experiment. The $\langle k_b \rangle$ for CO₂, at 9 cm h⁻¹, is roughly double the value for the other gases.

Sea water: $\langle k_b \rangle$ values for N₂, Ar and CO₂ are all high and similar at about 16 cm h⁻¹. The value for He, at 22 cm h⁻¹, is 40% higher than the other gases.

S-F comparison: Significantly higher $\langle k_b \rangle$'s are determined in sea water compared with fresh water. Factors are approximately 4× for N₂, 2× for CO₂ and 6× for He.

6.5.4 Steady-state saturation anomaly, s^0 and Δ^0

The percent steady-state saturation anomalies (lower column 7 of Table 6.4) are described and compared in this section.

Fresh water: Values range from 0.8% for CO₂ to 0.2% for He with an average of 0.5% (Ar excluded).

Sea water: Values range from 0.8% to 1.1% with an average for all four gases of 1.0%.

S-F comparison: In general, Δ^0 's in fresh water are smaller than those found in sea water. CO₂ is the exception, for which values are the same in both media.

6.6 Discussion

6.6.1 Gross features: k' , Δ^0

As expected, a combination of the most efficient conditions (seawater bubble population, low gas solubility, and high gas diffusivity) produced the highest combined gas exchange velocity: a combined exchange velocity of 27 cm h⁻¹ was measured for He invasion into sea water.

The importance of the bubble population in determining combined gas exchange velocities was demonstrated by the fact that, for every gas, the combined exchange velocity into

sea water was higher than the combined exchange velocity into fresh water, despite the gas property factors working to the opposite effect. Solubilities are lower in sea water compared with fresh water by typically 14% due to a 'salting out' effect (Weiss, 1970; Weiss, 1971; Weiss, 1974). Diffusivities, although there are few actual measurements, are also lower in sea water compared with fresh water by 3% to 7% (Jähne *et al.*, 1987a). The cause is principally the higher viscosity of sea water over fresh water (Horne, 1969). In the empirical formula of Wilke and Chang (1955) $D \propto \mu^{-1}$. Under conditions where the exchange velocity is considered to be proportional to $Sc^{-1/2}$, and thus to $(\mu/D)^{-1/2}$, the exchange velocity is then seen to be proportional to μ^{-1} . The kinematic viscosity, μ , is $1.100 \times 10^{-6} \text{ m}^2 \text{ s}^{-1}$ in sea water (S=34 psu) and $1.004 \times 10^{-6} \text{ m}^2 \text{ s}^{-1}$ in fresh water at 20°C. So the 10% increase in viscosity in sea water over fresh water is expected to decrease the exchange velocity by 10% between the two media. Consequently, it is expected that, as well as sea water taking up less gas than fresh water due to the lower gas solubilities in sea water, that rates of equilibration would be slower in sea water compared with equilibration rates in fresh water. Slower rates of equilibration in sea water compared with fresh water of order 20 to 30% are reported in the literature both for He in gently stirred systems (Weiss, 1971) and from the dissolution of single air bubbles (Wyman *et al.*, 1952; Detsch, 1990). The fact that clearly the converse was found in these experiments suggests that bubble populations play a primary role in determining total gas exchange rates. This result calls out for a further examination of the combined exchange velocity in terms of a component for the surface exchange and a separate component for transfer via bubbles. The bubble contributions to the combined exchange velocity may then be compared between fresh water and sea water to investigate the relative importance of gas properties and bubble populations.

The combined exchange velocity of He is significantly higher than the k 's of the other gases under the same conditions. Qualitatively this result is expected from diffusivity considerations. The diffusivity of He, at about $7 \times 10^{-5} \text{ cm}^2 \text{ s}^{-1}$, is 3.5 times higher than the diffusivities of the other gases, which all have values about $2 \times 10^{-5} \text{ cm}^2 \text{ s}^{-1}$. The exponent n_D in $k' \propto D^{n_D}$ evaluated from these 'bubbly regime' experiments from the ratio

$$n_D = \frac{\ln(k'_{He}/k'_{N_2})}{\ln(D_{He}/D_{N_2})} \quad (6.2)$$

is 0.31 ± 0.06 in fresh water and 0.42 ± 0.02 in sea water. However, in sea water CO_2 has a significantly higher k' than the other gases with similar diffusivities. These experiments

suggest that the Sc dependence of exchange velocity for sparingly soluble gases in bubbly regimes is lower than that established for 'rough surface' regimes ($n = 0.5$), in agreement with the results of Asher et al. (1991). There is also a suggestion from the data that the value of the exponent might be lower in fresh water compared with sea water, although the uncertainties in the limited data set are high. Also it appears, in particular for highly soluble CO_2 , that the combined exchange velocity is not solely a function of Sc .

The steady-state saturation anomaly appears to be largely determined by salinity through the effect of salinity on the bubble population. The combined exchange velocities were all found to be higher in sea water than in fresh water. Also, the surface exchange velocity is expected to be lower in sea water than in fresh water, based on viscosity and related diffusivity arguments. Consequently it is not surprising that the calculated steady-state supersaturations are found to be significantly higher in sea water than fresh water. In agreement with many other observations, for example (*Monahan and Zietlow, 1969; Zieminski and Whittemore, 1971; Scott, 1975*) there were differences between the bubble population in sea water compared with that in fresh water that were obvious to even the casual observer. In sea water the plume was a dense cloud of small bubbles, many of which persisted for 5 seconds or more. In fresh water the bubbles were generally fewer and larger and persisted for only about 2.5 seconds.

With respect to the limits of s^0 discussed in Chapter 5, estimates for the upper limits of supersaturation possible in the tank experiments are 15.5 mbar (from $\rho g d_m / 2$) and 20 mbar (from $\rho g z_b$, z_b estimated at 20 cm). In the tank experiments the depth of the mixing layer probably determines the maximum possible degree of supersaturation since the full depth development of the plume is likely constrained by the bottom of the tank. Consequently an upper limit of supersaturation of 15.5 mbar is expected. Observed steady-state supersaturations were indeed less than the theoretical upper limit: s^0 values ranged from 2.3 to 12 mbars (lower column 6 in Table 6.4).

In my model it is clear that the potential supersaturation and the exchange velocity of the bubble population are determined by the source bubble population, i.e. the bubble distribution before dissolution and rise-out. In the laboratory experiments the depth of water limits the penetration of the source bubble population. The source population is assumed to be invariant given the means of production. So, even though each plume

evolves to some degree due to dissolution, undergoing the largest changes at saturations far from steady state, it is the arguably invariant source population that controls the potential supersaturation term in the driving force. Although the exchange velocity may change over the relatively short life-time of a plume, at the time of injection the exchange velocity will initially have the same value. Consequently, for a frequently injected plume, no measurable change in the exchange velocity is expected over the course of a single gas experiment due to the changing level of saturation of the water. A feedback between the driving force for gas exchange and the exchange velocity, as suggested by Woolf and Thorpe (1991) and described in Chapter 5, section 5.3.2, would appear in my experiments as a changing $\langle k_b \rangle$ with time. Since $\langle k_b \rangle$ is a large component of k' , especially in sea water, a changing $\langle k_b \rangle$ would be apparent as a departure from a straight line in time series of dP/dt versus $P - p$. The effect would be more pronounced for the more soluble gases, but was not clearly observed when such plots were generated for these experiments. A change in bubble dissolution rates has been observed in the laboratory (*Schulze and Schlünder, 1985*) and treated theoretically (*Davies, 1986*) as being the consequence of the changing mobility of the bubble surface due to collection of surface active materials. The effect has been shown to be significant for soluble gases resulting in exchange velocity enhancements by a factor of 3 for periods of several seconds. Again, the effect is apparently not significant in these experiments where the plume lifetime is short compared with the frequency with which the source population is injected.

The conclusion that the degree of supersaturation at steady state is largely controlled by the source bubble population is intuitively reasonable considering that it is the dissolution of bubbles at depth that sets the upper limit on the potential degree of supersaturation. Within the fresh water series there is some evidence that CO_2 , with the highest solubility, attains the highest steady-state supersaturation and He, with the lowest solubility, has the lowest Δ^0 . The supersaturations are however relatively small and the uncertainties correspondingly high. This result is consistent with my formulation where supersaturation is proportional to k_b/k' , and thus dependent on solubility through k_b , when the ratio is not near unity. This at first appears contrary to the predictions of conventional theory. However, when it is stated in the literature that the least soluble gas is expected to reach the highest supersaturations, e.g., (*Broecker and Peng, 1982*), it is in reference to *potential*

supersaturations as the result of dissolution, partial or complete, of *air* bubbles, whereas in these experiments the injected bubbles contain only the single gas of interest and water vapour. In sea water the results show no clear trend between solubility and Δ^0 , or between diffusivity and Δ^0 . the supersaturations being remarkably similar. Overall the results are consistent with the limits outlined above, i.e., that at high $\langle k_b \rangle$ to k ratios ($k_b/k' \rightarrow 1$), such as were found in sea water, the degree of supersaturation is controlled by z_b . Whereas, when $\langle k_b \rangle$ and k are comparable, as were found in fresh water, the degree of supersaturation is much more dependent on the ratio of $\langle k_b \rangle$ to k . When the degree of supersaturation becomes dependent on the exchange velocities it becomes dependent on the gas properties influencing the exchange velocities. The surface exchange velocity is dependent on gas diffusivity and independent of solubility while the bubble exchange velocity is dependent on both properties to some, as yet unknown, variable extent, depending on the bubble population.

6.6.2 k and $\langle k_b \rangle$

In general, the model appears to fairly consistently separate k' into components describing the surface and bubble exchange velocities. The ratio of k_b to k varies with the chosen value of z_b only slightly and approaches a constant value with large z_b . In a typical example, increasing z_b by 25% to 25cm increased k by 16% and decreased k_b by 6%. Decreasing z_b to 15cm, however reduced k by 32% and increased k_b by 10%.

While the combined exchange velocity is higher in sea water than in fresh water (average +35% for He, N₂, Ar and CO₂), the surface exchange velocity component is, as expected, lower in sea water compared with fresh water (for He, N₂ and Ar). Lower exchange velocities in sea water compared with fresh water are generally expected, as described in section 6.6.1. However, the magnitude of the difference (-86%) is larger than might be expected (-10%) based on viscosity and diffusivity arguments.

While $\langle k_b \rangle$ dominates the combined exchange velocity in sea water, it appears that k dominates k' in fresh water (except for CO₂). This supports the hypothesis that the bubble population in sea water is more effective in transporting gas than that in fresh water. Gat and Shatkey (1991) also found that bubbled brine solutions took up more gas, and at a faster rate, than predictions based simply on solubility and diffusivity corrections to results obtained in fresh water.

A clear relationship of k to D is expected, but is not resolved. The k values for He in each case were higher than the average value for all four gases, but were not the highest values determined. This is most likely the result of the model's limited ability to separate k from k' : although the model does reasonably well, some resolution is apparently lost. The difference in k 's in sea water from those in fresh water may also be due to the extent that different degrees of turbulence, due to the different behaviour of the entrained air, are present in sea water compared with in fresh water. Increasing degrees of turbulence should affect the exchange velocities of all gases equally.

In sea water the $\langle k_b \rangle$'s for CO₂, N₂ and Ar are all high and very similar and He has the highest value, following the corresponding trends in gas diffusivity. In fresh water CO₂ has the highest $\langle k_b \rangle$ and He has the lowest value, following the corresponding trends in gas solubility (although the values for He and N₂ are similar). It appears from the experimental results that solubility is a more important factor in determining $\langle k_b \rangle$ in fresh water compared with sea water. In Chapter 5, section 5.3.3, it was suggested that solubility was likely to have a greater influence on gas exchange velocities when bubble populations were relatively less efficient, such as in fresh water where there are fewer and larger bubbles. There is additional supporting experimental evidence from the literature. Asher et al. (1991) found little influence of solubility on exchange velocities in their whitecap simulation experiments in sea water. In contrast, Broecker and Siems (1984) did find an exchange velocity dependence on solubility in their fresh water wind-wave tank experiments. Also, as $\langle k_b \rangle$ for CO₂ is calculated to be just 40% less in fresh water compared with sea water, whereas $\langle k_b \rangle$'s for He and N₂ are 85% and 70% less respectively, Woolf and Thorpe's theory that the transfer of the more soluble gas is less sensitive to changes in the bubble population (*Woolf and Thorpe, 1991*) is also supported by my results.

6.7 Summary

1. The versatility of the GTD method is demonstrated in this chapter in a series of laboratory experiments using a variety of gases and conditions.
2. Differences in bubble populations produced by the intermittent waterfall in different media are found to have significant effects on gas invasion rates. Combined exchange

velocities and degrees of supersaturation are generally found to be higher in seawater conditions than in freshwater conditions.

3. The gas tension method is demonstrated to be able to measure gas exchange velocities of the order of those found in the field.
4. A depth-dependent bubble (DDB) flux model applied to the data gives useful insights into bubble-mediated gas exchange and helps to discern the role of bubble populations on gas-exchange rates and steady-state supersaturations. Conclusions related specifically to the DDB flux model are:
 - (a) Goodness of the model is demonstrated by the fact that the combined exchange velocity generally separates into consistent components. The surface exchange velocity, k , is lower in sea water compared with fresh water even while the combined exchange velocity, k' , is higher in sea water. Diffusivity and solubility arguments support the finding of lower k 's in sea water compared with fresh water. The photographically determined differences between the bubble populations in sea water and those in fresh water support the finding of higher k_b 's in sea water.
 - (b) The exponent n in $k' \propto D^n$ for He compared to N_2 is found to be lower than the 0.5 established for 'rough' surface regimes, in agreement with the observations of others in 'bubbly' regimes.
 - (c) In fresh water, surface and bubble exchange velocities are quite similar. In sea water, with high uncertainties, $k < \langle k_b \rangle$. Again, this result is interpreted in terms of the different efficiencies of the bubble populations in sea water compared with those in fresh water.
 - (d) The CO_2 results are remarkably similar in fresh water and sea water and are explained in terms of the transport of a more soluble gas being less sensitive to changes in bubble populations.
 - (e) It was found, in agreement with the model predictions, that steady-state supersaturations become independent of gas properties and more dependent on the depth distribution of the bubble population when bubble exchange velocities are a large component of the combined exchange velocities.

- (f) Bubble exchange velocities, and consequently steady-state supersaturations, are suggested to become more sensitive to solubility when bubble populations are less efficient through having fewer and larger bubbles.

Chapter 7

Discussion and Conclusions

7.1 Introduction

While the gas tension method is discussed in both Chapters 4 and 6, there are topics that require further consideration. These topics fall under the general heading of errors and include temperature and humidity effects. Difficulties specific to the laboratory set-up are summarized here and solutions suggested. Suggestions for further work follow, including the development and application of a field instrument. Finally, conclusions are presented.

7.2 Temperature and Related Effects

The effects of a temperature difference between water and the overlying gas on inter-phase gas exchange are now considered. Also, the effect of a temperature difference between one experiment and the next is calculated. The level of temperature control achieved is very good, at better than 0.5°C between experiments (Table 6.2) and better than 0.3°C between phases (Table 6.1).

7.2.1 Solubility

Gas solubilities and diffusivities in water are temperature dependent. Nitrogen solubility is reduced by 1.7% per degree Celsius temperature increase around 20°C . The temperature dependence of helium's solubility is minimal at $0.18\%^{\circ}\text{C}^{-1}$, for argon it is $1.8\%^{\circ}\text{C}^{-1}$. Calculations are based on the data of Weiss (1970; 1971). At higher temperatures then, the

gas content of the water at equilibrium with the overlying atmosphere is smaller. In an invasion experiment into relatively warm water the driving force for gas transfer is reduced and consequently the flux is also reduced. Phillips (1991) argues that the driving force may be lower still for gases with large heats of solution, because the driving force in partial pressure terms is only a limiting case of the more complete thermodynamic driving force in terms of the difference in chemical potential between phases. Consideration of the chemical potential difference between phases links the gas flux to the heat flux via the heat of solution of the gas. Carbon dioxide has a large heat of solution, a property that Phillips suggests may help to reconcile estimates of the global uptake of CO_2 by the ocean when taken into consideration along with air-water temperature differences at the sea surface,

However, while the driving force for gas transfer is reduced, the gas exchange velocity is unchanged by solubility effects in most cases. An exception arises when bubbles are an additional mechanism for gas transfer (*Broecker and Siems, 1984*). There may also be air-water temperature difference effects on the bubble populations themselves (*Hwang et al., 1991; Thorpe et al., 1992*) with consequences for gas-exchange rates.

The advantage of the gas tension method over other techniques is that the gas pressure difference across the gas-water interface is measured directly. In contrast, other methods calculate a gas-exchange driving force from the difference between a discrete concentration measurement and an estimated equilibrium concentration. The equilibrium concentration is a calculated estimate that incorporates observed temperature and, in theory, but not always in practice, ambient atmospheric pressure. Potential problems arise when air-water temperature differences exist and, more significantly for the role of bubbles, with the assumption that the final steady state is in fact an equilibrium condition.

7.2.2 Diffusivity

Gas diffusivities in water also increase with increasing temperature. However diffusivities are not well known (10% at best) and different temperature dependencies are reported in the literature, partly as a consequence. *Jähne et al. (1987a)* report a range of diffusivity dependencies for the noble gases from $1.6\%^\circ\text{C}^{-1}$ for He to $3.3\%^\circ\text{C}^{-1}$ for Rn. According to the empirical formula of *Hayduk and Laudic (1974)*, the temperature effect on diffusivity, via changes in water viscosity amounts to $3.4\%^\circ\text{C}^{-1}$ around 20°C for all gases. In the surface

renewal model of gas transfer, appropriate for gas exchange under rough surface conditions, $k \propto D^{\frac{1}{2}}$. Temperature differences between repeat experiments could cause differences in k of the order of $3.4/2 = 1.7\%$ per degree Celcius. Temperature differences between experiments have been at most 0.5°C (Table 6.2), making this a small effect at less than 0.9%.

7.2.3 Pressure

The pressure controller should compensate for any temperature-induced pressure changes as its rated sensitivity is 0.3 mbar.

7.2.4 Humidity

Changes in gas-phase temperature are likely larger and faster than those in the bulk water. This means that small temperature differences between the gas and the bulk water can exist over extended periods. These conditions, while likely in the field, are not a concern in the laboratory experiments where the temperature was controlled at room temperature. This leads to consideration of the effect of water-vapour pressures since water-vapour pressure is a well-known function of temperature and, to a lesser extent, salinity. We assume that the partial pressure of water is the same in both phases, i.e. the gas phase is at 100% humidity so $p_{H_2O} = P_{H_2O}$, and the terms cancel out in the measurement of $P - p$. Both gas phase and water phase will indeed be 100% saturated with water vapour close to the interface, but the gas-phase pressure and humidity measurements are made somewhat remote from the interface. However, since the total pressure must be the same throughout the experimental tank, the total pressure measured by the barograph must equal the total pressure above the main water reservoir, even as the humidity is lower in the bell jar. As a reference for the relative contribution of water vapour pressure to the gas-phase pressure, at 22.8°C saturated vapour pressure is 27.5 mbar over fresh water, and slightly less, 27.0 mbar over sea water (formula of Green and Carritt (1967)).

7.3 Suggestions for Further Work

A number of difficulties with the current experimental apparatus would be resolved by investing in readily available hardware. The suggested improvements would improve the

precision of the method and greatly expand the range of experiments that might be carried out in the laboratory.

7.3.1 Hardware improvements

In the current system, as discussed in Chapters 4 and 6, the upper limit on gas-phase pressure was about 1040 mbar — the maximum measurable on the barograph. This pressure was controlled relative to atmospheric pressure by the Cartesian-diver controller and was poorly measured by the barograph due to 1) poor resolution in both time and pressure, and 2) the pen having a tendency to stick. The method was also tedious and error-prone: the bell-jar containing the barograph was susceptible to leaks and had to be opened in order to change the chart paper every 3 days; and the data had to be read from the charts and manually transferred to computer files. A digital pressure gauge with its sensor in the main tank and its output direct to a data logger synchronously collecting GTD output would be an obvious improvement. More expensive, a strong gas-tight tank could be used. Then gas pressures might be controlled absolutely to remove the influence of ambient atmospheric changes and allow long time-scale experiments to be carried out reproducibly. In the current system evasion experiments were difficult to carry out because, as mentioned, a large driving force for evasion could not be reliably produced, being limited by how much the water could be supersaturated by a prior invasion experiment compared with how low the ambient atmospheric pressure would remain. In addition, under low gas-phase pressures the hydrostatic pressure was barely sufficient to hold the membrane up against its support, being comparable in size, or less than, gas tension. Increasing depth of water above the GTD would mitigate this problem and indeed the water depth was increased during this series of experiments as this effect was discovered. This condition, equivalent to $P - p$ being greater than $\rho g d_m$, is also conducive to bubble nucleation. Bubbles nucleating on the membrane surface may also have interfered with the signal — unfortunately it was not possible to look directly at the membrane when it was in operating position. Bubble nucleation on acoustic current sensors has been found to be inhibited by a coating of anti-fog solution (A. J. Williams III, pers. comm.) or dishwashing detergent (T. Kelly, pers. comm.). These coatings may interfere with the gas permeability of the membrane, although the membrane certainly did accumulate a slimy coating after weeks of use anyway. Better control over the

volume/frequency of the bucket dumps would also be desirable and might be achieved by mechanization of the process.

The current system easily resolved differences in gas invasion rates with bubble injection between fresh water and sea water. An improved system would better resolve differences between different gases to more fully test the DDB flux model and Sc dependencies. It would certainly be desirable to compare evasion rates with invasion rates for different gases between fresh water and sea water with bubble injection. As Figure 7.1 illustrates, while the driving force for the equilibrium flux may be the same for invasion as evasion, the bubble flux driving force may not only be of different magnitude, but may also be in the opposite direction. Note that steady state is reached in the illustrated example when gas tension reaches a value such that the vectors for driving force, when multiplied by their corresponding exchange velocities, are equal in magnitude and opposite in sign for the equilibrium flux and the bubble flux. The consequences of any asymmetry between invasion and evasion processes is that typical gas flux studies following just the evasion of a tracer gas will not predict such high invasion fluxes, as for example observed by Wallace and Wirrick (1992). The asymmetry referred to in bubble gas fluxes, because it arises in the driving force term, is not expected to affect bubble exchange velocities. Exchange velocities and time constants are theoretically symmetrical between invasion and evasion, but absolute time required to reach steady state may not be the same in both cases; 'rate' can be an ambiguous term when used without qualification. Further laboratory experiments are needed to either confirm the basic theory, or show the significance of feedback between driving force terms and exchange velocity terms in the presence of bubbles.

There are many other phenomena that might be investigated using the gas tension method in further laboratory studies. These could include studies on the presence of surfactants, natural organic materials, and particles on gas exchange. Temperature effects, especially air-water temperature differences in the presence of bubble injection, and the coincident fluxes of heat and water vapour need further study.

7.3.2 Field instrument

A basic field instrument requires few adaptations from the laboratory GTD. Gas tension and gas-phase pressure would be measured absolutely, rather than differentially because it

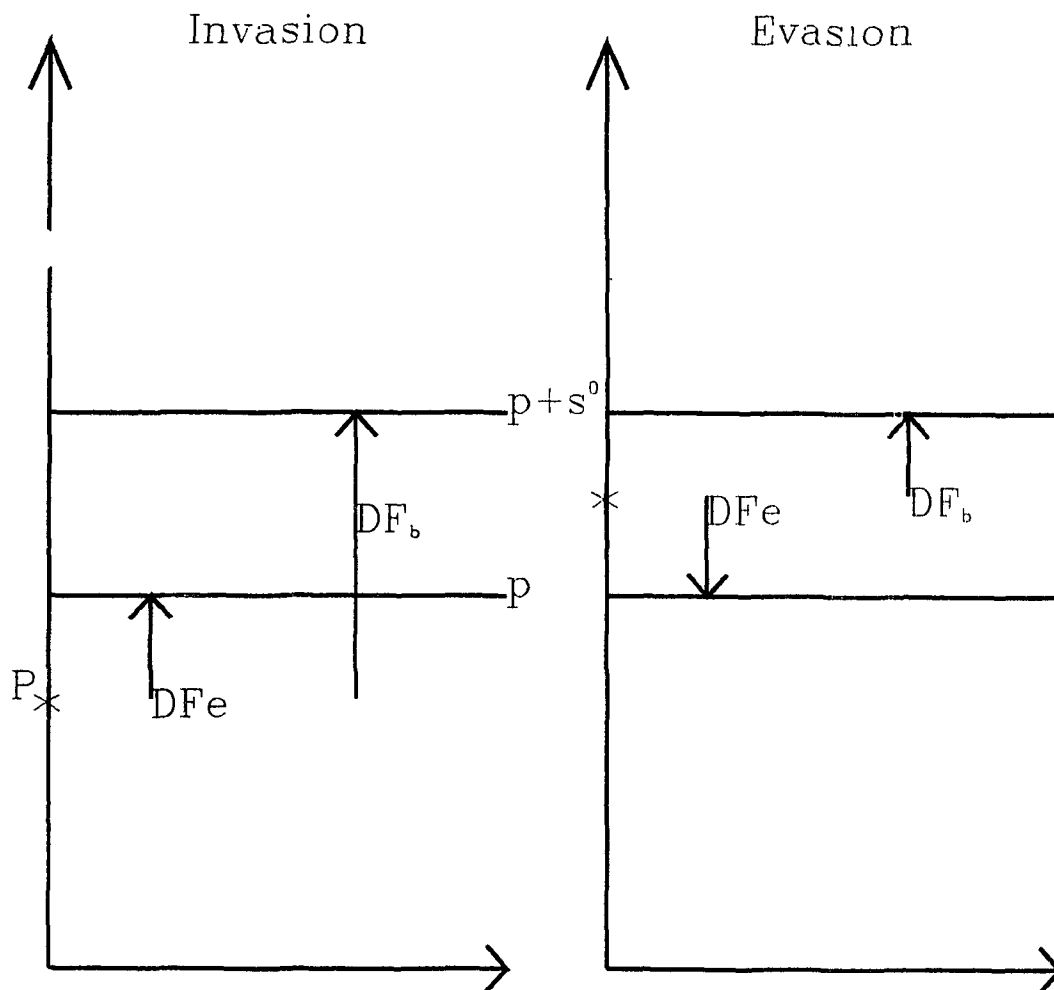


Figure 7.1: Driving forces for classic invasion and evasion scenarios. Conditions supporting supersaturation are the same in each case. The initial gas tension is chosen such that the magnitude of the equilibrium driving force, DF_e , the difference between the gas tension, P , and gas-phase pressure, p , is equal in each case. Clearly the 'bubble' driving force, DF_b is of different magnitude in each case, and not necessarily in the same direction. A steady state is reached when the equilibrium and bubble fluxes, the driving forces multiplied by the relevant exchange velocities, are of equal magnitude and oppositely directed.

is impractical to run a connecting tube to the surface. An alternative measurement of sensor drift would be required. A stirrer and a data logger would also be built in. An obvious question is how to then interpret total dissolved gas pressure in terms of the individual gases of interest. Total gas tension is very nearly the sum of the partial pressures of N_2 , O_2 and water vapour. Dissolved oxygen is readily measurable by in situ polarographic probes and, assuming 100% water vapour saturation, 96.9% of the remaining gas tension signal is due to N_2 . Nitrogen is essentially inert and is a useful starting point for modelling the response of other gases to physical processes, such as storm events. Solid-state oxygen detectors have been developed in industry for monitoring engine exhaust composition and may prove to be suitable for incorporation into the GTD. Other non-destructive gas analysis methods might also be considered for analysing the gas composition in the sensing volume of the GTD.

Total dissolved gas pressure is of interest to riverine fisheries (*D'Aoust et al.*, 1975; *D'Aoust and Clark*, 1980). Total dissolved gas meters have been developed to monitor levels of saturation downstream from power plant outfalls to determine the degree of intervention required to return the waters to safe gas levels. These meters use the same principle of equilibrating a small sampling volume via a gas permeable membrane and comparing the pressure directly with the overlying gas-phase pressure. Perhaps fortunately, we were unaware of these meters and developed our device independently and with design features that address the concerns of rapid response time, minimal hydrostatic pressure response and a check on sensor drift, that are particularly relevant to gas-exchange rate experiments.

7.4 Conclusions

Bubble population measurements made by a photographic method illustrated large differences between bubble populations in a seawater plume and a freshwater plume of the same genesis. While the results were not quantitative for small ($< 200\mu\text{m}$) diameter bubbles, they were generally consistent with other literature results. The seawater plume had many more, and smaller, bubbles than the freshwater plume. The numbers of bubbles were consistent with an exponentially decreasing function with depth. The intermittent waterfall was demonstrated to provide a convenient bubble-injection method suited to gas-exchange studies.

Total dissolved gas pressure, gas tension, is a valuable new fundamental measurement

in gas-exchange rate studies. The gas tension method, where time series of gas tension are used to follow the rate of equilibration of a water parcel in response to gas-phase pressure changes, is suited for use in energetic conditions where gas fluxes are large and rapid. Advantages of the gas tension method include the following items that are listed along with some of their implications:

1. Gas tension is a physical, rather than a chemical measurement of gas content.
 - (a) The gas tension measurement is not gas specific, allowing single-gas experiments to be compared with gases covering a wide range of properties.
 - (b) Gas is not consumed in the measurement, allowing continuous in situ measurements to be made without concern for depleting the gas content of the water.
2. Measurement of gas tension is made in situ and continuously.
 - (a) The delicate handling required of gas samples is avoided.
 - (b) A closed, and therefore potentially well-controlled, experimental tank can be used.
 - (c) Sensitivity to environmental variables is more easily apparent when all variables, including gas tension, may be monitored continuously.
3. The gas tension device measurement of differential pressure is very sensitive, due to the inherent sensitivity of the pressure sensor. The precision of the overall method, including explicit evaluation of gas tension, is also potentially high, given the discussion of available hardware improvements.
 - (a) Fluxes, in either invasion or evasion situations, can be measured.
 - (b) Fluxes of the order of magnitude of fluxes in the field are measurable.
4. The degree of saturation of the water is measured directly.
 - (a) The results are never biased due to an assumption about the steady-state degree of saturation.
 - (b) The method is ideally suited to investigating bubble-mediated gas transfer, for which gas supersaturations are diagnostic.

- The experimental results of this thesis support the conclusion that small bubbles significantly contribute to bubble-mediated gas flux, in support of the observations and theory of other investigators.
- Further, gas solubility is concluded to be a less important contributing factor to gas exchange velocities when bubble injection is efficient (many small bubbles), and relatively more important as bubble injection becomes less efficient (fewer and larger bubbles).
- The results support the theoretical conclusion that the steady-state supersaturation becomes less dependent on gas properties and more dependent on the depth distribution of the bubble population when bubble injection is efficient.
- Conversely, when bubble injection is less efficient, the degree of steady-state supersaturation is concluded to become more dependent on the gas properties, and in particular to become more dependent on gas solubility.

The model developed as a tool for analysing the gas-exchange data, by isolating the bubble-flux from the total gas flux, aided arrival at these conclusions. The experiments were carried out using single gases and the results suggest that further experiments with simple gas mixtures might be informative, leading to a better understanding of how injected bubbles of air behave.

A gas tension device for field studies of gas exchange requires only peripheral modifications of the prototype used in the laboratory. As a water-phase analog for barometric pressure, the gas tension signal in the field will provide net gas content response to changing environmental conditions. Gas tension response during storm events, especially as a function of depth, would be a particularly interesting and relevant study. The challenge in field measurements of gas tension will be to interpret the total dissolved pressure signal in terms of the contributing gases. Further laboratory studies using the gas tension device will contribute to the modelling efforts. In addition, existing bubble-mediated gas exchange models require further data to test them, data that has previously been sparse due to dynamic limitations of other methods, but can now be provided by the gas tension method.

Appendix A

Pressure Sensor Calibration

The calibration was carried out by manually applying small pressure increments to the sensor port of the differential pressure sensor using a syringe and recording the voltage of the sensor as amplified by the electronics package. The applied pressure was measured from the movement of a slug of water in a simple laboratory-assembled manometer. The arrangement is illustrated in Figure A.1. The calibration was carried out over about 10 minutes during which time atmospheric pressure and temperature changes were not considered to be varying significantly. Manometer dimensions: tube i.d. $3.36 \pm .02$ mm, o.d. $5.89 \pm .02$ mm, glass thickness $2.53 \pm .02$ mm, bulb volume 41.87 cm³ (2%, est.) and tube cross-section, A , 8.87×10^{-2} cm² (1%). The slope of sensor voltage versus manometer fluid position was recorded on two separate occasions at 0.443 V cm⁻¹ (Figure A.2) and 0.445 V cm⁻¹. The result was highly linear over the measured range of interest from approximately -3 to +6 V.

The voltage change per unit pressure change, dV/dp , is calculated by first calculating the pressure increment per centimeter movement of manometer fluid, dp/dx . The initial fluid position, at a barometric pressure of 1016.0 ± 0.05 mbar, was $x=15.85$ cm (0.3%). The total gas volume enclosed in the manometer by the slug of fluid, V , is the volume of gas in the tube (8.87×10^{-2} cm² \times 15.85 cm) plus the volume in the attached manometer bulb (41.87 cm³) For small pressure changes, $dp/dV \approx p/V$, and therefore

$$\begin{aligned} dp/dx &\approx A \times p/V \\ &= 2.08 \text{ mbar cm}^{-1}. \end{aligned}$$

Consequently, the voltage change per unit pressure change,

$$\begin{aligned}dV/dp &= (dV/dx)/(dp/dx) \\ &= (-0.444 \text{ V mbar}^{-1})/(2.08 \text{ mbar cm}^{-1}) \\ &= -0.213 \text{ V mbar}^{-1}.\end{aligned}$$

The voltage to pressure ratio is given the symbol r . The uncertainty in r is of order 3% and arises principally in the dp/dx term due to the difficulty in accurately measuring the volume of the manometer bulb. For most cases it is sufficient to have demonstrated that the response is highly linear because the actual value of the ratio frequently drops out of calculations.

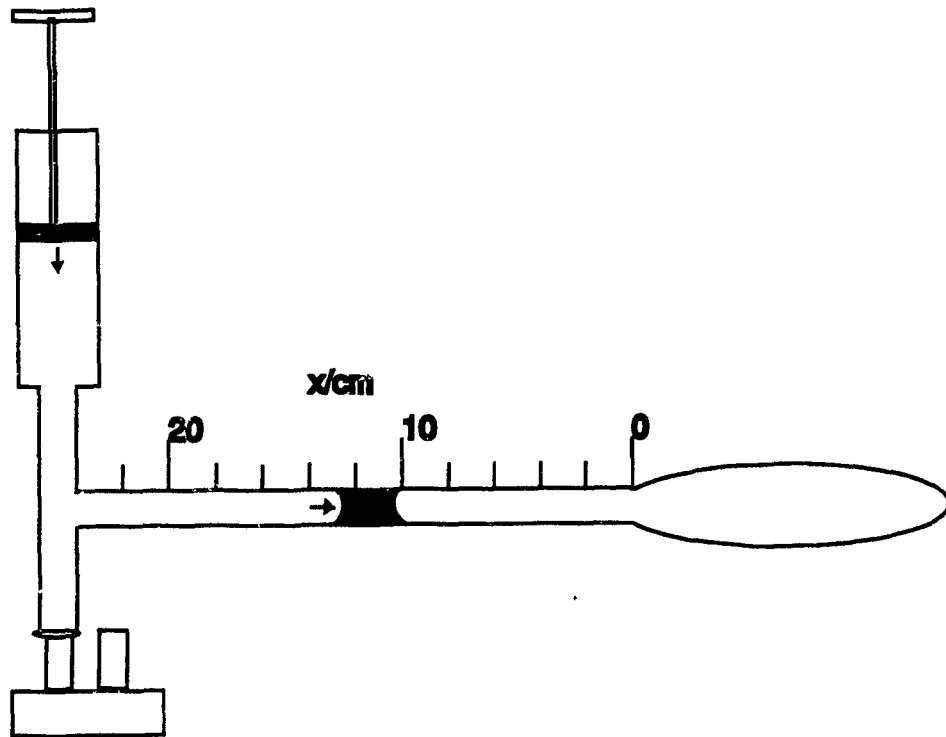


Figure A.1: Calibration apparatus: a simple manometer arrangement measured the pressure applied in the calibration exercise. Dimensions of the manometer are used to calculate the pressure change per centimeter movement of manometer fluid.

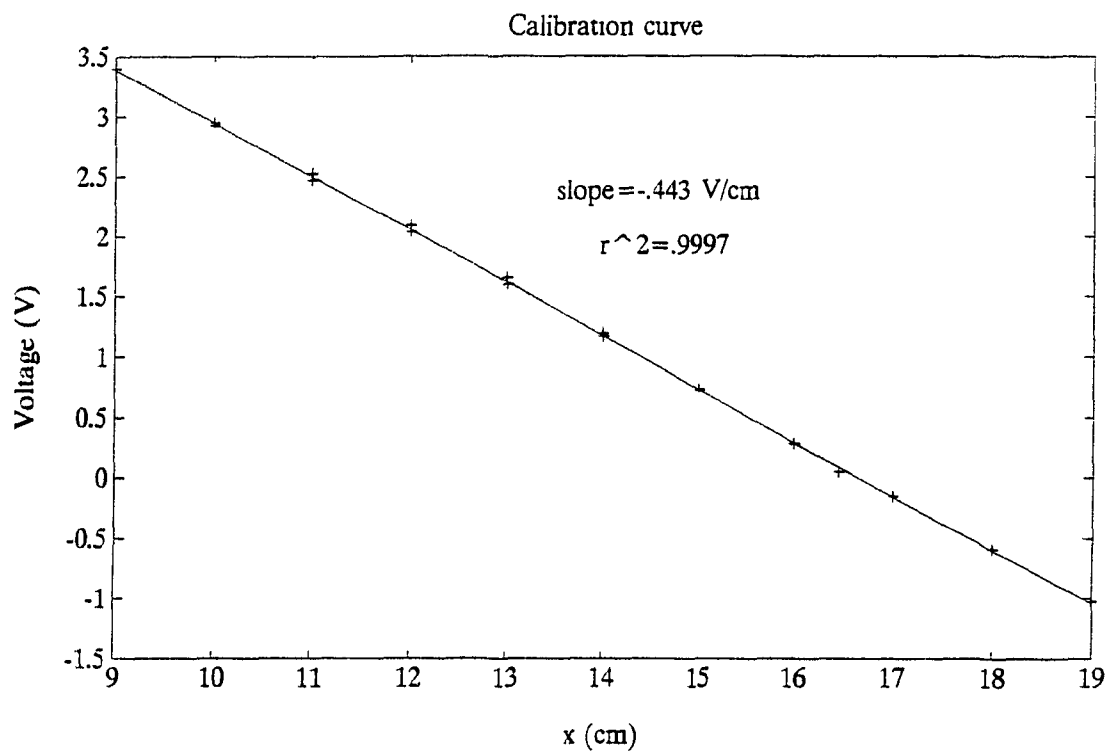


Figure A.2: Calibration curve of pressure sensor output voltage versus manometer fluid position.

Appendix B

Calculations

Similar integrals occur several times in the depth-dependent bubble flux model. Solution details and a review of the abbreviations used are given here.

Depth-averaged bubble flux

Tables of integrals give the following general solutions:

$$\int e^{ax} \partial x = \frac{e^{ax}}{a} \quad (\text{B.1})$$

$$\int x e^{ax} \partial x = \frac{e^{ax}}{a} \left(x - \frac{1}{a} \right) \quad (\text{B.2})$$

$$\int x^n e^{ax} \partial x = \frac{e^{ax}}{a} \left(x^n - \frac{nx^{n-1}}{a} + \frac{n(n-1)x^{n-2}}{a^2} - \dots - \frac{(-1)^n n!}{a^n} \right). \quad (\text{B.3})$$

From general solution B.1 it follows that the depth-averaged value of $e^{-\frac{z}{z_b}}$ between the surface and depth d_m is

$$\begin{aligned} \frac{1}{d_m} \int_0^{d_m} e^{-\frac{z}{z_b}} \partial z &= -\frac{z_b}{d_m} \left[e^{-\frac{z}{z_b}} \right]_0^{d_m} \\ &= -\frac{z_b}{d_m} \left[e^{-\frac{d_m}{z_b}} - 1 \right] \\ &= I \left(1 - e^{-\frac{1}{I}} \right) \\ &= c_1 \end{aligned}$$

where

$$I = \frac{z_b}{d_m}$$

Thus, to repeat, equations 5.10 and 5.9. From the above result it follows that, given

$$k_b(z) = k_{b0} e^{-\frac{z}{z_b}}, \quad (\text{B.4})$$

(equation 5.7) that the depth-averaged value of k_b over a mixing-layer depth d_m is

$$\begin{aligned} \langle k_b \rangle &= \frac{1}{d_m} \int_0^{d_m} k_{b0} e^{-\frac{z}{z_b}} \partial z \\ &= c_1 k_{b0} \end{aligned}$$

(equation 5.8).

The solution to the depth-averaged value of $\int z e^{-\frac{z}{z_b}} \partial z$ over $z = 0$ to $z = d_m$ is found by substituting the relevant variables in general solution B.2 and evaluating over the specified range.

$$\begin{aligned} \frac{1}{d_m} \int_0^{d_m} z e^{-\frac{z}{z_b}} \partial z &= -\frac{z_b}{d_m} \left[e^{-\frac{d_m}{z_b}} (z + z_b) \right]_0^{d_m} \\ &= -\frac{z_b}{d_m} \left(\left[e^{-\frac{d_m}{z_b}} (d_m + z_b) \right] - [z_b] \right) \\ &= I \left(z_b \left(1 - e^{-\frac{1}{I}} \right) - d_m e^{-\frac{1}{I}} \right) \\ &= d_m I \left(c_1 - e^{-\frac{1}{I}} \right) \\ &= d_m c_2 \end{aligned} \quad (\text{B.5})$$

$$\text{where (equation 5.12)} \quad c_2 = I(c_1 - e^{-\frac{1}{I}}).$$

Note that c_1 and c_2 are functions only of z_b and d_m . The bubble flux at depth z is given by (equation 5.6)

$$F_b(z) = -\frac{k_b(z)}{H} (P - (p + \rho g z)) \quad (\text{B.6})$$

and the average value between the surface and depth d_m (using the solutions obtained above) is

$$\begin{aligned} \langle F_b \rangle &= -\frac{1}{d_m} \int_0^{d_m} k_{b0} e^{-\frac{z}{z_b}} \frac{1}{H} (P - (p + \rho g z)) \partial z \\ &= -\frac{k_{b0}}{H} \frac{1}{d_m} \int_0^{d_m} e^{-\frac{z}{z_b}} (P - p) \partial z + \frac{k_{b0} \rho g}{H} \frac{1}{d_m} \int_0^{d_m} z e^{-\frac{z}{z_b}} \partial z \\ &= \frac{\langle k_b \rangle}{H} (\langle P \rangle - p) + \frac{\langle k_b \rangle c_2}{H c_1} \rho g d_m \end{aligned} \quad (\text{B.7})$$

(equation 5.11).

Gas tension time series

To obtain $P(t)$ the inhomogeneous partial differential equation,

$$\frac{\partial P}{\partial t} = -\frac{k'}{d_m}(P - p) + \langle k_b \rangle \rho g c_2 / c_1$$

must be first be arranged in a form convenient for solution, i.e.,

$$\frac{\partial P}{\partial t} + \frac{k'}{d_m}P = \frac{k'}{d_m}p + \langle k_b \rangle \rho g c_2 / c_1. \quad (\text{B.8})$$

A solution to such an expression, i.e.,

$$\frac{\partial P}{\partial t} + aP = f(t) \quad (\text{B.9})$$

is obtained by multiplying both sides by an 'integrating factor' $\mu(t)$, that allows equation B.9 to be rewritten as

$$\frac{\partial}{\partial t}(\mu(t)P) = \mu(t)f(t) \quad (\text{B.10})$$

which can be integrated with relative ease. The integrating factor is

$$\begin{aligned} \mu(t) &= e^{\int a \partial t} \\ &= e^{at} \end{aligned}$$

for this case where expression a is not a function of time. The solution for $P(t)$ is then

$$P = e^{-at} \int e^{at} f(t) \partial t. \quad (\text{B.11})$$

i) Constant p

In the case where p is constant, function f is no longer a function of time and the solution is

$$\begin{aligned} P &= e^{-at}(f/ae^{at} + d) \\ &= f/a + de^{-at} \end{aligned}$$

where d is a constant of integration and is determined from the initial condition $P = P_0$ at $t = 0$. Consequently the solution is

$$\begin{aligned} P &= f/a + (P_0 - f/a)e^{-at} \\ &= f/a(1 - e^{-at}) + P_0e^{-at} \end{aligned}$$

which becomes

$$P = \left(p + \rho g d_m \frac{\langle k_b \rangle c_2}{k' c_1} \right) (1 - e^{-\frac{k'}{d_m} t}) + P_0 e^{-\frac{k'}{d_m} t} \quad (\text{B.12})$$

(equation 5.15) on substitution of the relevant expressions for a and f .

Varying p

When gas-phase pressure is not constant, integral B.11 is more complicated. In the gas-exchange experiments a cubic expression fits most of the observed variability in p , (equation 5.19)

$$p = ht^3 + lt^2 + mt + n.$$

So $f(t)$ in equation B.8 becomes, with simplification,

$$\begin{aligned} f &= \frac{k'}{d_m} (ht^3 + lt^2 + mt + n) + \langle k_b \rangle \rho g c_2 / c_1 \\ &= a(ht^3 + lt^2 + mt + n) + b. \end{aligned} \quad (\text{B.13})$$

By substitution of expression B.13 in equation B.11

$$P = e^{-at} \int e^{at} (a(ht^3 + lt^2 + mt + n) + b) \partial t, \quad (\text{B.14})$$

and the component integrals can be separated and solved.

$$\begin{aligned} P &= e^{-at} \int e^{at} (a(ht^3 + lt^2 + mt + n) + b) \partial t \\ &= e^{-at} (ah \int t^3 e^{at} \partial t + al \int t^2 e^{at} \partial t + am \int t e^{at} \partial t + (an + b) \int e^{at} \partial t) \\ &= +h \left(t^3 - \frac{3}{a} t^2 + \frac{6}{a^2} t - \frac{6}{a^3} \right) \\ &\quad +l \left(t^2 - \frac{2}{a} t + \frac{2}{a^2} \right) \\ &\quad +m \left(t - \frac{1}{a} \right) \\ &\quad +n + \frac{b}{a} + d e^{-at}. \end{aligned}$$

Again, d is a constant of integration that is solved using initial conditions $P = P_0$ at $t = 0$,

$$d = P_0 - n - \left(\frac{b}{a} + \frac{m}{a} - \frac{2l}{a^2} + \frac{6h}{a^3} \right).$$

Rearranging terms gives

$$\begin{aligned}
 P &= ht^3 + lt^2 + mt + n - ne^{-at} \\
 &\quad - ((3ht^2 + 2lt + m) - me^{-at})/a \\
 &\quad + ((6ht + 2l) - 2le^{-at})/a^2 \\
 &\quad - (6h - 6he^{-at})/a^3 \\
 &\quad + b(1 - e^{-at})/a \\
 &\quad + P_0e^{-at}
 \end{aligned}$$

which is recognized as

$$\begin{aligned}
 P &= \left(p - \frac{1}{a} \frac{\partial p}{\partial t} + \frac{1}{a^2} \frac{\partial^2 p}{\partial t^2} - \frac{1}{a^3} \frac{\partial^3 p}{\partial t^3} + \frac{b}{a} \right) \\
 &\quad - \left(p(0) - \frac{1}{a} \frac{\partial p(0)}{\partial t} + \frac{1}{a^2} \frac{\partial^2 p(0)}{\partial t^2} - \frac{1}{a^3} \frac{\partial^3 p(0)}{\partial t^3} + \frac{b}{a} - P_0 \right) e^{-at}. \quad (\text{B.15})
 \end{aligned}$$

Examination of equation B.15 shows that, as required, $P \rightarrow P_0$ as $t \rightarrow 0$. When $t \rightarrow \infty$, the exponential term tends to zero and P tends towards a value determined by p , derivatives of p , and a constant value b/a . When p is constant the solution agrees with equation B.12.

Expansion, by replacing a and b , with their full expressions gives

$$\begin{aligned}
 P &= \left(p - \frac{d_m}{k'} \frac{\partial p}{\partial t} + \left(\frac{d_m}{k'} \right)^2 \frac{\partial^2 p}{\partial t^2} - \left(\frac{d_m}{k'} \right)^3 \frac{\partial^3 p}{\partial t^3} + \rho g d_m \frac{\langle k_b \rangle c_2}{k' c_1} \right) \\
 &\quad - \left(p(0) - \frac{d_m}{k'} \frac{\partial p(0)}{\partial t} + \left(\frac{d_m}{k'} \right)^2 \frac{\partial^2 p(0)}{\partial t^2} - \left(\frac{d_m}{k'} \right)^3 \frac{\partial^3 p(0)}{\partial t^3} + \rho g d_m \frac{\langle k_b \rangle c_2}{k' c_1} \right) e^{-\frac{k'}{d_m} t} \\
 &\quad + P_0 e^{-\frac{k'}{d_m} t}
 \end{aligned}$$

Appendix C

Data Analysis Routines

fitp.m

```
% function [run, Nr, tr, pr, Pr, ti, pri, Nt, tt, cf, perr, mp]=fitp
% M. Anderson, Feb 1993; last edit 1 Mar 1993
% function file to 1) generate P and p from raw gas-exchange exptal data
% and select working subsets of data, 2) fit cubic to p
% 3) generate a time scale for uniform subsampling
% Input: interactive for data file to load
% Output: cf=[k,l,m,n],      : cubic ycf=kt^3+lt^2+mt+n,
%      tr,tri,pr,pri,Pr,Pri : working subsets of raw data,
%      i, ti,      : i=start index, ti=t(i),
% tt, dt1, dt2      : sampling time scale and 2 intervals used
% mp      : mean pressure from cubic fit over tt
% Nr, Nt      : no. of data points in raw and subsampled fit
%      perr      : mean square error in fit to pr, (Nr points)
% Some vars saved to files for reference, others output for immediate use.
% Note: uncomment lines 60,61,62,67 to activate saving results to files
% Plots saved in fpti42j.met, data to fpti42j.mat, .dat etc,
function [run, Nr, tr, pr, Pr, ti, pri, Nt, tt, cf, perr, mp,nm]=fitp
% Calculate P from raw data using function 'fgetp'
clear % clear workspace
fname=input('File to load? ','s');
eval(['load ',fname]);
[P,DPp]=fgetp(t,V,p,V0);
```

```

%
% Find indices for subset of data using function 'subset'
% where first point related to dp/dt, last is max of 400min.
[i,j]=subset(t,p) % i= index of first pt, j=index of last point
it=input('or enter new value for i (0 to use given value) - ');
if it==0 else i=it; end
jt=input('or enter new value for j (0 to use given value) - ');
if jt==0 else j=jt; end
%
% Create reduced time series for analysis and reset tr(1)=0.
tri=t(1:j); % raw data cut off at max of 400 min
pri=p(1:j); % raw data cut off at max of 400 min
Pri=P(1:j); % raw data cut off at max of 400 min
ti=t(i); % time at start of analysis
tr=t(i:j); % raw data cut at both ends
tr=tr-tr(1); % reset tr(1)=0 from ti
pr=p(i:j); % raw data cut at both ends
Pr=P(i:j); % raw data cut at both ends
Nr=length(tr); % number of point in subset used in analysis
%
% Generate tt, times to subsample functions
% function 'interval' to clc average over first 60 min and remainder
[dt1,dt2,maxt]=interval(tr);
tt=[0:dt1:60, 60+dt2:dt2:maxt];
Nt=length(tt);
%
% cubic fit to p, ycf=ht^3+lt^2+mt+n using raw sampling density
cf=polyfit(tr,pr,3); % returns coeffs cf=[h,l,m,n]
ycf=polyval(cf,tt); % 'y' values
mp=mean(ycf); % mean gas-phase pressure over tt
% yct=polyval(cf,tr);
%
% Plot output
perr=fitplt(run,tr,tri,pr,pri,Pri,tt,cf,ti,Nr);
% Save output

```

```

l1=length(run)-1;
l2=length(run);
tis=num2str(ti);
js=num2str(j);
nm=[tis run(l1:l2) js];
mm=['fp' nm];
ltri=length(tri);
% length of each i,ti,dt1,dt2,mp,Nr,perr = 1, length of cf=4,
eval(['delete ',mm,'.met; meta ',mm]); % uncomment to activate
eval(['copy ',mm,'.met c:\mah\plots']); % copy to print dir
eval(['save ',mm,'.mat run cf mp i ti Nr perr tri dt1 dt2 Nt tt']);
disp(['output saved in ',mm, '.met, .mat; plots copied to print dir']);
eval(['save ',mm,'.dat /ascii ti perr Nr tr
ltri tri pri Pri Nt tt ycf']);
disp(['output saved in ',mm, '.dat']);
% n.b. .dat file contains only data needed to replot
clg;

```

fgetp.m

```

% function [P,DPp]=fgetp(t,V,p,V0);
% M. Anderson, 1992; last edit 1992
% Routine to calculate P and DPp from raw gas exchange exptal data.
% Simple but ensures all mfiles use same relationship.
% (Enter constants in this function)
% Data file must contain t, V, p and V0
% (GTD voltage, gas-phase pressure at times t, also offset voltage.)
%  $V=r(P-p+hp)+V0$ ;
function [P,DPp]=fgetp(t,V,p,V0);
hp=0; % hydrostatic pressure function.
r=.213; % voltage to pressure calib. ratio
DPp=((V-V0)/r)-hp; % differential pressure, P-p
P=((V-V0)/r)+p-hp; % gas tension
% end fgetp

```

subset.m

```

% function [i,j]=subset(t,p);

```

```

% M. Anderson, 1993; last edit 23 Feb 1993
% function file to return indices of t, p where
% i is the index where dp/dt is first <=0
% j is the index where t(j) is minimum of 400 min or entire series
function [i,j]=subset(t,p);
dpdt=diff(p)./diff(t);
i=min(find(dpdt<=0.1));
if t(length(t))<400;
    j=length(t);
else j=max(find(t<=400));
end;

```

interval.m

```

% function [dt1,dt2,maxt]=interval(tr),
% M. Anderson, 1993; last edit 24 Feb 1993
% function to break up tr after 60 min
% and estimate average sampling interval in each section
function [dt1,dt2,maxt]=interval(tr);
maxt=10*ceil(tr(length(tr))/10);
i=max(find(tr<=60));
t1=tr(1:i);
% diff(t) = vector of values t(n+1)-t(n);
dt1=round(sum(diff(t1))/(length(t1)-1));
t2=tr(i:length(tr));
dt2=round(sum(diff(t2))/(length(t2)-1));

```

opt20.m

```

% function [acmse,ad,cd]=opt20(run,tt,tr,pr,cf,Pr,t1,nm);
% M. Anderson,1993; last edit 24 Feb 1993
% function file to find coeffs oa, oc to optimize fit of Pcalc to Pobs,
% also range of a and c for double the minimum mean square error
% Use: following fitp or after loading fp(t1_run).mat generated by fitp
% Inputs required: run, tt, tr, pr, cf, Pr, t1; interactive inputs: a, c.
% Outputs: acmse: table (a vs c) of mean square errors
% mse=1/N sum(Pcalc-Pobs)^2      (N=length(tt))
% ad=[oa,mmse,cdub,rse at (oa,cdub)];

```

```

% cd=[oc,mmse,adub,mse at (adub, oc)];
% saved in files op20iw42.mat, .dat (activate l 80,81,82)
function [acmse,ad,cd]=opt20(run,tt,tr,pr,cf,Pr,ti,nm);
ai=input('Enter initial guess for <a> (slope) - ');
da=input('Enter <da>, increment between <a> values - ');
aa=[ai-(10*da):da:ai+(10*da)];
ci=input('Enter initial guess for <c> (intercept) - ');
dc=input('Enter <dc>, increment between <c> values - ');
cc=[ci-(10*dc):dc:ci+(10*dc)];
%
%
% Create domain of all combinations of a and c
[a,c]=meshdom(aa,cc);
% Calculate Pcalc at given a and c
% i.e. at each tt calculate the 2^11 values of Pcalc
% corresponding to each possible combination of c and a.
Pobs=fival(csap2(tr,Pr,1),tt);
P0=Pobs(1); % initial value of P (or Pr(1) same)
summse=0;
ycf=polyval(cf,tt); % p(tt) using cf
ycf0=cf(4); % p(0)
dy0=cf(3); % p'(0)
ddy0=2*cf(2); % p''(0)
ddy0=6*cf(1); % p'''
ddy0=ddy; % p'''(0)
ap=ones(a)./a;
a2p=ap./a;
a3p=a2p./a;
for k=1:length(tt);
dy=3*cf(1)*tt(k)*tt(k)+2*cf(2)*tt(k)+dy0; % p'(tt)
ddy=6*cf(1)*tt(k)+ddy0; % p''(tt)
f1=ycf(k)-dy*ap+ddy*a2p-dddy*a3p;
f2=ycf0-dy0*ap+ddy0*a2p-dddy0*a3p;
Pcalc=f1+(c./a)-(f2+(c./a)-P0).*exp(-a*tt(k));
summse=summse+(Pcalc-Pobs(k)).^2;

```

```

end;
mse=summse/length(tt); % mean square error
%
% find minimum mse (mmse) for optimal a (oa) and optimal c (oc)
[i,j]=min(mse); % i, values, and j, rows, of min value in each col
[k,l]=min(i); % k, value, and l, col, of min value
acmse=[0,a(1,:);c(:,l),mse]; % generate table a vs c with mse values
oa=a(1,l); % optimal value of a is in col(l), (every row),
oc=c(j(l),l); % optimal value of c is in row(j(l)), (every col);
mmse=k; % minimum mse
%
% At optimal value of c what value of a gives double the error?
% Look in row j(l) for closest value
eta=abs(mse-2*mmse);
[meta,k]=min(eta(j(l), )); % value meta in column k
adub=a(j(l),k);
cd=[oc,mmse,adub,mse(j(l),k)]
%
% At optimal value of a what value of c gives double the error?
% Look in col(l) for closest value
[meta,k]=min(eta(:,l)), % value meta in column k
cdub=c(k,l);
ad=[oa,mmse,cdub,mse(k,l)]
%
% Save output to files
mm=['op' nm];
eval(['save ',mm,'.mat acmse ad cd']);
eval(['save ',mm,'.dat /ascii acmse ad cd']),
eval(['copy ',mm,'.dat c:\mah\plots']),
disp(['output saved in ',mm,'.mat,.dat']),

```

pcalccf.m

```

% function [Pcalc,Pertt]=pcalccf(run,tt,tr,t1,Pr,cf,ad,cd,nm),
% M. Anderson, 1993; last edit 24 Feb 1993,
% function file to use cubic fit to p to calculate P(t) (DDB model)
% Use: Following fitp.m and calculation of optimal coeffs,

```

```

% oa, oc for a, c to generate plots of Pcalc, Pobs, and errors
% Input tr,pr,tt,Pr,cf=[h,l,m,n], a, c
% Output Pcalc and Pertt (error in Pcalc-Pobs vs tt).
% Saved in files pc(ti_run).met, .mat, .dat
function [Pcalc,Pertt]=pcalccf(run,tt,tr,ti,Pr,cf,ad,cd,nm);
a=ad(1)
ta=input('Enter value for a, or 0 to use default (oa) - ');
c=cd(1)
tc=input('Enter value for c, or 0 to use default (oc) - ');
if ta==0; else a=ta; end
if tc==0; else c=tc; end
Pobs=fvval(csap2(tr,Pr,1),tt); % Pobs = natural spline fit to Pr.
P0=Pobs(1); % or P0=Pr(1) - no different.
ycf=polyval(cf,tt); % p(tt)
ycf0=cf(4); % p(0)
dy=(3*cf(1)*tt.*tt)+(2*cf(2)*tt)+cf(3); % p'(tt)
dy0=cf(3); % p'(0)
ddy=6*cf(1)*tt+2*cf(2); % p''(tt)
ddy0=2*cf(2); % p''(0)
ddy=6*cf(1); % p'''(tt)
ddy0=ddy; % p'''(0)
f1=(ycf-dy/a+ddy/(a^2)-ddy/(a^3));
f2=(ycf0-dy0/a+ddy0/(a^2)-ddy0/(a^3));
Pcalc=(f1+c/a)-(f2+c/a-P0)*exp(-a*tt);
Pertt=Pcalc-Pobs; % time series of error
mse=sum(Pertt.^2)/length(tt);
%
% plot result
pcalcprt(run,ti,tt,Pcalc,Pobs,Pertt,a,c);
%
% save results
Nt=length(tt);
mm=['pc' nm];
eval(['delete ',mm,'.met; meta ',mm]);
eval(['save ',mm,'.mat run a c Nt tt Pcalc Pertt']);

```

```

eval(['save ',mm,'.dat /ascii a c t1 Nt tt Pobs Pcalc Pertt mse']),
eval(['copy ',mm,' met c:\mah\plots ']),
disp(['output saved to ',mm,'.met, mat, .dat;
plot file copied to print dir']),
clg;

```

actok.m

```

% function smry=actok(run,ad,cd,mp,t1,nm);
% M. Anderson, 1993, Last edit 23 Feb 1993
% function file to calculate kprime, k, kb0,
% sup (st.st supersat'n), spc (sup as %) and all errors
% given coefficients a and c from optimal curvefit to P(t), Pcalc.
% (Based on andata.m and DDB flux model)
% Use: following function opt20.m
% Inputs : id (run label), ad=[oa,mmse,cdub,mse for cdub],
%          mp (mean p), cd=[oc,mmse,adub,mse for adub].
% Outputs: smry=[smryk;smrysup,dm,I;r1,r2];
%          smryk=[kprime;k,kb;kb0]; in cm/h
%          smrysup=[sup,spc] in mbar and %
%          saved in files ok(t1s_run).mat, dat (uncomment 89-91)
function smry=actok(run,ad,cd,mp,t1,nm),
% Formulae:
% a = kprime/dm (1)
% c = kb0*rho*g*r2 (2) to calc kb0
% rho*g=1mbar/cm
% c = kb0*r2
% I=zb/zm
% r1=I(1-exp(-1/I)) (r1=c1 in text)
% r2=I(r1-exp(-1/I)) (r2=c2 in text)
% kprime=k+r1*kb0 (3)
% sup=c/a
% spc=sup*100/mp,
% k is calculated from (1) and (3)
zb=20, % zb=20cm
%zb=input('zb= '); % or manually input zb

```

```

dm=input('dm= '); % mixing layer depth
I=zb/dm;
r1=I*(1-exp(-1/I));
r2=I*(r1-exp(-1/I));
%
oc=cd(1);
oa=ad(1);
%
% Calculations using optimal value of c and range of a:
c=[oc,oc,oc];
da=oa-cd(3);
a=[oa-da,oa,oa+da];
akprime=(dm*a);
akb0=c/r2;
akb=akb0*r1;
ak=akprime-akb;
asup=c./a;
aspc=asup*100/mp;
%
% Calculations using optimal value of a and range for c:
a=[oa,oa,oa];
dc=oc-ad(3);
c=[oc-dc,oc,oc+dc];
ckprime=(dm*a);
ckb0=c/r2;
ckb=ckb0*r1;
ck=ckprime-ckb;
csup=c./a;
cspc=csup*100/mp;
%
%Calculations using optimal values of c and a:
a=oa;
c=oc;
kprime=(dm*a);
kb0=c/r2;

```

```

kb=kb0*r1,
k=kprime-kb;
sup=c/a;
spc=sup*100/mp;
%
% Calculate error ranges
ekprime=mean([(max([akprime,ckprime])-kprime),
kprime-min([akprime,ckprime])]);
ekb0=mean([(max([akb0,ckb0])-kb0),kb0-min([akb0,ckb0])]);
ekb=mean([(max([akb,ckb])-kb),kb-min([akb,ckb])]);
ek=mean([(max([ak,ck])-k),k-min([ak,ck])]);
esup=mean([(max([asup,csup])-sup),sup-min([asup,csup])]);
espc=mean([(max([aspc,cspc])-spc),spc-min([aspc,cspc])]);
%
% Save output, times 60 for min to hour
kprime=[kprime,ekprime]*60;
kb0=[kb0,ekb0]*60;
kb=[kb,ekb]*60;
k=[k,ek]*60;
smryk=[kprime;k;kb;kb0];
sup=[sup,esup];
spc=[spc,espc];
smrysup=[sup;spc];
smrys=['kprime',' k';' kb';' kb0';' sup';
' spc';' dm-I';' r1-r2']
smry=[smryk;smrysup;dm,I;r1,r2]
mm=['ok' nm];
eval(['save ',mm,'.mat run ad cd smry']);
eval(['save ',mm,'.dat /ascii nm t1 ad cd smry']);
eval(['!copy ',mm,'.dat c:\mah\plots ']),
disp(['output saved to ',mm,'.mat, .dat; .dat copied to print dir']);

```

Bibliography

- Anderson, M. L., and B. D. Johnson, Gas transfer: A gas tension method for studying equilibration across a gas-water interface, *J. Geophys. Res.*, *97*, 17899–17904, 1992.
- Asher, W. E., E. C. Monahan, R. Wanninkhof, and T. S. Bates, Correlation of fractional foam coverage with gas transport rates, in *Proceedings of the Second International Symposium on Gas Transfer at Water Surfaces*, edited by S. C. Wilhelms, and J. S. Gulliver, pp. 536–545, New York, Am. Soc. of Civil Engineers, 1991.
- Atkinson, L. P., Effect of air bubble solution on air-sea gas exchange, *J. Geophys. Res.*, *78*, 963–968, 1973.
- Baldy, S., Bubbles in the close vicinity of breaking waves: Statistical characteristics of the generation and dispersion mechanism, *J. Geophys. Res.*, *93*, 8239–8248, 1988.
- Baldy, S., and M. Bourguel, Bubbles between the wave trough and wave crest levels, *J. Geophys. Res.*, *92*, 2919–2929, 1987.
- Blanchard, D. C., and A. H. Woodcock, Bubble formation and modification in the sea and its meteorological significance, *Tellus*, *9*(2), 145–158, 1957.
- Bolin, B., On the exchange of carbon dioxide between atmosphere and sea, *Tellus*, *12*, 247–281, 1960.
- Broecker, H. C., J. Petermann, and W. Siems, The influence of wind on CO₂-exchange in a wind-wave tunnel, including the effects of monolayers, *J. Mar. Res.*, *36*, 595–610, 1978.
- Broecker, H. C., and W. Siems, The role of bubbles for gas transfer from water to air at higher windspeeds. Experiments in the wind-wave facility in Hamburg, in *Gas Transfer*

- at *Water Surfaces*, edited by W. Brutsaert, and G. H. Jirka, pp. 229-236, Norwell, Mass., D. Reidel, 1984.
- Broecker, W. S., An application of natural radon to problems in ocean circulation, in *Symposium on Diffusion in Oceans and Fresh Waters*, pp. 116-145, Palisades, N.Y., Lamont-Doherty Geological Observatory, 1965.
- Broecker, W. S., J. R. Ledwell, T. Takahashi, R. Weiss, L. Merlivat, L. Mémerly, T. H. Peng, B. Jähne, and K. O. Münnich, Isotopic versus micrometeorologic ocean CO₂ fluxes: A serious conflict, *J. Geophys. Res.*, *91*, 10517-10527, 1986.
- Broecker, W. S., and T. H. Peng, The vertical distribution of radon in the BOMEX area, *Earth Planet. Sci. Lett.*, pp. 99-108, 1971.
- Broecker, W. S., and T. H. Peng, *Tracers in the Sea*, p. 690, Lamont-Doherty Geological Observatory, Palisades, N.Y., 1982.
- Broecker, W. S., T. H. Peng, G. Ostlund, and M. Stuiver, The distribution of bomb radiocarbon in the ocean, *J. Geophys. Res.*, *90*, 6953-6970, 1985.
- Cipriano, R., and D. C. Blanchard, Bubble and aerosol spectra produced by a laboratory breaking wave, *J. Geophys. Res.*, *86*, 8085-8092, 1981.
- Cipriano, R. J., and D. C. Blanchard, Reply, *J. Geophys. Res.*, *87*, 5869-5870, 1982.
- Clift, R., J. R. Grace, and M. E. Weber, *Bubbles, Drops and Particles*, Academic Press, New York, 1978.
- Coantic, M., A model of gas transfer across air-water interfaces with capillary waves, *J. Geophys. Res.*, *91*, 3925-3943, 1986.
- Cokelet, E. D., Breaking waves, *Nature*, *267*, 769-774, 1977.
- Craig, H., and T. Hayward, Oxygen supersaturation in the ocean: Biological versus physical contributions, *Science*, *235*, 199-202, 1987.
- Craig, H., and R. F. Weiss, Dissolved gas saturation anomalies and excess helium in the ocean., *Earth Planet. Sci. Lett.*, *10*, 289-296, 1971.

- Crawford, G. B., and D. M. Farmer, On the spatial distribution of ocean bubbles, *J. Geophys. Res.*, *92*, 8231–8243, 1987.
- Csanady, G. T., The role of breaking wavelets in air-sea gas transfer, *J. Geophys. Res.*, *95*, 749–759, 1990.
- Danckwerts, P. V., Significance of liquid-film coefficients in gas absorption, *Ind. Eng. Chem.*, *43*, 1460–1467, 1951.
- Danckwerts, P. V., *Gas-liquid reactions*, McGraw-Hill, New York, 1970.
- D'Aoust, B. G., and M. J. R. Clark, Analysis of supersaturated air in natural waters and reservoirs, *Trans. Amer. Fisheries Soc.*, *109*, 708–724, 1980.
- D'Aoust, B. G., H. Siebold, and R. White, Direct measurement of total dissolved gas pressure, *Undersea Biomedical Research*, *2*, 141–149, 1975.
- Davies, J. T., Rates of gas absorption from single gas bubbles, *Chem. Eng. Sci.*, *41*, 1928–1929, 1986.
- Deacon, E. L., Gas transfer to and across an air-water interface, *Tellus*, *29*, 363–374, 1977.
- Deacon, E. L., Sea-air gas transfer: The wind speed dependence, *Boundary-Layer Met.*, *21*, 31–37, 1981.
- Desjardins, R. L., J. I. MacPherson, P. H. Schuepp, and F. Karanja, An evaluation of aircraft flux measurements of CO₂, water vapour and sensible heat, *Boundary-Layer Met.*, *47*, 55–69, 1989.
- Detsch, R. M., Dissolution of 100 to 1000 μm diameter air bubbles in reagent grade seawater and seawater, *J. Geophys. Res.*, *95*, 9765–9773, 1990.
- Downing, A. L., and G. A. Truesdale, Some factors affecting the rate of solution of oxygen in water, *J. Applied Chem.*, *5*, 570–581, 1955.
- Emerson, S., Chemically enhanced CO₂ gas exchange in a eutrophic lake: A general model, *Limnol. Oceanog.*, *20*, 743–753, 1975.

- Emerson, S., P. Quay, C. Stump, D. Wilbur, and M. Knox, O₂, Ar, N₂, and ²²²Rn in surface waters of the subarctic ocean: Net biological O₂ production, *Global Biogeochem. Cycles*, *5*, 49–69, 1991.
- Erickson III, D. J., A stability dependent theory for air-sea gas exchange, *J. Geophys. Res.*, *98*, 8471–8488, 1993.
- Etcheto, J., and I. Merlivat, Satellite determination of the carbon dioxide exchange coefficient at the ocean-atmosphere interface: A first step, *J. Geophys. Res.*, *93*, 15669–15678, 1988.
- Focal, *The Focal Encyclopedia of Photography*, McGraw-Hill, New York, 1969.
- Galletti, P. M., M. T. Snider, and D. Silbert-Aiden, Gas permeability of plastic membranes for artificial lungs, *Med. Res. Eng.*, *20*, 20–23, 1966.
- Gat, J. R., and M. Shatky, Gas exchange with saline waters, *Limnol. Oceanogr.*, *36*, 988–997, 1991.
- Goldman, J. C., M. R. Dennet, and N. M. Frew, Surfactant effects on air-sea gas exchange under turbulent conditions, *Deep-Sea Res.*, *35*, 1953–1970, 1988.
- Green, E. J., and D. E. Carritt, New tables for oxygen saturation of seawater, *J. Mar. Res.*, *25*, 140–147, 1967.
- Hartman, B., and D. E. Hammond, Gas exchange in San Francisco Bay, *Hydrobiologica*, *129*, 59–68, 1985.
- Hayduk, W., and H. Laudie, Prediction of diffusion coefficients for nonelectrolytes in dilute aqueous solutions, *A.I.Ch.E. J.*, *20*, 611–615, 1974.
- Higbie, R., The rate of absorption of a pure gas into a still liquid during short periods of exposure, *A.I.Ch.E. J.*, *35*, 365–389, 1935.
- Holmén, K., and P. S. Liss, Models for air-water gas transfer: An experimental investigation, *Tellus*, *B36*, 92–100, 1984.

- Hoover, T. E., and D. C. Berkshire, Effects of hydration on carbon dioxide exchange across an air-water interface, *J. Geophys. Res.*, *74*, 456-464, 1969.
- Horne, R. A., *Marine Chemistry*, Wiley-Interscience, New York, 1969.
- Hsu, Y. H. L., P. A. Hwang, and J. Wu, Bubbles produced by breaking wind waves, in *Gas Transfer at Water Surfaces*, edited by W. Brutsaert, and G. H. Jirka, pp. 221-227, Norwell, Mass., D. Reidel, 1984.
- Hwang, P. A., Y. H. L. Hsu, and J. Wu, Air bubbles produced by breaking wind waves: A laboratory study, *J. Phys. Oceanography*, *20*, 19-28, 1990.
- Hwang, P. A., Y. K. Poon, and J. Wu, Temperature effects on generation and entrainment of bubbles induced by a water jet, *J. Phys. Oceanography*, *21*, 1602-1605, 1991.
- Jähne, B., G. Heinz, and W. Dietrich, Measurement of the diffusion coefficients of sparingly soluble gases in water, *J. Geophys. Res.*, *92*, 10767-10776, 1987a.
- Jähne, B., W. Huber, A. Dutzi, T. Wais, and J. Ilmberger, Wind/wave-tunnel experiment on the schmidt number - and wave field dependence of air/water gas exchange, in *Gas Transfer at Water Surfaces*, edited by W. Brutsaert and G. H. Jirka, pp. 303-309, Norwell, Mass., D. Reidel, 1984a.
- Jähne, B., K. O. Münnich, R. Börsinger, A. Dutzi, and W. Huber, On the parameters influencing air-water gas exchange, *J. Geophys. Res.*, *92*, 1937-1949, 1987b.
- Jähne, B., T. Wais, and M. Barabas, A new optical bubble measuring device; a simple model for bubble contribution to gas exchange. in *Gas Transfer at Water Surfaces*, edited by W. Brutsaert, and G. H. Jirka, pp. 237-246, Norwell, Mass., D. Reidel, 1984b.
- Jähne, B., T. Wais, I. Mémerly, G. Caulliez, I. Merlivat, K. O. Münnich, and M. Coantic, He and Ru gas exchange experiments in the large wind-wave facility of IMST, *J. Geophys. Res.*, *90*, 11989-11997, 1985.
- Jenkins, W. J., and J. C. Goldman, Seasonal oxygen cycling and primary production in the Sargasso Sea, *J. Mar. Res.*, *43*, 465-491, 1985.

- Johnson, B. D., and R. C. Cooke, Bubble populations and spectra in coastal waters: A photographic approach, *J. Geophys. Res.*, *84*, 3761-3766, 1979.
- Johnson, B. D., and R. C. Cooke, Generation of stabilized microbubbles in seawater, *Science*, *276*, 209-211, 1981.
- Johnson, B. D., and P. Wangersky, Microbubbles: Stabilization by monolayers of adsorbed particles, *J. Geophys. Res.*, *92*, 14641-14647, 1987.
- Kanwisher, J., On the exchange of gases between the atmosphere and the sea, *Deep-Sea Res.*, *10*, 195-207, 1963.
- Kerman, B. R., A model of interfacial gas transfer for a well-roughened sea, *J. Geophys. Res.*, *89*, 1439-1446, 1984.
- Khoo, B. C., and A. A. Sonin, Augmented gas exchange across wind-sheared and shear-free air-water interfaces, *J. Geophys. Res.*, *97*, 14413-14415, 1992.
- Kolovayev, P. A., Investigation of the concentration and statistical size distribution of wind-produced bubbles in the near-surface ocean layer, *Oceanology*, *15*, 659-661, 1976.
- Kromer, B., and W. Roether, Field measurements of air-sea gas exchange by the radon deficit method during JASIN (1978) and FGGE (1979), *Meteor. Forschungsergeb.*, *24*, 55-75, 1983.
- Large, W. G., J. C. McWilliams, and P. P. Niiler, Upper ocean thermal response to strong autumnal forcing of the Northeast Pacific, *J. Phys. Oceanography*, *16*, 1524-1550, 1986.
- Ledwell, J. J., The variation of the gas transfer coefficient with molecular diffusivity, in *Gas Transfer at Water Surfaces*, edited by W. Brutsaert, and G. H. Jirka, pp. 293-302, Norwell, Mass., D. Reidel, 1984.
- Levich, V. G., *Physicochemical Hydrodynamics*, Prentice-Hall, Englewood Cliffs, N.J., 1962.
- Liss, P. S., Gas transfer: Experiments and geochemical implications, in *Air-sea Exchange of Gases and Particles*, edited by P. S. Liss, and W. G. N. Slinn, pp. 241-298, Norwell, Mass., D. Reidel, 1983.

- Liss, P. S., and L. Merlivat, Air-sea gas exchange rates: Introduction and synthesis, in *The Role of Air-Sea Exchange in Geochemical Cycling*, edited by P. Buat-Ménard, pp. 113–127, Norwell, Mass., D. Reidel, 1986.
- Liss, P. S., and P. G. Slater Flux of gases across the air-sea interface, *Nature*, *247*, 181–184, 1974.
- Liss, P., Processes of gas exchange across an air-water interface, *Deep-Sea Res.*, *20*, 221–238, 1973.
- Medwin, H., and N. D. Breitz, Ambient and transient bubble spectral densities in quiescent seas and under spilling breakers, *J. Geophys. Res.*, *94*, 12751–12759, 1989.
- Mémery, L., and L. Merlivat, Contribution of bubbles to gas transfer across an air-water interface, in *Gas Transfer at Water Surfaces*, edited by W. Brutsaert, and G. Jirka, pp. 247–253, Norwell, Mass., D. Reidel, 1984.
- Merlivat, L., and L. Mémery, Gas exchange across an air-water interface: Experimental results and modeling of bubble contribution to transfer, *J. Geophys. Res.*, *88*, 707–724, 1983.
- Monahan, E. C., and M. C. Spillane, The role of whitecaps in air-sea gas exchange, in *Gas Transfer at Water Surfaces*, edited by W. Brutsaert, and G. H. Jirka, pp. 495–503, Norwell, Mass., D. Reidel, 1984.
- Monahan, E. C., and T. Torgersen, The enhancement of air-sea gas exchange by oceanic whitecapping, in *Proceedings of the Second International Symposium on Gas Transfer at Water Surfaces*, edited by J. S. Gulliver, and S. E. Wilhelms, pp. 608–617, New York, Am. Soc. Civil Engineers, 1991.
- Monahan, E. C., and C. R. Zietlow, Laboratory comparisons of fresh-water and salt-water whitecaps, *J. Geophys. Res.*, *74*, 6961–6966, 1969.
- Murphy, P. P., R. A. Feely, R. H. Gammon, D. E. Harrison, K. C. Kelly, and L. S. Waterman, Assessment of the air-sea exchange of CO₂ in the South Pacific during austral autumn. *J. Geophys. Res.*, *96*, 20455–20465, 1991.

- Peng, T. H., W. S. Broecker, G. G. Mathieu, Y. H. Li, and A. E. Bainbridge, Radon evasion rates in the Atlantic and Pacific Oceans as determined during the GEOSECS program, *J. Geophys. Res.*, *84*, 2471-2486, 1979.
- Phillips, L. F., CO₂ transport at the air-sea interface: Effect of coupling of heat and matter fluxes, *Geophys. Res. Lett.*, *18*, 1221-1224, 1991.
- Platt, T., Primary productivity in the central North Pacific: Comparison of oxygen and carbon fluxes., *Deep-Sea Res.*, *31*, 1311-1319, 1984.
- Platt, T., and W. G. Harrison, Biogenic fluxes of carbon and oxygen in the ocean, *Nature*, *318*, 55-58, 1985.
- Platt, T., and W. G. Harrison, Reconciliation of carbon and oxygen fluxes in the upper ocean, *Deep-Sea Res.*, *33*, 273-276, 1986.
- Quinn, J. A., and N. C. Otto, Carbon dioxide exchange at the air-sea interface: Flux augmentation by chemical reaction, *J. Geophys. Res.*, *76*, 1539-1548, 1971.
- Robertson, J. E., and A. J. Watson, Thermal skin effect of the surface ocean and its implications for CO₂ uptake, *Nature*, *358*, 738-740, 1992.
- Roether, W., and B. Kromer, Optimum application of the radon deficit method to obtain air-sea gas exchange rates, in *Gas Transfer at Water Surfaces*, edited by W. Brutsaert, and G. H. Jirka, pp. 447-457, Norwell, Mass., D. Reidel, 1984.
- Schlichting, H., *Boundary Layer Theory*, p. 535, McGraw-Hill, New York, 1955.
- Schulze, G., and E. U. Schlünder, Physical absorption of single gas bubbles in degassed and preloaded water, *Chem. Eng. Process.*, *19*, 27-37, 1985.
- Scott, J. C., The role of salt in whitecap persistence, *Deep-Sea Res.*, *22*, 653-657, 1975.
- SenSym, *Solid-State Sensor Handbook*, Sunnyvale, Calif., 1989.
- Shatckay, M., and D. Ronen, Bubble populations and gas exchange in hypersaline solutions: A preliminary study, *J. Geophys. Res.*, *97*, 7361-7372, 1992.

- Shulenberger, E., and J. L. Reid, The Pacific shallow oxygen maximum, deep chlorophyll maximum, and primary productivity, reconsidered, *Deep-Sea Res.*, *28*, 901–919, 1981.
- Siems, W., Modelluntersuchungen zur Verdunstung und zum Gasaustausch zwischen Wasser und Luft. Der Einfluß von Wellen und Oberflächenverunreinigungen, Ph.D. thesis, Universität Hamburg, Hamburg, 1980.
- Skirrow, G., *The Dissolved Gases — Carbon Dioxide*, chapter 9, pp. 1–192, Academic Press, New York, 2nd edition, 1975.
- Smethie, W. M., T. Takahashi, D. W. Chipman, and J. R. Ledwell, Gas exchange and CO₂ flux in the Tropical Atlantic Ocean determined from ²²²Rn and pCO₂ measurements, *J. Geophys. Res.*, *90*, 7005–7022, 1985.
- Smith, S. D., R. J. Anderson, E. P. Jones, R. L. Desjardins, R. M. Moore, O. Hertzman, and B. D. Johnson, A new measurement of CO₂ eddy flux in the nearshore atmospheric surface layer, *J. Geophys. Res.*, *96*, 8881–8887, 1991.
- Smith, S. D., and E. P. Jones, Evidence for wind-pumping of air-sea gas exchange based on direct measurements of CO₂ fluxes, *J. Geophys. Res.*, *90*, 869–875, 1985.
- Smith, S. D., and E. P. Jones, Isotopic and micrometeorological ocean CO₂ fluxes: Different time and space scales, *J. Geophys. Res.*, *91*, 10529–10532, 1986.
- Smith, S. V., Physical, chemical and biological characteristics of CO₂ gas flux across the air-water interface, *Plant Cell Environ.*, *8*, 387–398, 1985.
- Spitzer, W. S., and W. J. Jenkins, Rates of vertical mixing, gas-exchange and new production: Estimates from seasonal gas cycles in the upper ocean near Bermuda, *J. Mar. Res.*, *47*, 169–196, 1989.
- Tans, P. P., I. Y. Fung, and T. Takahashi, Observational constraints on the global atmospheric CO₂ budget, *Science*, *247*, 1431–1438, 1990.
- Thomas, F., V. Garçon, and J. F. Minster, Modelling the seasonal cycle of dissolved oxygen in the upper ocean at Ocean Weather Station P, *Deep-Sea Res.*, *37*, 463–491, 1990.

- Thomas, F., C. Perigaud, L. Merlivat, and J. F. Minster, World scale monthly mapping of the CO₂ ocean-atmosphere gas transfer coefficient, *Philos. Trans. R. Soc. London*, *A325*, 71–83, 1988.
- Thorpe, S. A., On the clouds of bubbles formed by breaking wind-waves in deep water, and their role in air-sea gas transfer, *Phil. Trans. R. Soc. Lond.*, *303*, 155–210, 1982.
- Thorpe, S. A., The role of bubbles produced by breaking waves in super-saturating the near-surface ocean mixing layer with oxygen, *Annales Geophysicæ*, *2*, 53–56, 1984.
- Thorpe, S. A., Measurements with an automatically recording inverted echo sounder; ARIES and the bubble clouds, *J. Phys. Oceanography*, *16*, 1462–1478, 1986.
- Thorpe, S. A., P. Bowyer, and D. K. Woolf, Some factors affecting the size distributions of oceanic bubbles, *J. Phys. Oceanography*, *22*, 382–389, 1992.
- Thorpe, S. A., and P. N. Humphries, Bubbles and breaking waves, *Nature*, *283*, 463–465, 1980.
- Torgersen, T., R. Mason, D. Woolf, J. Benoit, M. P. Downing, M. Wilson, and E. C. Monahan, The role of breaking waves in the control of the gas exchange properties of the sea surface, in *Climate and Health Implications of Bubble-Mediated Sea-Air Exchange*, edited by E. C. Monahan, and M. A. V. Patten, pp. 155–162, Avery Point, CT, Connecticut Sea Grant College Program, 1989.
- Torgersen, T., G. Mathieu, R. H. Hesslein, and W. S. Broecker, Gas exchange dependency on diffusion coefficient: Direct ²²²Rn and ³He comparisons in a small lake, *J. Geophys. Res.*, *87*, 546–556, 1982.
- Upstill-Goddard, R. C., A. J. Watson, P. S. Liss, and M. I. Liddicoat, Gas transfer velocities in lakes measured with SF₆, *Tellus*, *B42*, 364–377, 1990.
- Wallace, D. W. R., and C. D. Wirick, Dissolved O₂ time-series records large air-sea gas fluxes associated with breaking waves, *Nature*, *356*, 694–696, 1992.
- Wang, W., D. J. Weubbles, W. M. Washington, R. G. Isaacs, and G. Molnar, Trace gases and other potential perturbations to global climate, *Reviews of Geophysics*, *24*, 110–140, 1986.

- Wanninkhof, R., Relationship between wind speed and gas exchange over the ocean, *J. Geophys. Res.*, *97*, 7373–7382, 1992.
- Wanninkhof, R., J. R. Ledwell, and W. S. Broecker, Gas exchange-wind speed relation measured with sulfur hexafluoride on a lake, *Science*, *227*, 1224–1226, 1985.
- Wanninkhof, R. H., and L. F. Bliven, Relationship between gas exchange, wind speed, and radar backscatter in a large wind-wave tank, *J. Geophys. Res.*, *96*, 2785–2796, 1991.
- Watson, A. J., Carbon dioxide. Conveying that sinking feeling, *Nature*, *356*, 561–562, 1992.
- Watson, A. J., R. C. Upstill-Goddard, and P. S. Liss, Air-sea gas exchange in rough and stormy seas measured by a dual tracer technique, *Nature*, *349*, 145–147, 1991.
- Weiss, R. F., The solubility of nitrogen, oxygen and argon in water and seawater, *Deep-Sea Res.*, *17*, 721–735, 1970.
- Weiss, R. F., Solubility of helium and neon in water and seawater, *J. Chem. Eng. Data*, *16*, 235–241, 1971.
- Weiss, R. F., Carbon dioxide in water and seawater: The solubility of a non-ideal gas, *Mar. Chem.*, *2*, 203–215, 1974.
- Wesely, M. L., D. R. Cook, R. L. Hart, and R. M. Williams, Air-sea exchange of CO₂ and evidence for enhanced upward fluxes, *J. Geophys. Res.*, *87*, 8827–8832, 1982.
- Whitman, W. G., The two-film theory of gas absorption, *Chem. and Met. Eng.*, *29*, 146–148, 1923.
- Wilke, C. R., and P. Chang, Correlation of diffusion coefficients in dilute solutions, *A.I.Ch.E., J.*, *1*, 264–270, 1955.
- Woolf, D. K., and S. A. Thorpe, Bubbles and the air-sea exchange of gases in near-saturation conditions, *J. Mar. Res.*, *49*, 435–466, 1991.
- Wu, J., Bubble populations and spectra in near-surface ocean: Summary and review of field measurements, *J. Geophys. Res.*, *86*, 457–463, 1981.

- Wu, J., Bubbles in the near-surface ocean: A general description, *J. Geophys. Res.*, *93*, 587-590, 1988.
- Wyman, J. J., P. F. Scholander, G. A. Edwards, and I. Irving, On the stability of gas bubbles in sea water, *J. Mar. Res.*, *11*, 47-63, 1952.
- Zieminski, S. A., and R. C. Whittemore, Behaviour of gas bubbles in aqueous electrolyte solutions, *Chem. Eng. Science*, *26*, 509-520, 1971.